Thermo-Optic and Refractometric Performance of Long-Range Surface Plasmon Multiple-Output Mach-Zehnder Interferometers

by

Hui Fan

Thesis submitted to the Faculty of Graduate and Postdoctoral Studies
in partial fulfillment of the requirements for the degree of

Doctor of Philosophy
in Electrical Engineering

Department of Electrical and Computer Engineering
Faculty of Engineering
University of Ottawa

© Hui Fan, Ottawa, Canada, 2016

Abstract

Long-range surface plasmon-polaritons are transverse-magnetic polarized optical surface waves formed through the interaction of photons with free electrons at the surface of metal slabs or stripes. They play important roles in a variety of field such as integrated optics, amplifiers and lasers, optical sensing, modulation, *etc*. Due to their longer propagation length and deeper penetration depth compared to those of single-interface surface plasmon-polaritons, they have become increasingly promising in optical sensing.

In sensing applications, it is necessary to reduce the noise level in order to obtain a lower detection limit. One way to achieve this is to use dual- or triple-output Mach-Zehnder interferometers so that the common perturbations among the outputs can be suppressed. The objective of this thesis is to provide deeper insights on the performances of dual- and triple-output Mach-Zehnder interferometers in thermo-optic and optical bulk sensing applications, theoretically and experimentally, and to demonstrate their ability to suppress common perturbations and lower the detection limit.

On the theoretical side, the objective is approached by constructing a model for the transfer characteristic. For dual-output Mach-Zehnder interferometers, the plane-wave model is used to develop a general model for thermo-optic sensing and an unbalanced model for optical bulk sensing. For triple-output ones, local normal mode theory is used with modal analysis for the 3×3 coupler portion of the structure. Quantitative methods to analyze and compare

different detection schemes are developed. The minimum detectable phase shift is determined for the case of thermo-optic sensing while the detection limit is determined for optical bulk sensing.

On the experimental side, the objective is approached by providing a direct experimental demonstration of the transfer characteristics at an optimized operating wavelength for the coupler portion of the device, then comparing to theory. Time traces are carried out and various detection schemes are applied to suppress common perturbations among the outputs, and to improve the minimum detectable phase shift or the detection limit.

Acknowledgements

First of all, I would like to acknowledge my supervisor - Professor Pierre Berini, for his guidance on both theory and experiments, as well as technical writing, throughout the course of my graduate studies, and also, for providing financial support for this research.

I would like to acknowledge Anthony Olivieri, Asad Khan, Ewa Lisicka-Skrzek, Israel de Léon Arizpe, Maude Amyot-Bourgeois, Mohammad Alavirad, Oleksiy Krupin, and Wei Ru Wong for their assistance in experiments and experimental setup construction.

I would like to acknowledge Akram Hajebifard, Behnood Ghamsari, Elham Keshmarzi, Kholoud Gazzaz, Naema Mahmoud Othman, Robert Charbonneau, Robin Buckley, and Yansong Cui for their assistance in modal analysis and numerical method implementation.

I would like to acknowledge Charles Chiu and Hamoudi Asiri for fabrication of my devices.

I would like to acknowledge André Duarte, Andrea Brouwer, Chengkun Chen, Lu Xiao, Maryam Al-Shehab, Maryam Khodami, Norman Fong, Paul Béland, Sa'ad Hassan, Saba Siadat Mousavi, and many other colleagues and friends for cooperation in all of my simulation and lab work.

I would also like to acknowledge my parents for providing financial support for my living expenses, and for their encouragement.

Publications

Papers published and accepted in referred journals

- H. Fan and P. Berini, "Bulk sensing using a long-range surface-plasmon triple-output Mach-Zehnder interferometer," Journal of the Optical Society of America B 33 (6), 1068-1074 (2016).
- H. Fan and P. Berini, "Bulk sensing using a long-range surface-plasmon dual-output Mach-Zehnder interferometer," Journal of Lightwave Technology 34 (11), 2631-2638 (2016).
- H. Fan, R. Charbonneau, and P. Berini, "Long-range surface plasmon triple-output Mach-Zehnder interferometers," Optics Express 22 (4), 4006-4020 (2014).
- H. Fan and P. Berini, "Noise cancellation in long-range surface plasmon dual-output Mach-Zehnder interferometers," Journal of Lightwave Technology 31 (15), 2606-2612 (2013).
- H. Fan and P. Berini, "Thermo-optic characterization of long-range surface plasmon devices in Cytop," Applied Optics 52 (2), 162-170 (2013).

Conferences Presented

- SPP 6, 26 May – 1 June 2013, Ottawa, Canada.
- Photonics North 2015, 9 June – 11 June 2015, Ottawa, Canada.

Acronyms

16-MHA 16-mercaptohexadecanoic Acid

BCB Benzocyclobutene

CCD Charge-Coupled Device

DDI Distilled / Deionized

DLSPP Dielectric-Loaded Surface Plasmon-Polariton

FEM Finite Element Method

GPIB General-Purpose Interface Bus

IL Insertion Loss

IMI Insulator-Metal-Insulator

IPA Isopropyl Alcohol

IR Infrared

LASER Light Amplification by Stimulated Emission of Radiation

LOD Limit of Detection

LRSPP Long-Range Surface Plasmon-Polariton

MOL Method of Lines

MPA Mode Power Attenuation

MZI Mach-Zehnder Interferometer

PFCB Perfluorocyclobutane

PMF Polarization Maintaining Fiber

RI Refractive Index

RIU Refractive Index Unit

SDS Sodium Dodecyl Sulfate

SMF Single Mode Fiber

SNR Signal-to-Noise Ratio

SPP Surface Plasmon-Polariton

SPR Surface Plasmon Resonance

TE Transverse Electric

TL Transition Loss

TM Transverse Magnetic

TOC Thermo-Optic Coefficient

UV Ultraviolet

VOA Variable Optical Attenuator

Table of Contents

Chapter 1

Introduction

1.1 Surface plasmon-polaritons

Valence electrons in metals regarded as a high density electron gas can sustain longitudinal electromagnetic charge density waves called plasma oscillations [1-3], which are energy quantized as plasmons in the quasiparticle viewpoint. Plasmons exist in the volume of the metal, namely the bulk plasmons, as well as on its surface, namely surface plasmons. Visible and near infrared light can couple to plasma oscillations at a metal-dielectric interface, creating a transverse-magnetic (TM) polarised optical surface wave quantized as quasiparticles referred to as surface plasmon-polaritons (SPPs). The field of SPPs peak at the metal-dielectric interface and decay exponentially into both media, with a typical penetration depth of a few nanometers on the metal side, as shown in Fig. 1.1. The red curves represent the profile of the main transverse electric field component (E_y) of an SPP mode propagating along the z axis (directed out of the page). The single-interface SPP waveguide consists of an optically semi-infinite dielectric with relative permittivity $\varepsilon_{r,1}$ and a metal with relative permittivity $\varepsilon_{r,2}$. The single-interface SPP mode has useful properties such as good confinement and high surface and bulk sensitivities, but also high attenuation preventing the mode from travelling appreciable distances. The attenuation problem is significantly improved by using long-range surface plasmon-polaritons (LRSPPs).

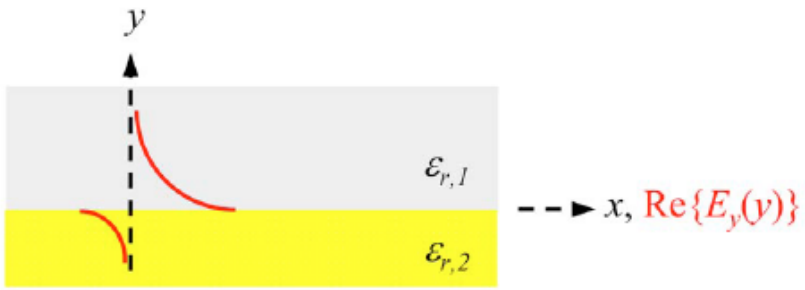

Fig. 1.1 Mode field profile of a single-interface SPP supported by the interface between a metal ($\varepsilon_{r,2}$) and a dielectric ($\varepsilon_{r,1}$) [4]

1.2 Long-range surface plasmon-polaritons

In order to reduce the attenuation, a thin metal slab or stripe bounded on all sides by the same dielectric material is used as the waveguide, supporting modes with comparatively lower attenuation and allowing propagation over a much longer distance, and thus named long-range SPPs. It has been demonstrated experimentally that attenuation reduction factors could be greater than 100 with the LRSPP, though this comes at the expense of a lower surface sensitivity which could be outweighed by the longer propagation length potentially enabling better applications [4].

1.2.1 Metal slab

If the width of the metal layer is optically infinite, the waveguide is called a "metal slab". Figure 1.2 shows the metal slab structure. The red curves represent the profile of the main transverse electric field component (E_y) of the supported modes propagating along the z axis (directed out of the page). The structure consists of a thin metal film with thickness t and relative permittivity $\varepsilon_{r,2}$ bounded on both sides by optically semi-infinite dielectric claddings with relative permittivity $\varepsilon_{r,1}$ and $\varepsilon_{r,3}$, which are supposed to be symmetric ($\varepsilon_{r,1} = \varepsilon_{r,3}$). When the thickness t of the metal slab reduces to nanometer-scale, the two single-interface SPPs at

the top and bottom interfaces couple with each other and form two TM-polarised supermodes [4], with their main transverse electric field component either symmetric or asymmetric, and thus referred to as s_b or a_b, respectively. The subscript b signifies "purely bound", meaning non-radiative, in contrast with two radiative modes labeled s_L and a_L in which the subscript L stand for "leaky". Among these modes, the s_b is identified as the LRSPP mode supported by a metal slab. Suppose the claddings are symmetric and lossless, the attenuation of the s_b mode diminishes as the thickness t reduces, because the mode field is increasingly expelled from the metal slab and penetrates deeper into the claddings [4]. Oppositely, the a_b mode shows more confinement in the metal as t reduces. Its attenuation increases, making the mode short-ranged.

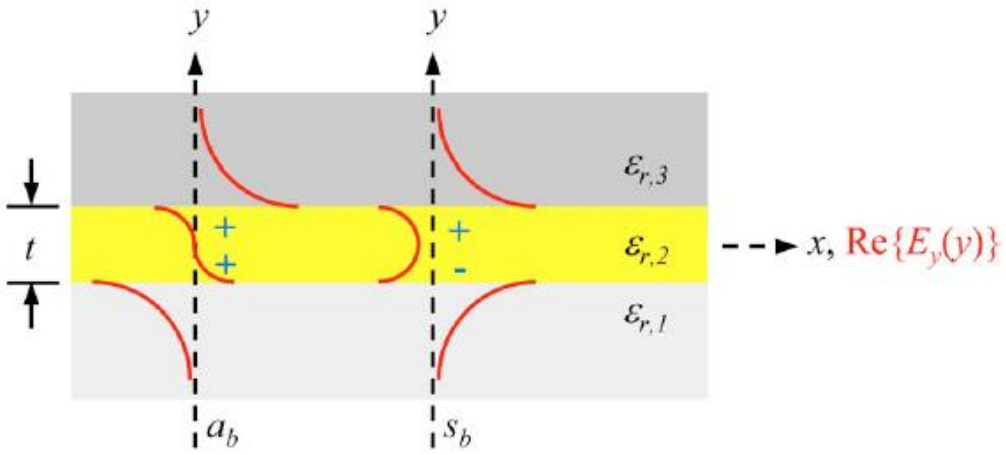

Fig. 1.2 Mode field profile of SPP supermodes (a_b, s_b) supported by a metal slab ($\varepsilon_{r,2}$) of thickness t bounded by two dielectric claddings ($\varepsilon_{r,1}$, $\varepsilon_{r,1}$) [4]

1.2.2 Metal stripe

If the width of the metal layer is not optically infinite, the waveguide is called a "metal stripe", as exhibited in Figure 1.3. The structure consists of a thin metal stripe with thickness t, width w, and relative permittivity $\varepsilon_{r,2}$ bounded by optically semi-infinite dielectric

claddings with relative permittivity $\varepsilon_{r,1}$ and $\varepsilon_{r,3}$. The direction of mode propagation is along the *z* axis (directed out of the page). In a metal stripe structure the solutions to Maxwell's equations are not analytical, but have to be derived numerically. This difficulty is due to the fact that all modes are created from the coupling of elemental corner or edge modes, which varies with structure parameters and operating wavelength, making the coupled modes unpredictable [4]. Despite the increasing analysis effort, the metal stripe can be handled by well-established numerical techniques such as the method of lines (MoL) and the finite element method (FEM).

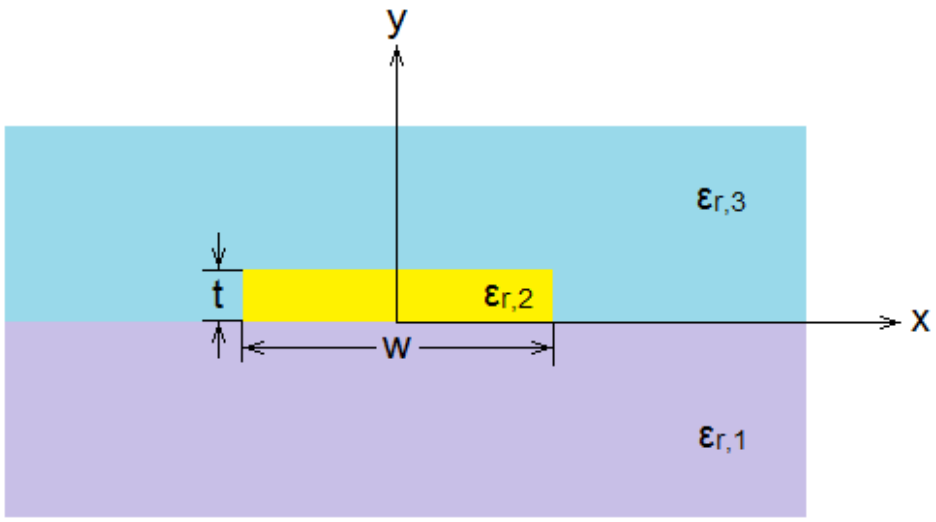

Fig. 1.3 Cross-sectional view of a LRSPP waveguide consisting of a metal stripe ($\varepsilon_{r,2}$) of thickness *t* and width *w* bounded by two dielectric claddings ($\varepsilon_{r,1}$, $\varepsilon_{r,1}$)

When symmetric claddings are assumed ($\varepsilon_{r,1} = \varepsilon_{r,3}$), the metal stripe structure supports four fundamental modes aa_b^0, as_b^0, sa_b^0, and ss_b^0, where *s* and *a* refer to symmetric and asymmetric, respectively. The first position is associated with the horizontal dimension *x* and the second with the vertical dimension *y*. The *b* here implies "purely bound" or non-radiative. Higher order modes are also supported where the E_y field component dominates for all

modes when t is small enough compared to w, hence the modes are essentially TM in character [4]. As t approaches zero, they can eventually be categorized into two groups: long-ranged modes (ss_b^m and as_b^m) acting like the s_b mode in a metal slab, and short-ranged modes (sa_b^m and aa_b^m) like the a_b mode, depending on the symmetry of the E_y distribution along y. Here m refers to the m~th order mode. The most commonly used mode among them is the fundamental long-range mode ss_b^0, which has a field distribution well-matched to Gaussian-like fields such as the output beam of a single mode fiber and thus is easily amenable to end-fire excitation. In most cases, the ss_b^0 mode is regarded as the LRSPP mode supported by a metal stripe. The higher order modes have attenuation low enough to be considered as long-range only near cut-off, where modes with sa_b^m and aa_b^m symmetries have increasing attenuation as t approaches zero and hence are not long-range. Thus a metal stripe with symmetric claddings can become a single mode structure by choosing appropriate stripe dimensions.

When the claddings are asymmetric, the ss_b^0 mode does not exist in a very thin asymmetric metal stripe for it exhibits a cut-off thickness that is not present in the symmetric structures, making it sensitive to asymmetry of refractive index in top and bottom claddings.

1.3 Thermo-optic sensing using LRSPPs

The thermo-optic effect is a phenomenon by which heat can influence the refractive index of a material [5], which has been explored for potential applications such as thermo-optic modulation, switching, and sensing using LRSPPs. Keeping the operating wavelength constant, the refractive index of a material changes linearly with temperature over a small temperature range (*e.g.* less than ~100 ^{o}C [6]), as given in the equation below.

$$n(T) = n(T_0) + (T - T_0)\frac{dn}{dT} \tag{1.1}$$

Here n is the refractive index of the material and T is the temperature. dn/dT is called the thermo-optic coefficient (TOC), which can be regarded as constant when the temperature range is relatively small. If the temperature range is too large, the TOC should be decomposed as a sum of smaller ranges of constant TOC and Eq. (1.1) changes into the following relation below.

$$n(T_N) = n(T_0) + \sum_{i=0}^{N-1}(T_{i+1} - T_i)\left[\frac{dn}{dT}\right]_{T_i} \tag{1.2}$$

Here i and N are the i~th sub-range and the total number of sub-ranges, respectively. Thus, given the temperature range of the thermo-optical device, the refractive index can be determined by applying Eqs. (1.1) and (1.2). The linear relationship between refractive index and temperature in the thermo-optic effect is obtained by differentiating the Clausius-Mossotti relation [6].

To conduct thermo-optic modulation on LRSPP waveguides, a few mechanisms have been designed and applied so that the change in temperature can affect the total insertion loss of the devices. Typical schemes include thermally-induced antiguiding and inducing refractive index asymmetry on straight waveguides, and phase-sensitive schemes using single- and multiple-output Mach-Zehnder interferometers (MZIs).

1.3.1 Thermally-induced antiguide

In this scheme, a straight LRSPP waveguide serves as both the optical path and the heat source, in which electric current generates heat when injected into the metal stripe forming

the waveguide, as shown in Fig. 1.4. Features added for thermo-optic control includes metal pads to connect to the current source and gaps to isolate the current to the active region of the metal stripe. The heat generated along the waveguide increases the temperature around the metal, forming a temperature gradient in the nearby dielectric claddings as the heat dissipates outwards, changing the refractive index accordingly. Polymers such as Cytop have a negative TOC [7], and thus as the cladding is made of polymer, its refractive index close to the metal stripe (heat source) is lower than regions further away, forming an antiguide (lower refractive index in the center than elsewhere), inducing radiation loss in the propagation of the LRSPP mode due to reduced confinement. When the current density of the injected current increases, the antiguide becomes stronger and eventually cuts off the LRSPP mode.

Fig. 1.4 Sketch of an LRSPP straight waveguide for thermo-optic modulation. The active region is highlighted in red.

1.3.2 Thermally-induced refractive index asymmetry

In this scheme, the same modulation structure is used as in Fig. 1.3 but a different cut off mechanism is applied. An asymmetry in refractive indices of the top and bottom claddings is induced, motivated by the fact that the LRSPP mode is sensitive to such an asymmetry. One method to realize this mechanism is to use different dielectrics for the top and bottom claddings. The two materials are refractive-index matched at room temperature but have different TOCs, so that heating the structure mismatches the refractive indices of the claddings, inducing an asymmetry that increases the loss of the LRSPP mode propagating

along the waveguide, and eventually cuts off the mode. Another method is to generate a temperature gradient in the waveguide region from top to bottom by adding a heater on the top and a heat sink at the bottom (or the opposite), as illustrated in Fig. 1.5.

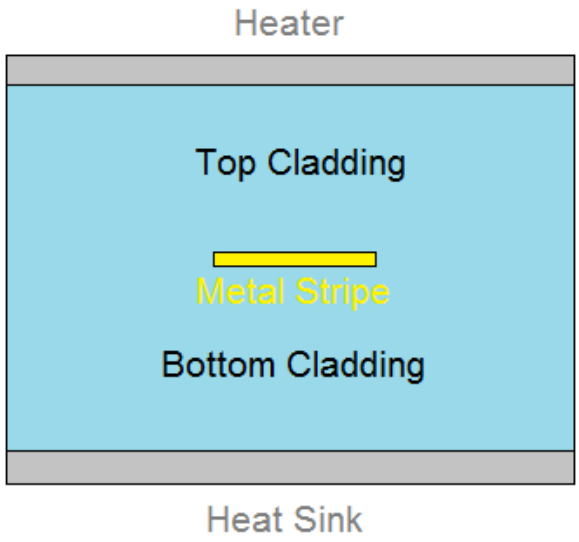

Fig. 1.5 Cross-sectional view of a waveguide structure generating a temperature gradient from top to bottom to create refractive index asymmetry.

1.3.3 Thermally-induced phase shift

In this scheme, an MZI is used as the modulator and electric current is injected along one of the arms, as shown in Fig. 1.6(a). Again, additional features for thermo-optic control such as metal pads and gaps are added to the active region of the metal stripe. The change in refractive index with temperature in the heated arm leads to the change in optical path length, and therefore a phase shift relative to the other arm. As the current varies, the thermally-induced phase shift changes between constructive and destructive interference conditions, and the output optical power oscillates between maximum and minimum. Care must be taken not to drive (thermally) the waveguide into cut-off via anti-guiding. The Y-junction on the output side can be replaced by a 3-dB (50:50) or a 3×3 coupler, constituting a dual- or triple-

output MZI, as shown in Fig. 1.6 (b) and (c). Compared to their single-output counterpart, multiple output MZIs have the advantages of larger dynamic range and the ability to suppress common perturbations, and therefore are more promising in optical sensing applications.

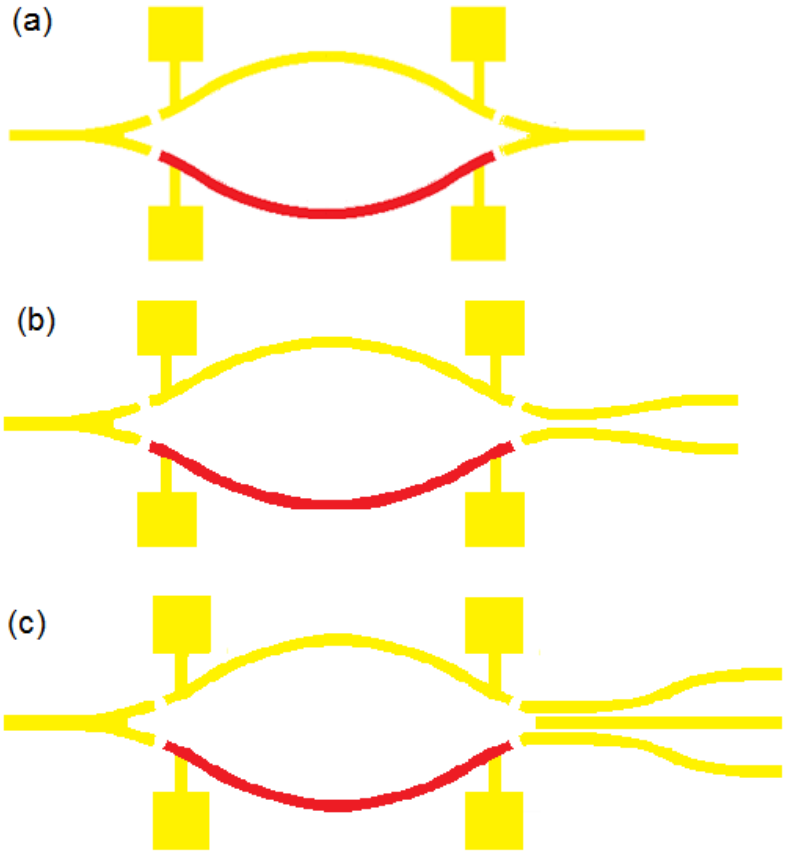

Fig. 1.6 Sketch of LRSPP MZIs for thermo-optic modulation, including (a) single-, (b) dual- and (c) triple-output MZIs. The active regions are highlighted in red.

1.4 Optical biosensing

Many fields including medical diagnosis, pharmaceuticals, food processing, environmental monitoring, *etc*, require the detection of certain drugs or pathogens, making biomedical sensing more and more important in a variety of applications. The analysis of certain

biomolecules can be realized optically, for instance, by detecting fluorescence, chemiluminescence, or the change of absorbance and/or reflectivity.

1.4.1 Fluorescence-based methods

One method to conduct optical biosensing is to tag the target biomolecules with fluorescent dye [8], as shown in Fig. 1.7. For instance, when detecting an antigen, its fluorescein-labeled antibody is prepared. The sample containing the antigen of interest is then immobilized to a surface of a substrate and the antibody is added in. A certain amount of time is given for the binding, and then any unbound antibody is rinsed off. By detecting the fluorescence the concentration of the antigen in the sample can be determined. This method is commonly used but it induces problems such as photo-bleaching and signal bias, and in most cases the immobilization process is not easy but rather complicated and time consuming.

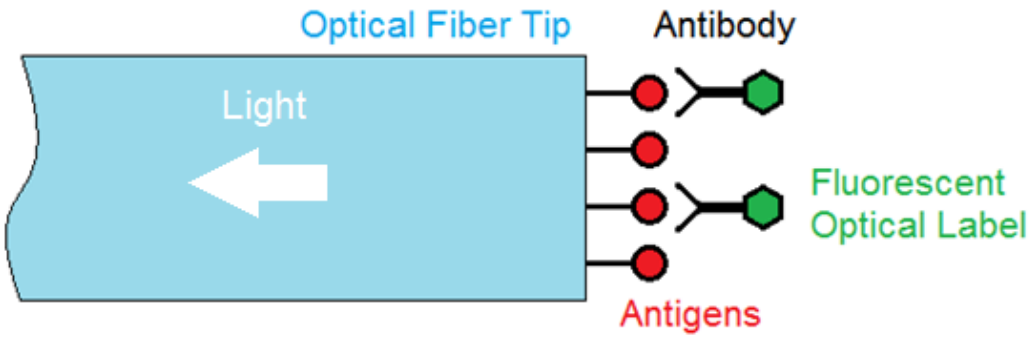

Fig. 1.7 Construction of a fluorescence-based antibody optical fiber biosensor.

Except for antibody-antigen detection, fluorescence is also used for enzyme detection, in which a fluorescent dye is used in the reaction system to indirectly monitor the formation of a product or the consumption of the analyte. For instance, such optical biosensing can be conducted if a certain fluorescent dye is found for which the product of the reaction serves as a fluorescent quencher [9].

1.4.2 Chemiluminescence-based methods

Label-free optical biosensing allows for detection without labeling biomolecules as well as real-time monitoring [10]. One method for label-free optical biosensing is to utilize chemiluminescence, which is the emission of light as the result of a chemical reaction. A distinct advantage of this method is that no excitation light source is required since light can be generated during the reaction, and thus no additional apparatus is necessary to remove the scattered excitation light. The chemiluminescence-based methods usually have more simplified optical instrumentation as well as better selectivity and sensitivity than the fluorescence-based methods.

1.4.3 Surface Plasmon Resonance

Another method for label-free optical biosensing is to detect the change of absorption and/or reflection, as in the popular surface plasmon resonance (SPR) technique, which has been well-developed, with early commercialization, miniaturized devices, and considerable amount of publications related to the topic. Conventional SPR biosensing is based on the Kretschmann-Raether configuration, consisting of a prism with a thin layer of Au integrated with fluidics and a CCD detector, interrogated with a transverse magnetic (TM) polarized beam, as shown in Fig. 1.8.

The prism is used to excite surface plasmons at a certain angle known as the SPR angle θ, at which plasmon excitation occurs with the energy of the incident light partially coupled into the surface plasmons and the optical power of the reflected light decreasing. θ is dependent on the refractive index of the sample solution as well as the presence of an adlayer at the metal-solution interface. In the sensing process, the refractive index of the bulk part of the

sample solution in the flow cell or the thickness of the adlayer changes, causing θ to change accordingly.

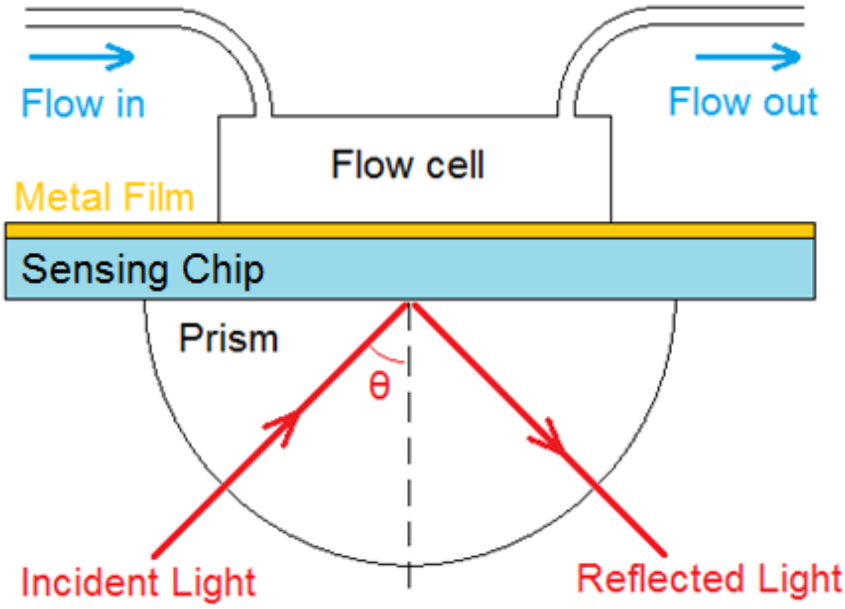

Fig. 1.8 Schematic view of an SPR sensor.

As mentioned above, there are two different mechanisms that can be used for SPR sensing. One is to change the refractive index of the sample solution in the flow cell, which is referred to as "bulk sensing". The other is to form an adlayer on the top surface of the metal stripe, which is referred to as "surface sensing" and is more commonly used in biosensing applications.

1.4.4 LRSPP bulk sensing and biosensing

In recent years, LRSPPs have been increasingly investigated in optical sensing due to their longer propagation length and deeper penetration depth. Their surface sensitivity is relatively lower than in conventional SPR, but that is compensated by the longer sensing surface that

can be used, and therefore the total sensitivity is better and the detection limit lower than in conventional SPR sensors [11].

The layout of the LRSPP structures used in biosensing is the same as in the thermo-optic structures (straight waveguide, single- and multiple-output MZIs) shown in Fig. 1.4 and 1.6 except for the additional features for thermal control. The metal pads and gaps added to the active region for thermo-optic actuation are replaced by etched fluidic channels defining the region for biosensing. The channels expose the top surface of the metal stripe to the surrounding medium, where sample solutions are injected and sensing occurs. Similar to SPR, there are two mechanisms of sensing when applying LRSPPs. The bulk (refractometric) sensing is conducted when the bulk refractive index in the fluidic channel changes as one sample solution replaces another, while surface sensing is carried out when an adlayer is formed on the top surface of the metal waveguide during biochemical interaction, for example, the binding between antigens and antibodies. The work related to this thesis focuses the discussion on bulk sensing, because the motivation of this work is to use multiple-output MZIs to improve the detection limit, and bulk sensing is easier to handle than surface sensing. However, the ideas for detection limit improvement in bulk sensing discussed in this thesis can also be applied to surface sensing.

1.5 Literature review

1.5.1 Thermo-optic modulation and sensing

As mentioned above, thermo-optic devices can be basically divided into three types. The first type uses a straight waveguide based on thermally-induced antiguide. Nikolajsen *et al.* [12] demonstrated variable optical attenuators (VOAs) with 15 nm thick and 8 μm wide Au stripe

between 15 μm thick benzocyclobutene (BCB) claddings, and investigated its wavelength dependence within the main telecom interval of 1470-1610 nm. Fan *et al*. [13] demonstrated a similar VOA with 35 nm thick and 5 μm wide Au stripe cladded by Cytop operating at ~1310 nm. Park *et al.* [14] demonstrated a VOA with a separate heater on top of the metal stripe, utilizing both thermally-induced anti-guiding and an asymmetric mode cut-off due to the temperature gradient of the claddings caused by the heater. Leosson *et al.* [15] conducted experiments on a similar VOA based on a nanowire hundreds of nanometers thick and wide instead of metal stripes. Leosson *et al.* [16] observed a >20 dB extinction ratio, <3V driving voltage and >1 kHz modulation bandwidth on a nanowire-based VOA operating at free space wavelengths 1525-1625 nm. Rosenzveig *et al*. [17] demonstrated the feasibility of fabricating nanowire-based VOA devices, and observed a thermo-optic memory effect in polymer in the experiments.

The second type also uses straight waveguides and is based on thermally-induced asymmetric mode cut-off. Gagnon *et al.* [5] demonstrated a VOA operating at a free space wavelength of ~ 1550 nm consisting of a Au stripe cladded with SiO_2 and index-matched polymer on top. Breukelaar *et al.* [18] investigated a VOA using SiO_2 and $LiNbO_3$ as claddings, and obtained a change in insertion loss of better than 20 dB. Breukelaar *et al.* [19] performed theoretical analysis on a VOA based on Au slab and SiO_2 claddings with asymmetric refractive indices, and the cut-off points of lossless and lossy waveguides were compared.

The third type uses MZIs based on thermally-induced phase shift between the sensing and the reference arms. Nikolajsen *et al.* [20] demonstrated single-output MZI modulators and directional-coupler switches consisting of Au stripes in BCB claddings operating at 1550 nm,

featuring low driving powers, high extinction ratios, and moderate response times. Fan *et al.* [13] investigated single-output MZIs with Au stripes and Cytop claddings operating at 1310 nm.

Additionally to LRSPPs, dielectric-loaded SPPs (DLSPPs) [21-24] have also been developed for thermo-optic sensing in recent years.

1.5.2 Optical bulk sensing and biosensing

A popular and sensitive technique for optical biosensing is to label specific targets with fluorescent dyes in which a primary antibody or antigen is immobilized to the surface of a substrate. One typical example is the experiments carried out by Marks *et al.* [25] to detect cholera antitoxin antibodies. The researchers coated polypyrrole-biotin on the end-facet of an optical fiber and then sequentially attached a few chemical reagents (avidins, biotin labeled cholera toxin B subunits, anti-cholera toxin B subunits, and HRP-labeled goat anti-rabbit LgG peroxidase) by steps for immobilization, and finally hydrogen peroxide and luminol are added to the reaction mixture to emit light. Another scheme of fluorescence-based biosensing is to use fluorescent dyes in the reaction system to monitor the formation of a product or the consumption of an analyte. Research using this scheme consists of a sensor designed by Ignatov *et al.* [9] for lactate detection. The principle is that the fluorescent dye ruthenium is quenched by oxygen. When lactate is catalyzed by lactate oxidase, it consumes oxygen, and the decrease in oxygen concentration leads to an increase in ruthenium fluorescence.

Chemiluminescence and Electrochemiluminescence is the emission of light as the result of a chemical or electro-generated chemical reaction. Biosensing methods based on them have the advantages that no excitation light source is needed or an apparatus to remove scattered

excitation light, yielding better selectivity and sensitivity. They are commonly used for detecting hydrogen peroxide formed by enzymatic reactions. Zhu *et al*. [26] constructed an electrogenerated chemical reaction flow system to detect glucose. Ramos *et al.* [27] design a sensor for p-iodophenol, 2-naphthol, and p-coumaric acid using horseradish peroxidase immobilized in sol-gel on the end of an optical fiber.

Although there have been many successful label-free approaches in recent years, for instance, long period fiber gratings demonstrated by Garg *et al*. [28], SPR has dominated the field of optical biosensing for its high sensitivity. Feltis *et al*. [29] demonstrated a self-contained hand-held biosensor based on SPR, capable of detecting trace levels of the bio-toxin ricin. Relevant biologicals can be detected and validated in a 20 min timeframe. Wu *et al*. [30] presented a phase-sensitive SPR biosensor based on the MZI design using a Wollaston prism to interrogate the phase of two polarizations simultaneously, and obtained results from experiments on glycerin–water mixtures showing a sensitivity limit of 5.5×10^{-8} refractive index unit (RIU) per 0.01° phase change. Hadjar *et al*. [31] proposed a monolithic interferometric configuration based on Fabry-Perot interferometers for phase shift detection using SPR sensors. Nguyen *et al*. [32] demonstrated an optical fiber refractometric sensor based on SPR, integrating a periodic array of resonant nano-apertures in a gold film onto the end-facet of an optical fiber, and they achieved a sensitivity of 755 ± 12 nm/RIU. Špringer *et al*. [33] enhanced the sensitivity of SPR sensors using functionalized Au nanoparticles, which can also be applied to different types of optical biosensors. Vaisocherová *et al*. [34] recently demonstrated the commercialization potential of an ultra-low fouling SPR imaging biosensor for the rapid parallel detection of miRNA for clinical use, combining the

advantages of high sensitivity and the parallelized detection ability of two conventional miRNA detection methods.

Apart from conventional SPR sensors, biosensing using single-interface SPP waveguides have been demonstrated. Gao *et al*. [35] proposed a vertical MZI biosensor constructed by two nanoslits on a flat metal film serving as the waveguides of SPPs. Zeng *et al*. [36] proposed a sensitive multiplexed MZI sensor array based on the interference between single-interface SPP and Metal-Insulator-Metal SPP modes supported in a multi-layered structure.

Benefiting from longer propagation lengths and deeper penetration depths, LRSPPs exploited in prism-coupled sensors have been demonstrated to have better performance than conventional SPR. Dostálek *et al*. [37] implemented a layer structure consisting of a fluoropolymer buffer layer, a thin gold film, and an aqueous sample in an SPR sensor to excite LRSPPs. Slavík *et al*. [38] modified conventional SPR by depositing a low refractive index fluoropolymer Teflon at the interface between the glass prism and Au film, and demonstrated a detection limit of 2.5×10^{-8} RIU. Vala *et al*. [39] reported that LRSPP-based sensors were ~8 times more sensitive to sample refractive index changes than conventional SPR sensors, and their responses were 2.5 to 5.5 times greater. Chabot *et al*. [40] reported that LRSPP-based sensors exhibit a 50% greater sensitivity compared to conventional SPR sensors for toxicity measurements based on living cells.

LRSPPs excited in end-fire coupled sensors based on a straight waveguide have been demonstrated. Krupin *et al*. [41] proposed a sensor consisting of 5 μm wide and 22 nm thick Au stripes embedded in Cytop with microfluidic channels etched into the top cladding. The biosensor demonstrated a good capability for bulk sensing (with a detection limit of $2.3 \times 10^{-}$

^{6} RIU) and for sensing analyte over a wide range of mass (from cells to proteins). They used the same device for the detection of blood group antigen A on whole erythrocytes [42] and leukemia markers in patient serum using a functionalization strategy based on Protein G [43]. Wong *et al*. [44] used a similar device for the detection of dengue-specific immunoglobulin M antibody in actual patient blood plasma samples. Béland *et al*. [45] demonstrated the potential of a similar device to be used in diagnosis of urinary tract infection.

LRSPP sensors based on single-output MZIs have also been demonstrated for bulk sensing. Khan *et al*. [46] proposed refractometric sensing experiments using a compact integrated single-output MZI formed from thin Au stripes in Cytop with an etched microfluidic channel defining the sensing arm, and achieved a detection limit of 9×10^{-7} RIU. Vernon *et al*. [47] theoretically demonstrated a similar single-output MZI sensor, with the two Y-junctions on the input and output sides replaced by two 3×3 couplers.

1.6 Thesis scope and outline

The motivation for this work is to develop new structures based on LRSPP multiple-output MZIs for thermo-optic operation, bulk refractometric, and biochemical sensing. The thesis aims to provide deeper insights on the performances of single- and multiple-output MZIs both theoretically and experimentally, and on the ability of common perturbation suppression for dual- and triple-output MZIs. The scope of this thesis comprises three important points:

- *Experimental demonstration of transfer characteristics on single-, dual- and triple-output MZIs*: In the context of LRSPP thermo-optic and optical bulk sensing the demonstrated devices are polymer-cladded straight metal stripes, nanowires, or single-, dual- and triple-output MZIs, the latter two having the advantages of 2 × and

3 × larger dynamic range respectively, compared to their single output counterpart and the ability to suppress common perturbations.

- *Theoretical analysis of dual- and triple-output MZIs*: In order to compare experimental transfer characteristics with theory, analyses of multiple-output MZI models, especially their coupler portion, are necessary. As for the dual couplers, the thesis presents a theoretical expectation of the transfer characteristic based on plane-wave model. As for the triple couplers, the thesis presents a theoretical model for three-waveguide coupling based on modal analysis so that simple equations that model the operation of an idealised design can be given.
- *Study of detection schemes to improve the detection limit using dual- and triple-output MZIs*: It would be beneficial to take advantage of the multiple outputs to cancel off or at least suppress some of the common perturbations, such as a drift in the input optical power or input coupling conditions, or the background light. The thesis analyzes different detection schemes to obtain the best common perturbation suppression and the best detection limit of the devices for use in thermo-optic applications and optical bulk sensing.

This thesis consists of a collection of scientific articles, each of them presented as a chapter. The remainder of this thesis is organized as follows. Chapter 2 demonstrates the transfer characterisation of single-output MZIs in thermo-optic sensing theoretically and experimentally. Chapter 3 reports the theoretical performance of a dual-output MZI, the experimental transfer characteristics in thermo-optic modulation, and the detection schemes to improve the minimum detectable phase shift. Chapter 4 reports the theoretical performance of a triple-output MZI based on the modeling results of a 3 × 3 coupler, the

experimental transfer characteristics in thermo-optic modulation, and the detection schemes. Chapter 5 reports the theoretical performance of an unbalanced dual-output MZI, the experimental transfer characteristics in optical bulk sensing, and the schemes to improve the detection limit of the device. Chapter 6 reports the experimental transfer characteristics of a triple-output MZI in optical bulk sensing compared with theoretical expectation by fitting, and the detection schemes. Chapter 7 concludes this work and presents suggestions for future work.

Chapter 2

Thermo-optic characterisation of LRSPP single-output MZIs

2.1 Theoretical

2.1.1 Mechanism of modulation

The mechanism of thermo-optic modulation of single-output MZIs is to inject an electrical current into one arm of the MZI, namely the sensing arm, while the other arm, namely the reference arm, remains isolated. When the current passes through the metal stripe along the waveguide, heat is generated therein and diffuses into the dielectric claddings, thus modulating the output optical power thermo-optically. Due to the thermo-optic effect, the rise in temperature along the sensing arm changes the refractive index of the claddings nearby as well as the effective index of the mode travelling along the waveguide, resulting in a change in optical path length and creating a phase shift relative to the reference arm. As the injected current varies, the phase shift changes between constructive and destructive interference conditions.

If the TOC of the dielectric material that forms the claddings is negative (*e.g.* Cytop), an interesting effect will occur when the metal stripe is heated. As heat diffuses from the metal stripe into the surrounding claddings, a temperature gradient higher in the center and lower in the nearby region is formed. The negative TOC of the claddings will convert this temperature gradient to a negative gradient of refractive index, lower in the center and higher in the nearby region, in other words, an antiguide. This will inhibit the propagation of the LRSPP

mode due to radiation leakage of optical power. When the density of injected electrical current is strong enough, the attenuation becomes so high that the LRSPP mode is cut off entirely.

Another effect is the burning out of the metal stripe when the injected electrical current is too large. This is due to electromigration which happens when the heavy positive ions constituting the metal are displaced due to the strong electron-wind colliding on them [48,49].

A third effect that may be taken into consideration is glass transition, depending on the material used for the claddings. Some materials have a glass transition temperature T_g beyond which it changes from glassy to rubbery which causes permanent damage to the waveguide.

Therefore, it is important to properly control the density of the electrical current in conducting thermo-optic experiments in order to prevent the antiguide effect from cutting off the LRSPP mode and the electromigration effect and glass transition effect from damaging the waveguide.

2.1.2 Theoretical expectation

Assuming that the two Y-junctions of the single-output MZI are designed for equal power split and combine, the expression for the output power of the MZI is given below following Ref.[11]:

$$P_{out} = P_{in} A W \frac{1}{2}\left[1 + V\cos\left(\phi + \phi_0\right)\right] \tag{2.1}$$

where

$$A = A_{ATT} A_{RL} A_{TL} \tag{2.2}$$

$$A_{ATT} = \exp\left(-2\alpha L_t\right) \tag{2.3}$$

$$A_{RL} = \exp\left(-2\rho\theta_t\right) \tag{2.4}$$

$$A_{TL} = \exp\left(-2\tau_t\right) \tag{2.5}$$

$$V = \frac{1}{\cosh\left(\Delta\alpha L_s + \Delta\rho\theta_s + \Delta\tau\right)} \tag{2.6}$$

$$W = \exp\left[-\left(\Delta\alpha L_s + \Delta\rho\theta_s + \Delta\tau\right)\right]\cosh\left(\Delta\alpha L_s + \Delta\rho\theta_s + \Delta\tau\right) \tag{2.7}$$

in which P_{in} and P_{out} are the input and output optical powers; A is the total loss factor of the MZI, consisting of three separate factors A_{ATT} for attenuation, A_{RL} for radiation loss, and A_{TL} for transition loss, where the latter two losses can be determined in dB as $-10\log_{10}A_{RL}$ and $-10\log_{10}A_{TL}$ (usually express as TL); α and $\Delta\alpha$ are the mode field attenuation of the reference arm and the difference in mode field attenuation of the sensing arm relative to the reference arm, L_t and L_s are the total path length and length of the active region on the sensing arm, ρ and $\Delta\rho$ are coefficients that characterise the radiation loss of the reference arm and the difference in radiation loss between the two arms, θ_t and θ_s are the total bending angle of all the curved sections of the MZI and the bending angle of the active region on the sensing arm, τ_t and $\Delta\tau$ are coefficients that characterise the total transition loss of the MZI and the difference in transition loss between the arms; ϕ and ϕ_0 are the phase shift introduced by thermo-optic modulation, and the initial phase difference between the arms; V is the visibility factor of the MZI representing the peak-to-valley difference of the output power, and W is the unbalance factor representing the power penalty due to $\Delta\alpha$, $\Delta\rho$, and $\Delta\tau$.

Under normal operation, the electrical current injected to heat the sensing arm is small enough such that $\Delta\alpha$, $\Delta\rho$, and $\Delta\tau$ should be negligible. In this case V and W are close to 1, and Eq.(2.1) simplifies to

$$P_{out} = P_{in} A \frac{1}{2}\left[1 + \cos\left(\phi + \phi_0\right)\right] \tag{2.8}$$

which shows that the output optical power is a sinusoidal function of the phase.

2.1.3 Phase shift versus dissipated electrical power

The measurements are data points of output optical power versus dissipated electrical power instead of thermally induced phase shift. In order to compare them directly, it is necessary to derive a general relation between the dissipated electrical power and the phase shift.

Firstly, the relation between the phase shift and the thermally induced change in effective index of the LRSPP mode is known to be linear, given as

$$\phi = \frac{2\pi L_s}{\lambda} \Delta n_{eff} \tag{2.9}$$

where λ is the working wavelength (1310 nm), and Δn_{eff} is the thermally-induced change in effective index of the LRSPP mode propagating along the arms.

Secondly, it is known from the linear modal of the thermo-optic effect that when the temperature is changed in a range that is not too large (*e.g.* up to ~100 ^{o}C [6]), the thermally-induced index change of the cladding material is linearly related to the change of temperature. Assuming that the effective index of the mode changes linearly with the refractive index of the cladding material by a constant factor of C_n, we have the following relation:

$$\Delta n_{eff} = C_n \left[\frac{dn}{dT}\right] \Delta T \tag{2.10}$$

where the TOC of Cytop which is used as the cladding material of our device is taken as $dn/dT = -5\times10^{-5}$ $^{\circ}$C^{-1} [50]. The change in temperature during the experiments is estimated by

measuring the change in resistance of the metal stripe in the active region, based on the relation in Ref.[5]:

$$R = R_0(1 + \delta\Delta T) \tag{2.11}$$

where R and R_0 are the resistance of the metal stripe measured in and before the experiment, respectively. The temperature coefficient of resistivity of Au used for the metal stripe is taken as $\delta = 1.3876\times10^{-3}$ ($^{\circ}C^{-1}$). The estimated temperature range in the experiments is ~70°C, satisfying the precondition to apply the linear model of thermo-optic effect.

Finally, we need to relate ΔT to the dissipated electrical power P_e. Here an assumption is made that the rise in temperature is linear with the electrical power dissipated along a unit length of the metal stripe P_e/L_s by a constant factor C_T, which gives us the following relation:

$$P_e = C_T L_s \Delta T \tag{2.12}$$

the validity of which is verified by fitting the measurements to theoretical expectation. Now, the relation between P_e and ϕ can be derived from Eqs. (2.9), (2.10), and (2.12). By combining the constant factors as $C = C_n/C_T$, we obtain

$$\phi = \frac{2\pi}{\lambda}\left[\frac{dn}{dT}\right]CP_e \tag{2.13}$$

where the constant factor C is also determined by fitting. The slope of this relation $(2\pi/\lambda)(dn/dT)C$ depends only on the cross-sectional dimensions of the waveguide.

2.2 Experimental

2.2.1 Device of interest

Fig. 2.1 illustrates a front cross-sectional sketch of a chip on which the device of interest is fabricated, comprising several waveguides each formed as a thin narrow Au stripe embedded

in Cytop claddings. The whole device was supported by a 450 μm thick silicon substrate on which a 10 μm bottom cladding layer made of Cytop was spin-coated. A gold layer of 35 nm was then deposited on the bottom cladding and patterned in a lift-off lithography process by removing the gold in predetermined regions according to the layout. Then another 10 μm thick Cytop layer was coated as the top cladding to fully embed the Au structures in a symmetric Cytop environment. Fabrication details can be found in Ref.[51].

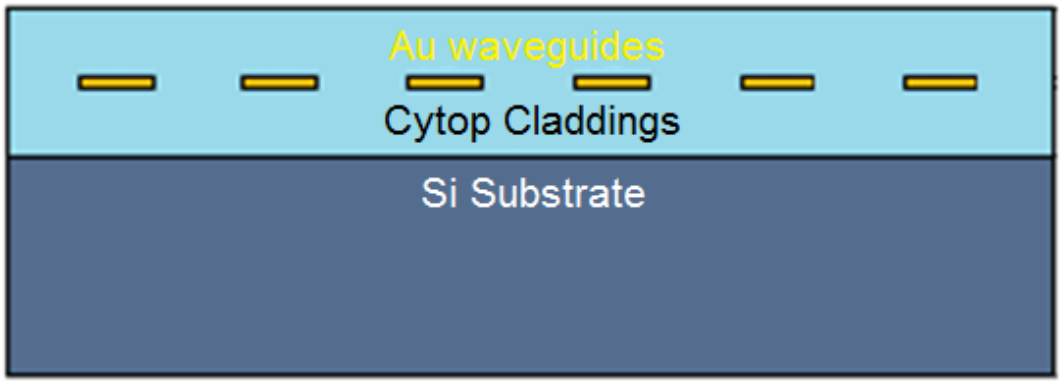

Fig.2.1. Front cross-sectional view of a chip.

The device of interest is a single-output MZI with a designed operating wavelength of 1310 nm, which consists of two straight sections at the input and output ends and a few curved sections in between them, as shown in Fig. 2.2 (a). All the Au stripes along the waveguides have dimensions of 5 μm in width, 35 nm in thickness. All the curved sections have the same radius of curvature of 5.5 mm. There are two designs of the single-output MZIs, one is 3.8 mm long with a 240 μm separation between the arms, the other is 3 mm long with a 140 μm separation between the arms. Both use Y-junctions with a 2 μm inner waveguide separation at the split/combine point. All the chips on which the single-output MZIs are fabricated originate from the same wafer (identified internally as CWS 19).

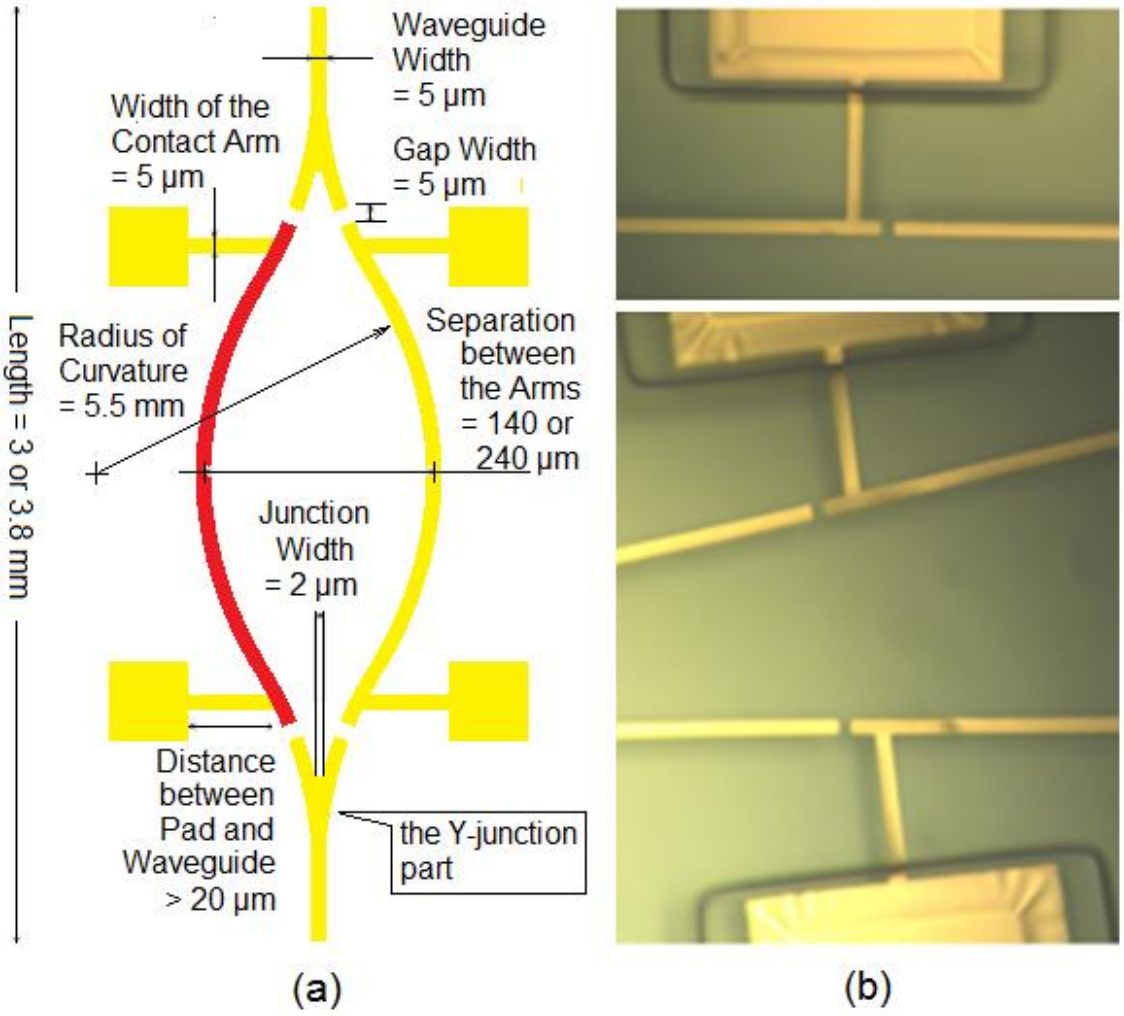

Fig.2.2. (a) Sketch of a single-output MZI showing dimensions, and

(b) microscope images showing the features required for thermo-optic control.

Additional features are added in order to apply thermo-optic modulation to the device, including metal pads, contact arms and gaps, as shown in Fig. 2.2 (b). The pads are used to accommodate the electrical probes used to inject an electrical current into the active region of the waveguide, the Au stripe highlighted in red in Fig. 2.2 (a). In the active region, the Au stripe is used as both an element of the optical waveguide and the electrical wire for the current to pass through. The top cladding of the pads are etched to expose the metal contacts for electrical probes. The pads are kept at least 20 μm away from the waveguides to prevent

optical interference, as most of the power of the LRSPP mode is contained within a 3 μm distance from the waveguide. Contact arms with the same thickness and width as the waveguides are used to connect the pads to the waveguides. 2 μm gaps are used to isolate the electric current from the rest of the device while introducing no significant optical loss along the waveguide.

2.2.2 Experimental setup

Fig. 2.3 illustrates the setup used in the thermo-optic experiments. Light at a free-space wavelength of 1310 nm from a laser is put into the chip under test though a polarisation maintaining fiber (PMF). The output light is first collected by a microscope objective and received by a CCD camera to find the LRSPP mode by adjusting the fiber-waveguide alignment, and then is coupled into a single mode fiber (SMF) connected to a power meter to measure the output optical power. Two electrical probes are attached to the pads of the waveguide connecting the active region with a power supply and a multi-meter, forming a closed electrical circuit. The power supply injects electrical current into the active region to generate heat that enables thermo-optic modulation. The power meter, multi-meter and power supply are connected to a computer with GPIB cables, allowing LabVIEW programs to control the voltage applied to the chip, and record the current passing through the Au stripe in the active region on the sensing arm, and the output optical power on the power meter. In our experiments, the thermo-optic control was conducted by applying an increasing voltage in steps of 0.01 V every 0.5 s.

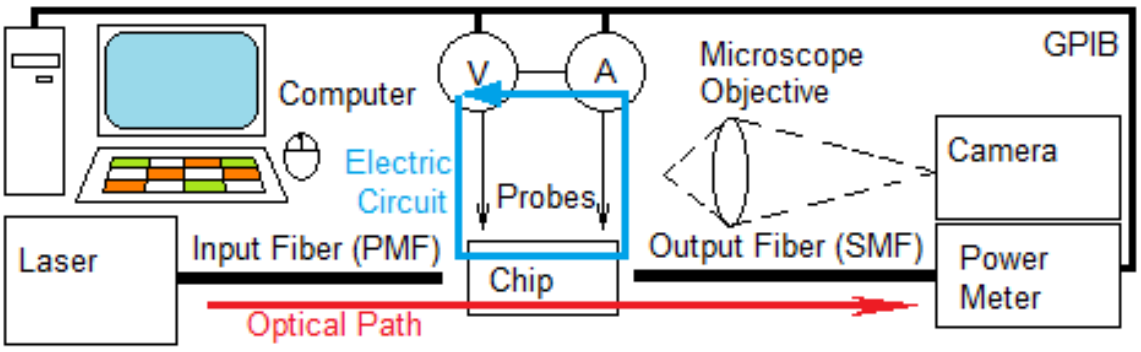

Fig.2.3. Block diagram of the experimental setup for the thermo-optic measurements.

2.2.3 Experiments on 3.8 mm long MZIs

Fig. 2.4 shows the results obtained from a 3.8 mm long MZI with a separation of 240 μm between the arms. It is calculated from the layout that for this MZI we have L_s = 1.62 mm and L_t = 3.81 mm. The output optical power versus dissipated electric power is plotted in Fig.2.4 and compared with theory for which the input power was taken as P_{in} = 1.83 mW, the attenuation α = 0.691 mm^{-1} (6dB/mm), the total radiation coefficient $\rho\theta_t$ = 0.039 (0.34dB), the total transition coefficient τ_t = 0.599 (5.2dB), and the nominal phase shift between the arms as ϕ_0 = -0.2π, all adjusted by optimizing the fit between the theoretical and experimental responses, with α, $\rho\theta_t$ and τ_t close to the modeling results reported in Ref. [52]. The slope in Eq. (2.13) found in the fitting is $(2\pi/\lambda)(dn/dT)C$ = 1.25 rad/mW.

It is observed that the measurements generally follow the model except at the largest dissipated powers. They start to deviate from theory when the dissipated power is 13 mW, corresponding to an injected current of 4.6 mA. This is possibly because the temperature therein is so high that the antiguide effect in the sensing arm becomes strong, weakening the interference between the arms. Another possible cause is that the temperature is approaching the glass transition temperature of the Cytop claddings at T_g = 108˚C [7] and a linear

dependence of refractive index on temperature may no longer hold since permanent change in the claddings near the Au stripe may occur.

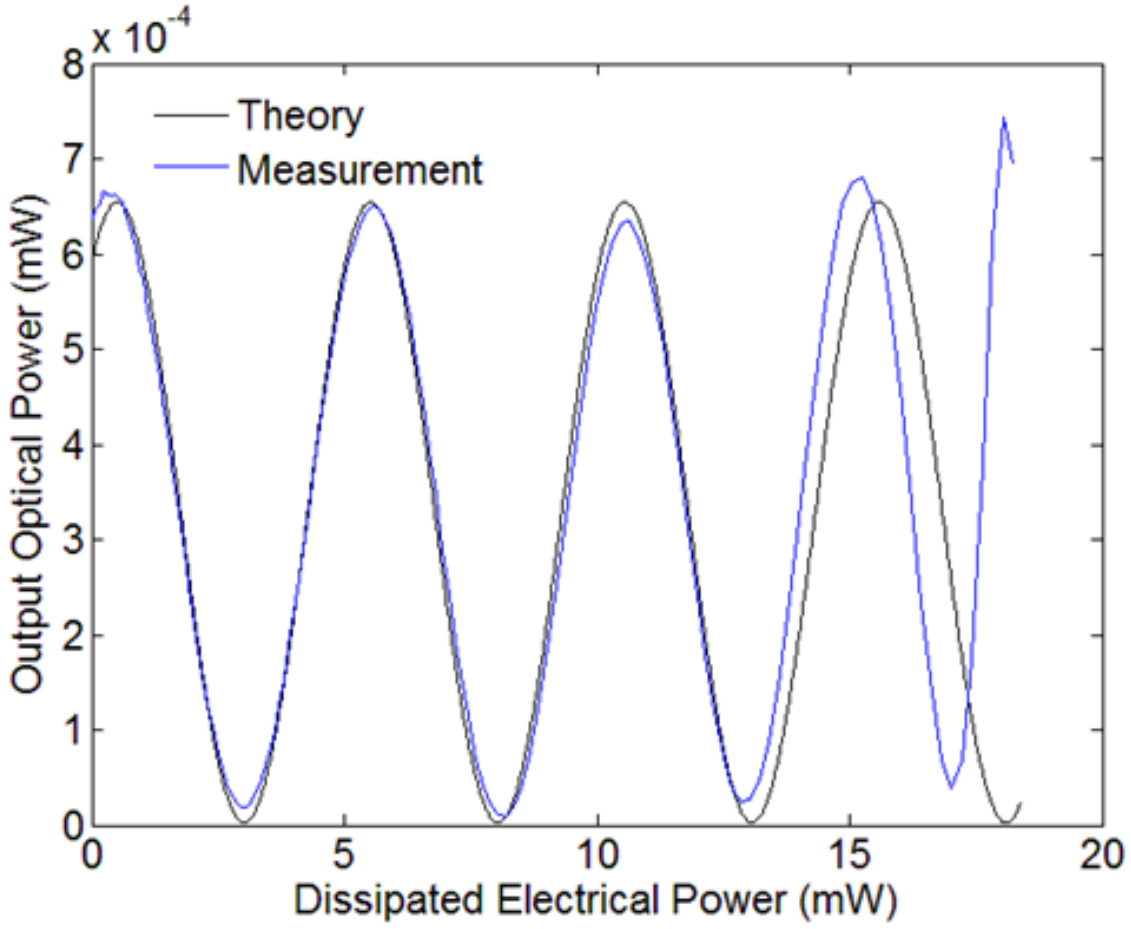

Fig. 2.4. Output optical power versus dissipated electrical power for a 3.8 mm long MZI [13].

2.2.4 Experiments on 3.0 mm long MZIs

A MZI with a length of 3 mm, a separation of 140 μm between the arms was also tested. It is calculated from the layout that for this MZI we have L_s = 1.28 mm and L_t = 3.01 mm. The comparison of theory to the measured output optical power versus dissipated electric power is shown in Fig.2.5. The parameters used for the fitting were P_{in} = 1.78 mW, α = 0.576 mm^{-1} (5dB/mm), $\rho\theta_t$ = 0.030 (0.26dB), τ_t = 0.599 (5.2dB), and ϕ_0 = -0.83π. The slope of Eq. (2.13) is found as $(2\pi/\lambda)(dn/dT)C$ = 1.35 rad/mW, which is close to that of the longer MZI case

(1.25 rad/mW). Fabrication inconsistencies among structures and waveguide deformation could be the causes for the difference [51,52]. Again, we observe a deviation from sinusoidal at the largest dissipated powers possibly due to the same reasons as in the longer MZI case.

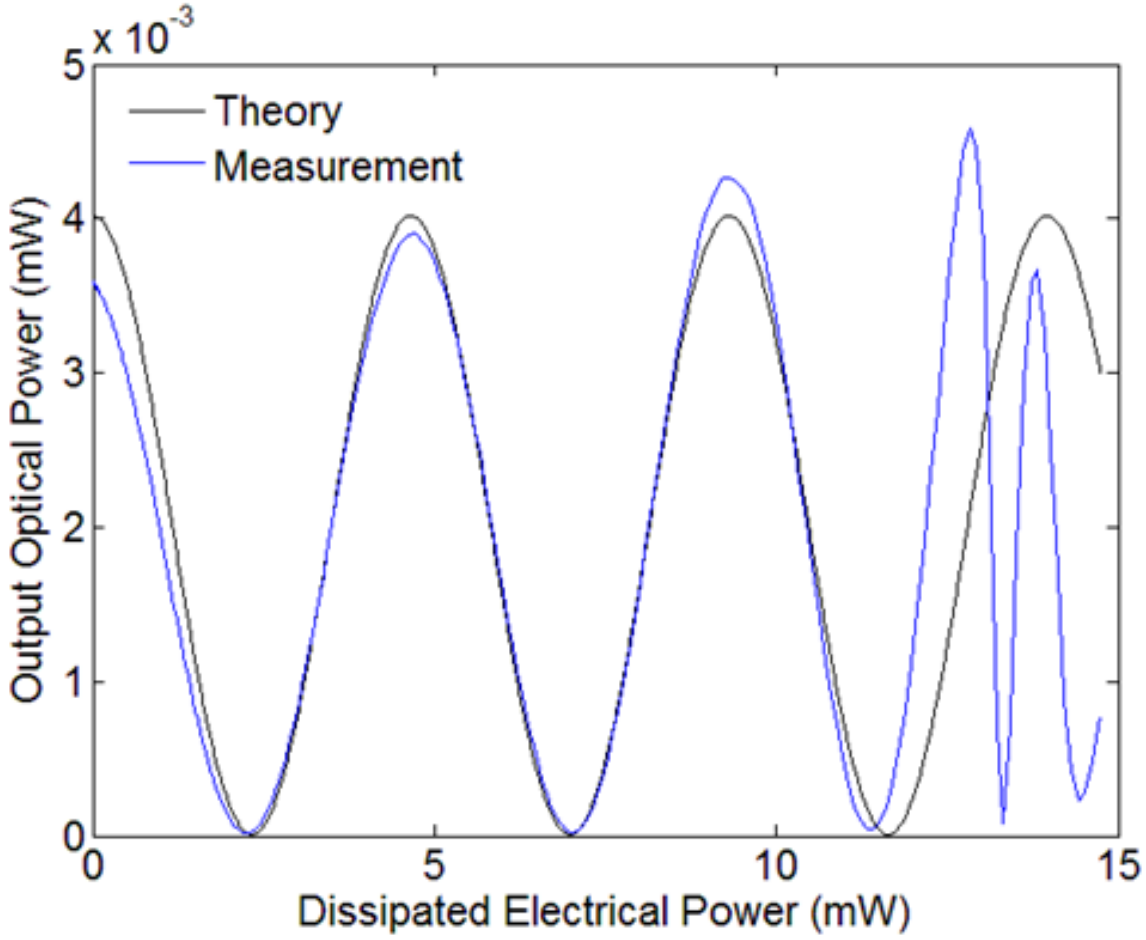

Fig. 2.5. Output optical power versus dissipated electrical power for a 3.0 mm long MZI [13].

2.3 Summary

This chapter shows the switching ability of the single-output MZIs, indicating that thermo-optic functions can be enabled in Cytop and providing a basis for thermo-optic sensing on multiple output MZIs. Thermo-optic characterisation was conducted on single-output MZIs of two different dimensions operating at 1310 nm by heating the active region on the sensing

arm with electrical current injected through metal probes. The measured output power versus dissipated electrical power agreed well with fitted theory except at high dissipated powers. The deviations from a sinusoidal response may be due to the beginning of mode cut off in the heated arm with high temperature. Proximity to the glass transition temperature of Cytop may also be a cause. The results show that as long as the driving currents are low enough to avoid memory effects and deformation due to changes in the polymer, Cytop-cladded LRSPP devices based on MZI structures can be used in thermo-optic sensing.

2.4 Contribution

The results provided in this chapter contributed to part of an article published in *Applied Optics* as Ref.[13]. I designed and built the experimental setup; I generated and interpreted the theoretical and experimental results, and wrote the manuscript. Prof. Berini contributed to the design of the experiments and experimental setup, the interpretation of the results, and revised the manuscript. Charles Chiu fabricated the devices used in the experiments.

Chapter 3

Thermo-optic sensing using LRSPP dual-output MZIs

3.1 Summary

In this chapter, the characterization of dual-output Mach-Zehnder interferometers operating with long-range surface plasmon-polaritons at a free-space wavelength of ~1370 nm is reported. The devices were constructed by embedding Au stripes in Cytop claddings, and consist of a symmetric Mach-Zehnder interferometer in cascade with a 50:50 coupler. By injecting electric current via probes to generate heat in the active region in one arm of the interferometer, a phase difference between the arms was thermo-optically induced, modulating the optical power of the two outputs. The outputs were complementary as expected theoretically, thus demonstrating the switching abilities of the structure. The advantages for sensing applications of a dual-output interferometer over a single-output one are a 2× larger dynamic range and the ability to cancel common noise and source fluctuations. The larger dynamic range and noise cancellation produced a minimum detectable phase shift 4× lower than obtained by monitoring a single output. The smallest value of $\Delta\phi_{min}$ obtained was ~ 3 mrad.

3.2 Contribution

The results provided in this chapter were published as an article in the *Journal of Lightwave Technology*. I designed and built the experimental setup; I developed the theoretical model; I generated and interpreted the theoretical and experimental results, and wrote the manuscript.

Prof. Berini contributed to the design of the experiments and experimental setup, the interpretation of the results, and revised the manuscript. Hamoudi Asiri fabricated the devices used in the experiments.

3.3 Errata

The discussion from Eq.(3.13) to (3.16) in the published article should be replaced by the discussion in Section 2.1.3. Also, the term S is missing at the end of Eq.(4.5). These errors do not change any of the results nor the conclusions reached.

3.4 Article

The published article follows verbatim.

Noise Cancellation in Long-Range Surface Plasmon Dual-Output Mach-Zehnder Interferometers

Hui Fan and Pierre Berini

Abstract—**The characterisation of dual-output Mach-Zehnder interferometers operating with long-range surface plasmon-polaritons at a free-space wavelength of ∼1370 nm is reported. The devices were constructed by embedding Au stripes in Cytop claddings, and consist of a symmetric Mach-Zehnder interferometer in cascade with a 50:50 coupler. By injecting electric current via probes to generate heat in the active region in one arm of the interferometer, a phase difference between the arms was thermo-optically induced, modulating the optical power of the two outputs. The outputs were complementary as expected theoretically, thus demonstrating the switching abilities of the structure. The advantages for sensing applications of a dual-output interferometer over a single-output one are a 2X larger dynamic range and the ability to cancel common noise and source fluctuations. The larger dynamic range and noise cancellation produced a minimum detectable phase shift 4X lower than obtained by monitoring a single output. The smallest value of $\Delta\phi_{\min}$ obtained was ∼3 mrad. The structure is especially promising for (bio)chemical sensing applications.**

Index Terms—**Dual-output Mach-Zehnder interferometer, long-range surface plasmon-polariton, noise cancellation, thermo-optic modulation.**

I. Introduction

SURFACE plasmon-polaritons (SPPs) are surface waves that propagate along the interface of a metal and a dielectric as a transverse-magnetic (TM) polarised mode [1]–[3], with fields peaking at the interface and decaying exponentially into both media. A symmetrically-cladded thin metal slab (infinite width) allows the SPPs at the two interfaces to bound, forming two supermodes, with the symmetric one known as the long-range SPP (LRSPP) for its comparably low attenuation [4]. A thin metal stripe (finite width) with symmetric claddings provides additional confinement in the lateral direction and supports several LRSPP modes [5]; the fundamental one exhibits a Gaussian-like field distribution and is useful for integrated optics elements [6]–[8].

Manuscript received December 21, 2012; revised April 29, 2013; accepted June 17, 2013. Date of publication June 26, 2013; date of current version July 17, 2013.

H. Fan is with the School of Electrical Engineering and Computer Science, University of Ottawa, Ottawa, Ontario K1N 6N5, Canada [redacted]

P. Berini is with the School of Electrical Engineering and Computer Science, and the Department of Physics, University of Ottawa, Ottawa, Ontario K1N 6N5, Canada [redacted]

Color versions of one or more of the figures in this paper are available online at http://ieeexplore.ieee.org.

Digital Object Identifier 10.1109/JLT.2013.2271217

Thermo-optic modulation and switching of LRSPPs have been explored as potential applications. Keeping the pressure and operating wavelength constant, the refractive index of a material changes linearly with temperature over a small temperature range (e.g. less than ∼ 100°C [9]), as follows:

$$n(T) = n(T_0) + (T - T_0)\frac{dn}{dT} \tag{1.1}$$

where n is the refractive index and T is the temperature. The variation of refractive index as a function of temperature $\mathrm{d}n/\mathrm{d}T$ is called the thermo-optic coefficient (TOC). This effect has motivated the investigation of variable optical attenuators (VOAs) based on thermally-induced anti-guiding in embedded Au stripes in polymer such as benzocyclobutene (BCB) [10], ZPU [11] and Cytop [12], on mode cut-off due to thermally-induced index asymmetry [13], [14], and on single-output Mach-Zehnder interferometers (MZIs) where the thermally-induced phase shift on one arm induces constructive and destructive interference conditions [12], [15]. Thermo-optic switches based on couplers have also been reported [15].

MZIs are widely used for modulation and sensing applications, e.g., electro-optic modulation [16], [17] and biochemical probing [18], [19]. MZIs providing two complementary outputs [20], henceforth referred to as dual-output MZIs, are very interesting. They can be used as switching structures or as sensing structures. As sensing structures, they provide in differential mode twice the signal swing (dynamic range) relative to using a single output. Furthermore, the two outputs can be used to suppress common noise and power fluctuations due to, e.g., changes in input laser power or coupling conditions.

In the past, fiber interferometers with 2 × 2 or 3 × 3 directional couplers were demonstrated [21], [22]. Research on multiple output MZIs based on dielectric waveguides has been conducted [23], [24]. Surface plasmon resonance schemes were also applied to MZIs [25], [26], but mainly single-output. Dual-output MZIs operating with surface plasmons of any kind (including LRSPPs) have yet to be demonstrated. Given the advantages and potential applications of such structures, there is a strong motivation to investigate them. Recent work has focused on researching and fabricating metal stripe devices cladded with Cytop [7], [27] (an amorphous fluoropolymer with a refractive index close to that of water [28], $n \sim 1.334$) for biosensing applications with LRSPPs [29].

We have fabricated thermo-optic dual-output MZIs as Au stripes in Cytop supporting LRSPPs in order to investigate their phase (switching) and noise suppression characteristics for eventual application to biosensing. The paper is organized as follows: Section II describes the device architecture and the experimental setup and procedures. Section III discusses

0733-8724/$31.00 © 2013 IEEE

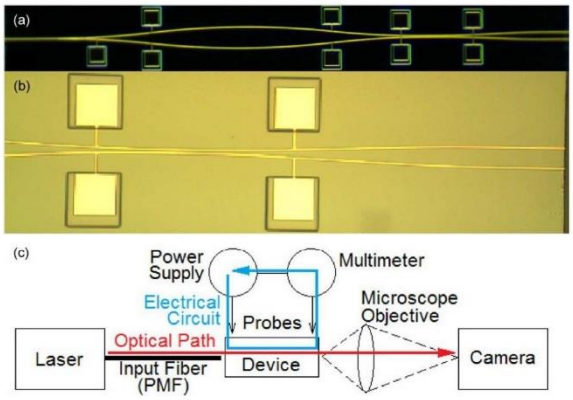

Fig. 1. Device and setup: Microscope image of (a) the whole dual-output MZI device and (b) the coupling structure on the device. (c) Block diagram of the thermo-optic experimental setup.

theoretically the operation of the devices and compares the measured transfer characteristics with theory. Section IV demonstrates the noise cancellation abilities of the structure. Section V concludes the paper.

II. Device Architecture and Experimental Setup

Fig. 1(a) shows a microscope image of a fabricated device of interest in this paper—a dual-output MZI consisting of a symmetric MZI in cascade with a 3 dB (50:50) coupler producing outputs that are complementary. The structure was designed for operation at a free-space wavelength of 1310 nm, is implemented with Au waveguides 35 nm thick, 5 μm wide, and is 3.8 mm long. All curved sections have the same radius of curvature of 5.5 mm. The MZI has a Y-junction splitter with a 2 μm inner waveguide separation at the split and a separation of 140 μm between its two arms at the widest point. The 3 dB coupler has a coupled length of 100.25 μm, a coupled separation of 3.5 μm, and a separation of 46 μm between its two output ports. A high-magnification microscope image of the coupler and its outputs is given in Fig. 1(b). Details on the modelling and design of the constitutive components can be found in [7].

The devices were fabricated by first depositing a 10 μm thick Cytop layer forming the bottom cladding on a 450 μm thick silicon substrate, followed by a 35 nm thick Au layer patterned through a lift-off lithography process, then another 10 μm thick Cytop layer forming the upper cladding (such that the waveguides are optically symmetric [5]). Fabrication details can be found in [27], [30]. Additional features are added for thermo-optic control as shown in Figs. 1(a) and (b), including metal pads and contact arms to connect to the electric probes, as well as gaps to isolate the current to the active region of the Au stripe. The pads are placed 20 μm away from the waveguides and the gaps are 2 μm long in order to remain optically non-invasive. The active region, consisting of one arm of the MZI, is heated between two contact pads by the injected current, changing the refractive index of the surrounding Cytop claddings, and inducing a phase difference between the LRSPP modes travelling in the two arms of the MZI. All tested devices originate from the same wafer (identified internally as ND II).

Fig. 1(c) illustrates the block diagram of the experimental setup. Light at ~1310 nm in free-space wavelength from a tunable laser is input into the device through a butt-coupled polarisation maintaining fiber (PMF), and the LRSPP modes emerging from both outputs are captured by a single microscope objective and a CCD camera, constituting the optical path. An electrical circuit is formed by contacting an arm of the MZI to two metal probes which are connected to a power supply and a multi-meter, so as to inject an electrical current into the waveguide to generate heat for the thermo-optic modulation. The power supply, the multi-meter, and the camera are controlled by LabVIEW programs to apply voltages, read currents, and measure the optical powers within two pre-set apertures on the output mode image using frame grabber and laser beam analysis software (LBA-710PC, Ophir Spiricon). Output images are captured in real time but are post-processed using Matlab, where the magnitude proportional to the intensity of each pixel within each aperture is summed (integrated) as a measure of the total power within each. Calibration is then achieved by carrying out the same procedure for an incident beam of known power. In this method the powers of both outputs are captured simultaneously so common noise can be cancelled out.

III. Transfer Characteristic

Theoretically, the optical powers emerging from the two output ports are sinusoidal and complimentary. Following Appendix A, the two output optical powers can be determined and expressed as:

$$\begin{aligned} P_1 = &\frac{1}{2}P_{in}\frac{1}{4}A_{out} \\ &\times \Big[(A_+ + A_-)(A_s + A_r) \\ &\quad + 2\sqrt{A_+A_-}(A_s - A_r)\cos(2|\kappa|L_c) \\ &\quad + 2(A_+ - A_-)\sqrt{A_sA_r}\cos(\phi_D + \phi_0) \\ &\quad + 4\sqrt{A_+A_-}\sqrt{A_sA_r}\sin(2|\kappa|L_c)\sin(\phi_D + \phi_0)\Big] \end{aligned} \quad (3.1)$$

and

$$\begin{aligned} P_2 = &\frac{1}{2}P_{in}\frac{1}{4}A_{out} \\ &\times \Big[(A_+ + A_-)(A_s + A_r) \\ &\quad - 2\sqrt{A_+A_-}(A_s - A_r)\cos(2|\kappa|L_c) \\ &\quad + 2(A_+ - A_-)\sqrt{A_sA_r}\cos(\phi_D + \phi_0) \\ &\quad - 4\sqrt{A_+A_-}\sqrt{A_sA_r}\sin(2|\kappa|L_c)\sin(\phi_D + \phi_0)\Big] \end{aligned} \quad (3.2)$$

Using the above, the difference and sum of the two powers are determined as:

$$\begin{aligned} P_1 - P_2 = &\frac{1}{2}P_{in}A_{out}\sqrt{A_+A_-}\Big[(A_s - A_r)\cos(2|\kappa|L_c) \\ &+ 2\sqrt{A_sA_r}\sin(2|\kappa|L_c)\sin(\phi_D + \phi_0)\Big] \end{aligned} \quad (3.3)$$

and

$$P_1 + P_2 = \frac{1}{2} P_{in} A_{out} \left[\frac{(A_+ + A_-)}{2} (A_s + A_r) + (A_+ - A_-)\sqrt{A_s A_r} \cos(\phi_D + \phi_0) \right] \quad (3.4)$$

Thus the normalized power difference between the two outputs is expressed as

$$\frac{P_1 - P_2}{P_1 + P_2} = \frac{\sqrt{A_+ A_-}\left[\cos(2|\kappa|L_c)(A_s - A_r) + 2\sqrt{A_s A_r}\sin(2|\kappa|L_c)\sin(\phi_D + \phi_0)\right]}{\frac{A_+ + A_-}{2}(A_s + A_r) + (A_+ - A_-)\sqrt{A_s A_r}\cos(\phi_D + \phi_0)} \quad (3.5)$$

In these equations, we have:

$$A_s = \mathrm{e}^{-2(\alpha L_t + \Delta\alpha_S L + \rho\theta_0 + \Delta\rho_S\theta + \tau_0 + \Delta\tau_S)} \quad (3.6)$$

$$A_r = \mathrm{e}^{-2(\alpha L_t + \rho\theta_0 + \tau)} \quad (3.7)$$

$$A_+ = \mathrm{e}^{-2(\alpha_+ L_C - \rho_+\theta_C - \tau_+)} \quad (3.8)$$

$$A_- = \mathrm{e}^{-2(\alpha_- L_C - \rho_-\theta_C - \tau_0)} \quad (3.9)$$

$$A_{out} = e^{-2(\alpha L_{out} + \rho\theta_{out} + \tau_{out})} \quad (3.10)$$

L_t, L, L_c and L_{out} are the total and active path length of the MZI, the coupled length of the coupler, and the path length after the coupler. κ is the coupling coefficient and $|\lambda|L_c$ is the coupling angle. σ and $\Delta\alpha$ are the mode field attenuation of the reference arm and the difference in the attenuation of the heated arm relative to the reference arm of the MZI, and α_+ and α_- are those of the symmetric and asymmetric supermodes of the coupler [20]. θ_0, θ and θ_c are the total bending angle of the curved sections of the MZI, the bending angle of the active region, the total bending angle of the coupler, and the total bending angle after the coupler. ρ and $\Delta\rho_s$ are coefficients that characterise the radiation loss of the reference arm and the difference in the radiation loss between the arms, and ρ_+ and ρ_- are those of the symmetric and asymmetric supermodes of the coupler. A radiation coefficient ρ at a curved section θ is defined (for convenience) as $e^{-2\rho\theta} = R$ where the radiation loss of the section is determined in dB as $-10\log_{10} R$. τ_0 and $\Delta\tau_s$ are coefficients that characterise the total transition loss of the MZI and the difference in transition loss between the arms, τ_+, and τ_- are those of the symmetric and asymmetric supermodes of the coupler, and τ_{out} is that of the section after the coupler. Transition losses include butt-coupling losses at the input and output facets of the die, the transition losses at the taper of the Y-junction splitter, and transition losses at the intersections between curved sections bending in opposite directions [7]. A transition coefficient τ at a junction is defined (for convenience) as $e^{-2\tau} = T_r$ where T_r is the transmittance of the junction and $\mathrm{TL} = -10\log_{10} T_r$ is the transition loss in dB. ϕ_D and ϕ_0 are the phase difference introduced by the thermo-optic modulation, and the initial phase difference between the arms. A_s and A_r are loss factors applied to the modes coming out of the MZI part and entering the coupler from the sensing and reference arms, A_+ and A_- are those of the symmetric and asymmetric supermodes of the coupler, and A_{out} is that of the section after the coupler.

For our 3-dB coupler design, A_+ and A_- are similar, in which case (3.5) simplifies to:

$$\frac{P_1 - P_2}{P_1 + P_2} = \frac{A_s - A_r}{A_s + A_r}\cos(2|\kappa|L_c) + 2\sqrt{A_s A_r}|A_s + A_r \sin(2|\kappa|L_c \sin(\phi_D + \phi_0)) \quad (3.11)$$

Under small dissipated electrical power, $\Delta\alpha_s$, $\Delta\rho_s$ and $\Delta\tau_s$ are negligible causing A_s and A_r to be generally the same, and (3.11) can be simplified to:

$$\frac{P_1 - P_2}{P_1 + P_2} = \sin(2|\kappa|L_c)\sin(\phi_D + \phi_0) \quad (3.12)$$

For the case of a 3 dB coupler (50:50 split), $\sin(2|\kappa|L_c) = 1$ and the above simplifies further, such that the normalized optical power difference is a sinusoidal function of the phase difference only.

Experiments were performed to verify the operation and complimentary of the two outputs by applying an increasing voltage in steps of 0.01 V every 0.5 s on one arm, and recording the current passing through and the optical powers emerging from the two ports. Figs. 2(a) and (b) show the optical output powers and the normalized powers measured at the wavelength of 1373 nm versus dissipated electrical power. The theoretical normalised power difference given by (3.12), in which the coupling angle was $|\kappa|L_c = 0.175\pi$ for $L_c = 100.25$ μm and the nominal phase shift between the arms was $\phi_0 = 0.03\pi$ (both adjusted by optimising the fit between theory and measurements) is also plotted in Fig. 2(b). The wavelength of the input light was tuned to 1373 nm so that the coupler would operate near its 3 dB point (the coupler was designed to provide this coupling at 1310 nm but due to fabrication imperfections it occurred at longer wavelength).

Since the measured data consist of optical power versus dissipated electrical power, while the theory is versus phase shift, it is convenient to relate the dissipated electrical power to the heat-induced phase difference as:

$$\phi_D = \frac{2\pi}{\lambda}\frac{dn}{dT} C_{st} P_e \quad (3.13)$$

which is obtained by combining (1.1) (using $-5 \times 10^{-5}\ ^\circ\mathrm{C}^{-1}$ [31] as the TOC of Cytop) with the following relations:

$$\phi_D = \frac{2\pi L}{\lambda} n_D \quad (3.14)$$

$$P_e = \frac{L(T - T_0)}{C_{st}} \quad (3.15)$$

Eq. (3.14) gives the phase difference ϕ_D in terms of the thermally-induced effective refractive index difference between the active and reference arms n_D, where λ is the operating wavelength (1373 nm). Eq. (3.15) relates the dissipated electrical power P_e to the temperature T at a specific location in the claddings close to the heated waveguide, and C_{st} is a constant independent of L and only dependant on the cross-section of the

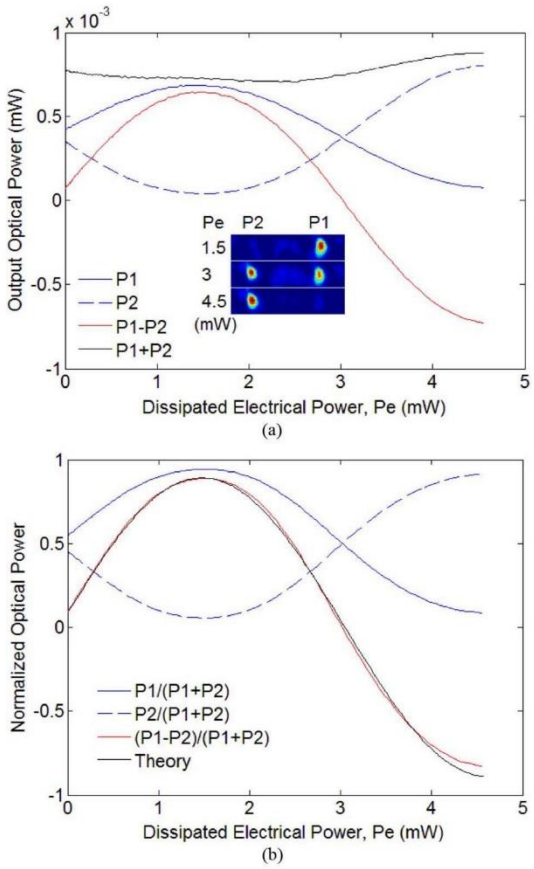

Fig. 2. (a) Output optical powers and (b) normalized optical powers versus dissipated electrical power for the dual-output MZIs.

waveguide. Eq. (3.15) was derived from the thermal equation [13]:

$$\frac{P_e}{L} = -\oint_C K\nabla T \cdot \vec{n} dC \tag{3.16}$$

where $K = 0.12$ W/(m · K) [28] is the thermal conductivity of Cytop, C is a contour passing through the said location and enclosing the cross-section of the waveguide, and $\vec{n}dC$ is an element of contour pointing outward. Eq. (3.13) is linear with a slope of $m = (2\pi/\lambda)(dn/dT)C_{st}$ which depends only on the cross-sectional dimensions of the waveguide; m is extracted from the measurements by fitting and found to be $m = 1$ rad/mW.

It is observed in Fig. 2(b) that the measured normalized power difference $(P_1 - P_2)/(P_1 + P_2)$ coincides very well with theory with only a slight discrepancy at the largest dissipated powers (4 $\sim$ 4.5 mW). This discrepancy occurs because of slight changes in $\Delta\alpha_s$, $\Delta\rho_s$ and $\Delta\tau_s$ so A_s and A_r are no longer equal, and according to (3.11), induce a decrease in the magnitude of the second term without changing appreciably the first term. Another set of curves also plotted in Figs. 2(a) and 2(b) are the optical powers of the two individual outputs which are sinusoidal and complimentary as observed, verifying the prediction of a π phase difference between the outputs, and the sum of the powers which remains essentially constant. It can be observed as well that the power difference of the two outputs provides a dynamic range that is twice as large as the individual power outputs, which emphasises an advantage of the dual-output MZI over its single-output counterpart for a sensing application. A mosaic showing the outputs for three dissipated electrical powers is given as the inset of Fig. 2(a) from which switching is clearly identified.

IV. Noise Cancellation

An advantage of dual-output MZIs is their ability to cancel out common noise from the two outputs. The noise comes mainly from the input and the background light. The causes of the common noise include fluctuations of the input optical power, fluctuations in the fiber-waveguide alignment in the vertical direction, and the evenly distributed background light. In other experiments, there may be additional noises coming from common phase, pressure, and thermal fluctuations, which can also be cancelled when exist. Consider the measured time traces shown in Fig. 3(a), obtained at the operating wavelength of 1373 nm. This experiment was conducted on an identical dual-output MZI as in the previous section, from which the measured output optical powers are plotted versus time. The MZI was biased at a constant voltage of 0.38 V ($P_e =\sim 0.21$ mW) near maximum phase sensitivity, where the output powers are approximately equal and near the mid-point of their full swings (this is where a sensor would be operated). Some common noise is observed on P_1 and P_2, and much of this noise is cancelled by subtracting the two powers, as noted from the traces and the values of standard deviation σ noted on the figure. The common noise can also be reduced by normalisation to the sum of powers, as observed in Fig. 3(b). There are therefore six detection schemes to be assessed and compared statistically.

The average (denoted P) and standard deviation (denoted σ) of P_1, P_2 and $P_1 - P_2$, and of their normalized counterparts, $P_1/(P_1 + P_2)$, $P_2/(P_1 + P_2)$ and $(P_1 - P_2)/(P_1 + P_2)$ were obtained over the time interval of the measurements. The minimum detectable change in P (denoted ΔP_{min}) is given by the corresponding σ times a factor k, which is taken as $k = 2$ in this paper. In order to compare the performance of the six detection schemes, we introduce the minimum detectable phase shift $\Delta\phi_{min}$, defined as:

$$\Delta\phi_{min} = \frac{\Delta P_{min}}{\left|\frac{\partial P}{\partial \phi_D}\right|} = \frac{k\sigma}{\left|\frac{\partial P}{\partial \phi_D}\right|} \tag{4.1}$$

Assuming that the device operates over a small range of dissipated power such that $A_s = A_r = A_m$ (subscript m stands for MZI) and assuming that $A_+ = A_- = A_c$ (subscript c stands for coupler) then P_1 of the dual-output MZI, (3.1), simplifies to:

$$P_1 = \frac{1}{2} P_{in} A_m A_c A_{out} \sin(2|\kappa|L_c) \sin(\phi_D + \phi_0) \tag{4.2}$$

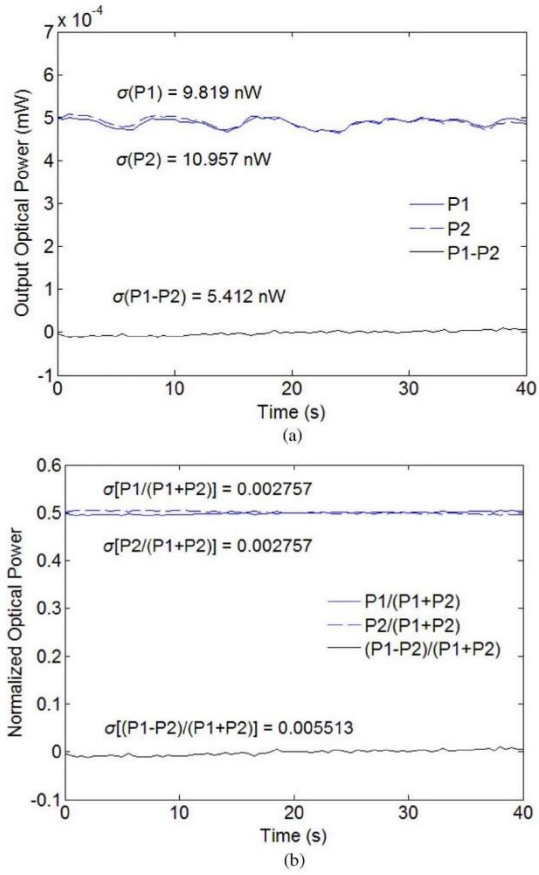

Fig. 3. (a) Output optical power and (b) Normalized optical power from a dual-output MZI versus time.

from which $\partial P_1/\partial\phi_D$ is obtained as:

$$\frac{\partial P_1}{\partial \phi_D} = \frac{1}{2} P_{in} A_m A_c A_{out} S \tag{4.3}$$

where:

$$S = \sin(2|\kappa|L_c)\cos(\phi_D + \phi_0) \tag{4.4}$$

Similarly, we obtain

$$\frac{\partial P_2}{\partial \phi_D} = -\frac{1}{2} P_{in} A_m A_c A_{out} \tag{4.5}$$

$$\frac{\partial (P_1 - P_2)}{\partial \phi_D} = P_{in} A_m A_c A_{out} S \tag{4.6}$$

$$\frac{\partial \left(\frac{P_1}{P_1+P_2}\right)}{\partial \phi_D} = \frac{1}{2} S \tag{4.7}$$

$$\frac{\partial \left(\frac{P_2}{P_1+P_2}\right)}{\partial \phi_D} = \frac{1}{2} S \tag{4.8}$$

$$\frac{\partial \left(\frac{P_1-P_2}{P_1+P_2}\right)}{\partial \phi_D} = S \tag{4.9}$$

TABLE I
STANDARD DEVIATIONS σ AND MINIMUM DETECTABLE PHASE SHIFTS $\Delta\phi_{min}$ FOR P_1, P_2, $P_1 - P_2$, $P_1/(P_1 + P_2)$, $P_2/(P_1 + P_2)$ AND $(P_1 - P_2)/(P_1 + P_2)$ OF FIG. 3 (MEASUREMENT 1) AND FOR ANOTHER SET OF MEASUREMENTS TAKEN WITH DIFFERENT INPUT POWERS

Output Optical Power	Measurement 1 $P_{in}A_mA_cA_{out}$ = 0.976μW		Measurement 2 $P_{in}A_mA_cA_{out}$ = 1.404μW	
	σ	$\Delta\phi_{min}$ (mrad)	σ	$\Delta\phi_{min}$ (mrad)
P_1	9.819 nW	40.24	2.223 nW	6.333
P_2	10.957 nW	44.91	2.590 nW	7.377
P_1-P_2	5.412 nW	11.09	2.180 nW	3.105
$P_1/(P_1+P_2)$	2.757e-3	11.03	7.74e-4	3.096
$P_2/(P_1+P_2)$	2.757e-3	11.03	7.74e-4	3.096
$(P_1-P_2)/(P_1+P_2)$	5.513e-3	11.03	1.548e-3	3.096

Substituting these equations into (4.1), yields the corresponding minimum detectable phase shifts:

$$\Delta\phi_{min}|_{P_1 \text{ or } P_2} = \frac{2}{P_{in}A_mA_cA_{out}} \frac{k}{S}\sigma|_{P_1 \text{ or } P_2} \tag{4.10}$$

$$\Delta\phi_{min}|_{P_1-P_2} = \frac{1}{P_{in}A_mA_cA_{out}} \frac{k}{S}\sigma|_{P_1-P_2} \tag{4.11}$$

$$\Delta\phi_{min}|_{\frac{P_1}{P_1+P_2} \text{ or } \frac{P_2}{P_1+P_2}} = 2\frac{k}{S}\sigma|_{\frac{P_1}{P_1+P_2} \text{ or } \frac{P_2}{P_1+P_2}} \tag{4.12}$$

$$\Delta\phi_{min}|_{\frac{P_1-P_2}{P_1+P_2}} = \frac{k}{S}\sigma|_{\frac{P_1-P_2}{P_1+P_2}} \tag{4.13}$$

$S = 1$ for the case of a 3 dB coupler ($\sin(2|\kappa|L_c) = 1$) and for operation near maximum sensitivity (where $\cos(\phi_D + \phi_0) = 1$), as is the case for the results plotted in Fig. 3. Substituting $S = 1$, $k = 2$, the standard deviations obtained from Fig. 3, and $P_{in}A_mA_cA_{out} = 0.976\ \mu$W for the dual-output MZI under consideration, the values of $\Delta\phi_{min}$ are determined and listed as Measurement 1 in Table I.

Though the standard deviations of the power signals and those of the normalized powers cannot be directly compared, their corresponding minimum detectable phase shifts $\Delta\phi_{min}$ ((4.10) to (4.13)) can be directly compared. Table I, Measurement 1, shows that subtraction of the two power outputs ($P_1 - P_2$) decreased $\Delta\phi_{min}$ by a factor of ~4 relative to that obtained from a single output (P_1 or P_2), implying that significant common noise has been cancelled. The factor of ~4 originates approximately equally from an increase in the dynamic range when taking the difference (i.e., the factor of 2 is absent in (4.11) relative to (4.10)), and a decrease in the standard deviation due to cancellation of common noise (i.e., $\sigma|_{\text{P1}-\text{P2}} \sim 0.5\sigma|_{\text{P1 or P2}}$, Table I).

Comparing $\Delta\phi_{min}$ of $P_1 - P_2$ with those of the three normalized powers ($P_1/(P_1+P_2)$, $P_2/(P_1+P_2)$ and $(P_1-P_2)/(P_1+P_2)$) suggests that slightly better noise cancellation is possible with the latter, although the improvement is in this case very modest. The normalized powers yield the same $\Delta\phi_{min}$ ((4.12)) because $P_1/(P_1+P_2)$ and $P_2/(P_1+P_2)$ have the same standard deviation since they are complementary and the former is expressed as $1-[P_2/(P_1+P_2)]$ (the sum of the two output powers is approximately unchanged). The difference in the normalized powers $(P_1 - P_2)/(P_1 + P_2)$ also yields the same $\Delta\phi_{min}$ because the former can be expressed as $1 - 2[P_2/(P_1 + P_2)]$ and thus has a standard deviation twice as large as the individual

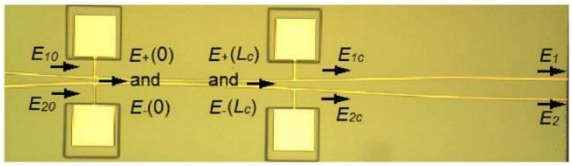

Fig. 4. Notations of the modes travelling from the coupler to the end of the device.

ones (see also Table I), but $\Delta\phi_{min}$ remains the same because the factor of 2 is absent in (4.13) relative to (4.12).

A second set of time traces were obtained on a similar device but under less environmentally perturbative conditions and at slightly higher input power. The results are summarised in Table 2 as Measurement 2. Compared to Measurement 1, lower values of σ and $\Delta\phi_{min}$ are obtained. The standard deviation of the difference $P_1 - P_2$ is only slightly smaller than those of the individual powers, implying less common noise in this experiment. $\Delta\phi_{min}$ decreases by a factor of $\sim$2 in this case because of the increased dynamic range ((4.11) relative to (4.10)). The three normalised powers produce a comparable (slightly lower) $\Delta\phi_{min}$. The smallest value of $\Delta\phi_{min}$ obtained in these experiments was 3.1 mrad.

V. Conclusions

Dual-output MZIs operating in LRSPPs, constructed by cascading a symmetric MZI with a 50:50 coupler, were characterized thermo-optically at a free-space wavelength of $\sim$1370 nm. The waveguides consisted of 5 μm wide and 35 nm thick gold stripes cladded with Cytop, and were heated by injecting electrical current through metal probes into the active region. Expressions for the output powers were determined, and differences and normalisations formed, yielding six possible measurands. The output optical powers were measured simultaneously versus the thermally-induced phase difference between the MZI arms and were observed to be complimentary as expected. The larger dynamic range (2$\times$) of the (un)normalised power difference, compared to a single (un)normalised power output, serves as an advantage. The complimentary outputs also enable noise cancellation by removing common noise from the output powers. The larger dynamic range and noise cancellation abilities produced a minimum detectable phase shift ($\Delta\phi_{min}$) that was 4$\times$ lower than obtained by monitoring a single output. The smallest value of $\Delta\phi_{min}$ obtained was $\sim$3 mrad. Dealing with the two output powers P_1 and P_2 by calculating $(P_1 - P_2)$ or $(P_1 - P_2)/(P_1 + P_2)$ provides not only a 2$\times$ larger dynamic range but also a lower noise level such that a smaller minimum detectable phase shift can be achieved. The structure is promising for sensing applications, including (bio)chemical sensing.

Appendix A

In this appendix the P_1 and P_2 in Section III are derived. The electric fields on the input side of the coupler are noted E_{10} in the modulated arm and E_{20} in the reference arm, as shown in Fig. 4. Omitting the common phase change during the travelling of the mode (which will be cancelled off since the output powers are calculated as $P = |E|^2$), E_{10} and E_{20} are related to the input optical power P_{in} and the loss factors A_s and A_r mentioned in Section III as:

$$E_{10} = \frac{\sqrt{2}}{2}\sqrt{P_{in}}\sqrt{A_s}e^{-j(\phi_D+\phi_0)} \quad (A.1)$$

$$E_{20} = \frac{\sqrt{2}}{2}\sqrt{P_{in}}\sqrt{A_r} \quad (A.2)$$

The electrical field in the reference arm has a loss factor while that in the sensing arm has a loss factor and a phase shift factor. In the coupler, E_{10} and E_{20} are decomposed as the sum of two supermodes denoted $E_+(0)$ and $E_-(0)$, expressed as [20]:

$$E_{10} = Q\left[E_+(0) + E_-(0)\right] \quad (A.3)$$

$$E_{20} = Q\left[E_+(0) - E_-(0)\right] \quad (A.4)$$

where Q is a constant. The supermodes $E_+(0)$ and $E_-(0)$ travel along the coupler. On the output side of the coupler, they become:

$$E_+(L_c) = E_+(0)\sqrt{A_+}e^{-j|\kappa|L_c} \quad (A.5)$$

$$E_-(L_c) = E_-(0)\sqrt{A_-}e^{-j|\kappa|L_c} \quad (A.6)$$

Again, the common phase change is omitted. The E_+ mode receives a negative phase shift while the E_- mode receives a positive one [20]. The electric fields on the output side of the coupler are related to $E_+(L_c)$ and $E_-(L_c)$ as:

$$E_{1c} = Q\left[E_+(L_c) + E_-(L_c)\right] \quad (A.7)$$

$$E_{2c} = \left[E_+(L_c) - E_-(L_c)\right] \quad (A.8)$$

The modes coming out of the coupler continue travelling along the waveguide. When they reach the output end of the device, they become:

$$E_1 = E_{1c}\sqrt{A_{out}} \quad (A.9)$$

$$E_2 = E_{2c}\sqrt{A_{out}} \quad (A.10)$$

Substituting (A.1)to (A.8) into (A.9) and (A.10), and calculating the output powers as $P_1 = |E_1|^2$ and $P_2 = |E_2|^2$, yields the expressions in (3.1) and (3.2).

Acknowledgment

The authors acknowledge Yansong Cui for assistance with the theoretical analysis, and are grateful to Ewa Lisicka-Skrzek and Hamoudi Asiri for sample preparation and fabrication, respectively.

References

[1] , A. D. Boardman, Ed., *Electromagnetic Surface Modes*. Hoboken, NJ, USA: Wiley, 1982.

[2] , V. M. Agranovich and D. L. Mills, Eds., *Surface Polaritons: Electromagnetic Waves at Surfaces and Interfaces*. Amsterdam, The Netherlands: North Holland, 1982.

[3] H. Raether, *Surface Plasmons on Smooth and Rough Surfaces and on Gratings*. New York, NY, USA: Springer, 1988.

[4] P. Berini, "Long-range surface plasmon polaritons," *Adv. Opt. Photon.*, vol. 1, no. 3, pp. 484–588, 2009.

[5] P. Berini, "Plasmon-polariton waves guided by thin lossy metal films of finite width: Bound modes of symmetric structures," *Phys. Rev. B*, vol. 61, no. 15, pp. 10484–10503, 2000.

[6] R. Charbonneau, C. Scales, I. Breukelaar, S. Fafard, N. Lahoud, G. Mattiussi, and P. Berini, "Passive integrated optics elements based on long-range surface plasmon polaritons," *J. Lightw. Technol.*, vol. 24, no. 1, pp. 477–494, Jan. 2006.

[7] H. Fan, R. Buckley, and P. Berini, "Passive long-range surface plasmon-polariton devices in Cytop," *Appl. Opt.*, vol. 51, no. 10, pp. 1459–1467, Apr. 1, 2012.

[8] A. Boltasseva, T. Nikolajsen, K. Leosson, K. Kjaer, M. S. Larsen, and S. I. Bozhevolnyi, "Integrated optical components utilizing long-range surface plasmon polaritons," *J. Lightw. Technol.*, vol. 23, no. 1, pp. 413–422, Jan. 2005.

[9] E. D. Palik and G. Ghosh, *Electronic Handbook of Optical Constants of Solids*. New York, NY, USA: Academic, 1999.

[10] K. Leosson, T. Nikolajsen, A. Boltasseva, and S. I. Bozhevolnyi, "Long-grange surface plasmon polariton nanowire waveguides for device applications," *Opt. Exp.*, vol. 14, no. 1, pp. 314–319, 2006.

[11] S. Park and S. H. Song, "Polymeric variable optical attenuator based on long range surface plasmon polaritons," *Electron. Lett.*, vol. 42, no. 7, pp. 402–404, Mar. 30, 2006.

[12] H. Fan and P. Berini, "Thermo-optic characterisation of long-range surface plasmon devices in Cytop," *Appl. Opt.*, submitted for publication.

[13] G. Gagnon, N. Lahoud, G. A. Mattiussi, and P. Berini, "Thermally activated variable attenuation of long-range surface plasmon-polariton waves," *J. Lightw. Technol.*, vol. 24, no. 11, pp. 4391–4402, Nov. 2006.

[14] I. Breukelaar, R. Charbonneau, and P. Berini, "Long-range surface plasmon-polariton mode cutoff and radiation in embedded strip waveguides," *J. Appl. Phys.*, vol. 100, no. 4, p. 043104, 2006.

[15] T. Nikolajsen, K. Leosson, and S. I. Bozhevolnyi, "Surface plasmon polariton based modulators and switches operating at telecom wavelengths," *Appl. Phys. Lett.*, vol. 85, no. 24, pp. 5833–5835, Dec. 13, 2004.

[16] R. G. Heideman and P. V. Lambeck, "Remote opto-chemical sensing with extreme sensitivity: Design, fabrication and performance of a pigtailed integrated optical phase-modulated Mach–Zehnder interferometer system," *Sensors and Actuators B*, vol. 61, no. 1, pp. 100–127, 1999.

[17] L. Fabiny, S. T. Vohra, F. Bucholtz, and A. Dandridge, "Three-channel low-frequency fiber-optic voltage sensor," *Opt. Lett.*, vol. 19, no. 3, pp. 228–230, Feb. 1, 1994.

[18] B. Drapp, J. Piehler, A. Brecht, G. Gauglitz, B. J. Luff, J. S. Wilkinson, and J. Ingenhoff, "Integrated optical Mach-Zehnder interferometers as simazine immunoprobes," *Sensors and Actuators B*, vol. 38–39, no. 1, pp. 277–282, 1997.

[19] B. J. Luff, J. S. Wilkinson, J. Piehler, U. Hollenbach, J. Ingenhoff, and N. Fabricius, "Integrated optical Mach-Zehnder biosensor," *J. Lightw. Technol.*, vol. 16, no. 4, pp. 583–592, Apr. 1998.

[20] A. B. Buckman, *Guided-Wave Photonics*. Orlando, FL, USA: Harcourt Brace Jovanovich, 1992.

[21] S. K. Sheem, "Optical fiber interferometers with [3 × 3] directional couplers: Analysis," *J. Appl. Phys.*, vol. 52, no. 6, p. 3865, 1981.

[22] K. P. Koo, A. B. Tveten, and A. Dandridge, "Passive stabilization scheme for fiber interferometers using (3 × 3) fiber directional couplers," *Appl. Phys. Lett.*, vol. 41, no. 7, p. 616, 1982.

[23] D. A. Jackson, A. Dandridge, and S. K. Sheem, "Measurement of small phase shifts using a single-mode optical-fiber interferometer," *Opt. Lett.*, vol. 5, no. 4, pp. 139–141, Apr. 1980.

[24] P. Hua, B. Jonathan Luff, G. R. Quigley, J. S. Wilkinson, and K. Kawaguchi, "Integrated optical dual Mach-Zehnder interferometer sensor," *Sensors and Actuators B*, vol. 87, no. 2, pp. 250–257, 2002.

[25] S. Y. Wu, H. P. Ho, W. C. Law, and C. Lin, "Highly sensitive differential phase-sensitive surface plasmon resonance biosensor based on the Mach-Zehnder configuration," *Opt. Lett.*, vol. 29, no. 20, pp. 2378–2380, Oct. 15, 2004.

[26] J. Ptasinski, L. Pang, P.-C. Sun, B. Slutsky, and Y. Fainman, "Differential detection for nanoplasmonic resonance sensors," *IEEE Sensors J.*, vol. 12, no. 2, pp. 384–388, Feb. 2012.

[27] C. Chiu, E. Lisicka-Shrzek, R. Niall Tait, and P. Berini, "Fabrication of surface plasmon waveguides and devices in Cytop with integrated microfluidic channels," *J. Vac. Sci. Technol. B*, vol. 28, no. 4, pp. 729–735, Jul/Aug. 2010.

[28] Asahi Glass Co., Ltd., Japan, "Amorphous fluoropolymer CYTOP," Jan. 2009 [Online]. Available: www.agc-cytop.com

[29] O. Krupin, H. Asiri, C. Wang, R. N. Tait, and P. Berini, "Biosensing using straight long-range surface plasmon waveguides," *Opt. Exp.*, submitted for publication.

[30] H. Asiri, "Fabrication of surface plasmon biosensors in CYTOP," Master's thesis, Dept. Chem. Biolog. Eng., Univ. Ottawa, Ottawa, Canada, 2012.

[31] S. Takenobu, Y. Kuwana, K. Takayama, Y. Sakane, M. Ono, H. Sato, N. Keil, W. Brinker, H. Yao, C. Zawadzki, Y. Morizawa, and N. Grote, "All-polymer 8 × 8 AWG wavelength router using ultra low loss polymer optical waveguide material (CYTOP)," in *Proc. OFC/NFOEC*, 2008, Paper no. JWA 32.

Author biographies not included at authors' request due to space constraints.

Chapter 4

Thermo-optic sensing using LRSPP triple-output MZIs

4.1 Summary

In this chapter, a triple-output Mach-Zehnder interferometer (MZI) operating with long-range surface plasmon-polariton waves, consisting of a MZI in cascade with a triple coupler, is demonstrated at a wavelength of ~1370 nm, using the thermo-optic effect to produce phase shifting. A theoretical model for three-waveguide coupling is also proposed and was applied to compute the transfer characteristic of various designs. Dimensions for the device were selected to optimize performance, experiments were performed, and the results were compared to theory. The outputs were sinusoidally related to the thermally-induced phase shift and separated by ~$2\pi/3$ rad, as expected theoretically. Four detection schemes that take advantage of the 3 times larger dynamic range and suppress time-varying common perturbations are proposed and analyzed in order to improve the detection limit of the device. A minimum detectable phase shift ~2/3 that of an individual output was obtained from a power difference scheme and a normalization scheme. The smallest minimum detectable phase shift was 7.3 mrad.

4.2 Contribution

The results provided in this chapter were published as an article in *Optics Express*. I designed and built the experimental setup; I developed the theoretical model and implemented the numerical methods used for the theoretical analysis; I generated and

interpreted the theoretical and experimental results, and wrote the manuscript. Prof. Berini contributed to the design of the experiments and experimental setup, the development of the theoretical model, the interpretation of the results, and revised the manuscript. Hamoudi Asiri fabricated the devices used in the experiments.

4.3 Article

The published article follows verbatim.

Long-range surface plasmon triple-output Mach-Zehnder interferometers

Hui Fan,[1] Robert Charbonneau,[1] and Pierre Berini[1,2,*]

[1]*School of Electrical Engineering and Computer Science, University of Ottawa, 800 King Edward Ave., Ottawa, Ontario K1N 6N5, Canada*

[2]*Department of Physics, University of Ottawa, 150 Louis-Pasteur St., Ottawa, Ontario K1N 6N5, Canada*

[redacted]

Abstract: A triple-output Mach-Zehnder interferometer (MZI) operating with long-range surface plasmon-polariton waves, consisting of a MZI in cascade with a triple coupler, is demonstrated at a wavelength of ~1370 nm, using the thermo-optic effect to produce phase shifting. A theoretical model for three-waveguide coupling is also proposed and was applied to compute the transfer characteristic of various designs. Dimensions for the device were selected to optimize performance, experiments were performed, and the results were compared to theory. The outputs were sinusoidally related to the thermally-induced phase shift and separated by ~$2\pi/3$ rad, as expected theoretically. Four detection schemes that take advantage of the 3 times larger dynamic range and suppress time-varying common perturbations are proposed and analyzed in order to improve the detection limit of the device. A minimum detectable phase shift ~2/3 that of a single output was obtained from a power difference scheme and a normalization scheme. The smallest minimum detectable phase shift was 7.3 mrad. The device is promising for sensing applications, including (bio)chemical sensing.

©2014 Optical Society of America

OCIS codes: (240.6680) Surface plasmons; (230.3120) Integrated optics devices.

References and links

1. A. D. Boardman, ed., *Electromagnetic Surface Modes* (John Wiley, 1982).
2. H. Raether, *Surface Plasmons on Smooth and Rough Surfaces and on Gratings* (Springer, 1988).
3. P. Berini, "Long-range surface plasmon polaritons," Adv. Opt. Photon. **1**(3), 484–588 (2009).
4. R. Charbonneau, C. Scales, I. Breukelaar, S. Fafard, N. Lahoud, G. Mattiussi, and P. Berini, "Passive integrated optics elements based on long-range surface plasmon-polaritons," J. Lightwave Technol. **24**(1), 477–494 (2006).
5. P. Berini, "Plasmon-polariton waves guided by thin lossy metal films of finite width: Bound modes of symmetric structures," Phys. Rev. B **61**(15), 10484–10503 (2000).
6. K. Leosson, T. Nikolajsen, A. Boltasseva, and S. I. Bozhevolnyi, "Long-range surface plasmon polariton nanowire waveguides for device applications," Opt. Express **14**(1), 314–319 (2006).
7. G. Gagnon, N. Lahoud, G. A. Mattiussi, and P. Berini, "Thermally activated variable attenuation of long-range surface plasmon-polariton waves," J. Lightwave Technol. **24**(11), 4391–4402 (2006).
8. I. Breukelaar, R. Charbonneau, and P. Berini, "Long-range surface plasmon-polariton mode cutoff and radiation in embedded strip waveguides," J. Appl. Phys. **100**(4), 043104 (2006).
9. H. Fan and P. Berini, "Thermo-optic characterization of long-range surface-plasmon devices in Cytop," Appl. Opt. **52**(2), 162–170 (2013).
10. T. Nikolajsen, K. Leosson, and S. I. Bozhevolnyi, "Surface plasmon-polariton based modulators and switches operating at telecom wavelengths," Appl. Phys. Lett. **85**(24), 5833–5835 (2004).
11. J. Gosciniak, S. I. Bozhevolnyi, T. B. Andersen, V. S. Volkov, J. Kjelstrup-Hansen, L. Markey, and A. Dereux, "Thermo-optic control of dielectric-loaded plasmonic waveguide components," Opt. Express **18**(2), 1207–1216 (2010).
12. S. Kaya, J.-C. Weeber, F. Zacharatos, K. Hassan, T. Bernardin, B. Cluzel, J. Fatome, and C. Finot, "Photo-thermal modulation of surface plasmon polariton propagation at telecommunication wavelengths," Opt. Express **21**(19), 22269–22284 (2013).
13. S. Y. Wu, H. P. Ho, W. C. Law, C. Lin, and S. K. Kong, "Highly sensitive differential phase-sensitive surface plasmon resonance biosensor based on the Mach-Zehnder configuration," Opt. Lett. **29**(20), 2378–2380 (2004).

#201434 - $15.00 USD Received 15 Nov 2013; revised 3 Feb 2014; accepted 3 Feb 2014; published 13 Feb 2014
(C) 2014 OSA

14. J. Ptasinski, L. Pang, P. C. Sun, B. Slutsky, and Y. Fainman, "Differential detection for nanoplasmonic resonance sensors," IEEE Sens. J. **12**(2), 384–388 (2012).
15. R. G. Heideman and P. V. Lambeck, "Remote opto-chemical sensing with extreme sensitivity: Design, fabrication and performance of a pigtailed integrated optical phase-modulated Mach–Zehnder interferometer system," Sens. Actuators B Chem. **61**(1), 100–127 (1999).
16. A. Khan, O. Krupin, E. Lisicka-Skrzek, and P. Berini, "Mach-Zehnder refractometric sensor using long-range surface plasmon waveguides," Appl. Phys. Lett. **103**(11), 111108 (2013).
17. B. J. Luff, J. S. Wilkinson, J. Piehler, U. Hollenbach, J. Ingenhoff, and N. Fabricius, "Integrated optical Mach-Zehnder biosensor," J. Lightwave Technol. **16**(4), 583–592 (1998).
18. K. C. Vernon, D. E. Gómez, and T. J. Davis, "A compact interferometric sensor design using three waveguide coupling," J. Appl. Phys. **106**(10), 104306 (2009).
19. A. B. Buckman, *Guided-Wave Photonics* (Harcourt Brace Jovanovich, 1992).
20. S. K. Sheem, "Optical fiber interferometers with [3x3] directional couplers: Analysis," J. Appl. Phys. **52**(6), 3865 (1981).
21. K. P. Koo, A. B. Tveten, and A. Dandridge, "Passive stabilization scheme for fiber interferometers using (3x3) fiber directional couplers," Appl. Phys. Lett. **41**(7), 616 (1982).
22. P. Hua, B. Jonathan Luff, G. R. Quigley, J. S. Wilkinson, and K. Kawaguchi, "Integrated optical dual Mach-Zehnder interferometer sensor," Sens. Actuators B Chem. **87**(2), 250–257 (2002).
23. H. Fan and P. Berini, "Noise cancellation in long-range surface plasmon dual-output Mach-Zehnder interferometers," J. Lightwave Technol. **31**(15), 2606–2612 (2013).
24. A. Yariv, *Optical Electronics* (Saunders, 1991).
25. S. L. Chuang, "Application of the strongly coupled-mode theory to integrated optical devices," IEEE J. Quantum Electron. **23**(5), 499–509 (1987).
26. S. L. Chuang, "A coupled-mode theory for multiwaveguide systems satisfying the reciprocity theorem and power conservation," J. Lightwave Technol. **5**(1), 174–183 (1987).
27. H. Fan, R. Buckley, and P. Berini, "Passive long-range surface plasmon-polariton devices in Cytop," Appl. Opt. **51**(10), 1459–1467 (2012).
28. P. Berini, R. Charbonneau, N. Lahoud, and G. Mattiussi, "Characterization of long-range surface plasmon-polariton waveguides," J. Appl. Phys. **98**(4), 043109 (2005).
29. Asahi Glass Co, Ltd., Japan, "Amorphous fluoropolymer CYTOP," Jan. 2009 [Online]. Available: *http://www.agc-cytop.com*.
30. E. D. Palik and G. Ghosh, *Electronic Handbook of Optical Constants of Solids* (Academic, 1999).
31. H. Asiri, "Fabrication of surface plasmon biosensors in CYTOP," Master's thesis, Dep. Chem. Biol. Eng., Univ. Ottawa, Ottawa, Canada, 2012.
32. C. Chiu, E. Lisicka-Shrzek, R. N. Tait, and P. Berini, "Fabrication of surface plasmon waveguides and devices in Cytop with integrated microfluidic channels," J. Vac. Sci. Technol. B **28**(4), 729–735 (2010).

1. Introduction

Surface plasmon-polaritons (SPPs) are transverse magnetic (TM) polarised optical surface waves that propagate typically along the interface of a metal and a dielectric [1,2]. Long-range surface plasmon-polaritons (LRSPPs) are SPP supermodes having significantly lower attenuation supported by a thin metal slab or stripe waveguide [3], formed as single-interface SPPs at each metal-dielectric interface couple with each other. Amongst the LRSPPs supported by the stripe, the fundamental mode exhibits a Gaussian-like field distribution [4] and thus is amenable to end-fire excitation, while the others are high-order modes exhibiting field extrema along the width of the stripe and can be cut-off by choosing appropriate stripe dimensions [5].

One application of LRSPPs is thermo-optic modulation, of which the basic mechanism is that the refractive index of a material changes with temperature. A simple model for the thermo-optic effect is the linear model given as follows:

$$n(T) = n(T_0) + (T - T_0)\frac{dn}{dT} \tag{1.1}$$

where n is the refractive index, T is the temperature, and dn/dT is the thermo-optic coefficient (TOC) - the ratio of the change of the refractive index of a material over that of the temperature. The linear model for the thermo-optic effect is assumed to hold over a small temperature range for constant pressure and operating wavelength. Thermo-optic modulation devices that have been designed and investigated includes straight variable optical attenuators

#201434 - $15.00 USD Received 15 Nov 2013; revised 3 Feb 2014; accepted 3 Feb 2014; published 13 Feb 2014
(C) 2014 OSA

(VOAs) based on thermally-induced anti-guiding [6] and asymmetric mode cut-off [7,8], and Mach-Zehnder interferometers (MZIs) based on thermally-induced phase shift between the sensing and the reference arms [9,10]. Except for LRSPP, there are also researches on thermo-optic modulation using dielectric-loaded SPP (DLSPP) waveguides [11,12].

MZIs are widely used for thermo-optic modulation [13,14] and other applications, e.g., electro-optic modulation [15], and biochemical sensing [16–18]. Multi-output MZIs consist of a MZI in cascade with a dual or triple coupler. Dual-output MZIs provide two complementary outputs [19] that can be used to suppress time-varying common perturbation and to obtain twice the dynamic range compared to a single-output MZI, whereas triple-output MZIs have three outputs with ~$2\pi/3$ rad phase separation [17], so at least one output is always available in the linear region (where the sensitivity is maximum). In the past, multi-output MZIs based on fibers [20,21], dielectric waveguides [22], and surface plasmon waveguides [23] were demonstrated. Theoretical research has also been conducted to apply weakly coupled theory [18,24] and strongly coupled theory [25,26] to multiple-output MZIs.

In this paper, we demonstrate thermo-optically activated triple-output MZIs based on LRSPPs, we propose a general theoretical approach based on modal analysis to model and design triple-output MZIs, and we give simple equations that model the operation of an idealised design from which perturbation cancellation and dynamic range can be easily assessed. We compare our theoretical transfer characteristics with those obtained from coupled-mode theory and with the measurements. We also investigate the suppression of common mode perturbations in the transfer characteristics and in outputs over time. In principle, thermo-optic activation can be replaced with bio-chemical interactions, so the device is relevant to biosensing.

The paper is organized as follows: Section 2 introduces the structure of interest and the general theoretical model applied, and validates the results of the model via comparison with coupled-mode theory; the design of triple-output MZIs based on LRSPPs is also discussed. Section 3 compares the measured transfer characteristics with theory, and gives a brief description of the experimental devices and setup. Section 4 investigates the dynamic range, the ability to suppress time-varying common perturbations, and the recurring availability of an output in the linear region. Section 5 concludes the paper.

2. Theoretical

2.1 Structure

Figure 1 shows a sketch of the structure of interest in this paper. The triple-output MZI consists of a symmetric MZI in cascade with a triple coupler.

Our fabricated structure is comprised of waveguides consisting of Au stripes cladded with Cytop, all stripes designed to be 35 nm thick and 5 μm wide, and operating in a single LRSPP mode (ss_b^0 [5]) at the operating free-space wavelength of interest (λ_0~1310 nm). The MZI has a Y-junction splitter with a 1 μm inner waveguide separation at the split and a separation of 140 μm between its two arms at the widest point. All curved sections have the same radius of curvature of 5.5 mm. The dimensions for these elements were selected based on the modelling and design results summarised in [4,27]. The triple coupler, shown in expanded view in Fig. 1(b), has a coupling length of 828.57 μm, a separation of 2 μm between the waveguides, and a flared-out separation of 46 μm between its three outputs at the end of the structure. This coupler was modelled and designed as described in the subsequent sub-sections. The linear length of the full structure (MZI and coupler) is 4.8 mm; the optical path length is slightly longer.

Additional features for thermo-optic control includes 2 μm long gaps as well as 40 μm x 40 μm metal pads that are placed 20 μm away from the waveguides and connected to them with contact arms of the same width and thickness as the waveguides. The dimensions are chosen such that the features remain optically non-invasive. The pads are used to attach metal

#201434 - $15.00 USD Received 15 Nov 2013; revised 3 Feb 2014; accepted 3 Feb 2014; published 13 Feb 2014
(C) 2014 OSA

probes to inject electrical current generating heat in the active region of the device, and the gaps isolate the current to that region. As the active region is heated, the refractive index of the surrounding Cytop claddings change, introducing a phase shift between the LRSPP modes travelling in the two arms of the MZI, and so the optical powers of the three outputs of the coupler change as well. The designed operating wavelength of the device is 1310 nm (free-space).

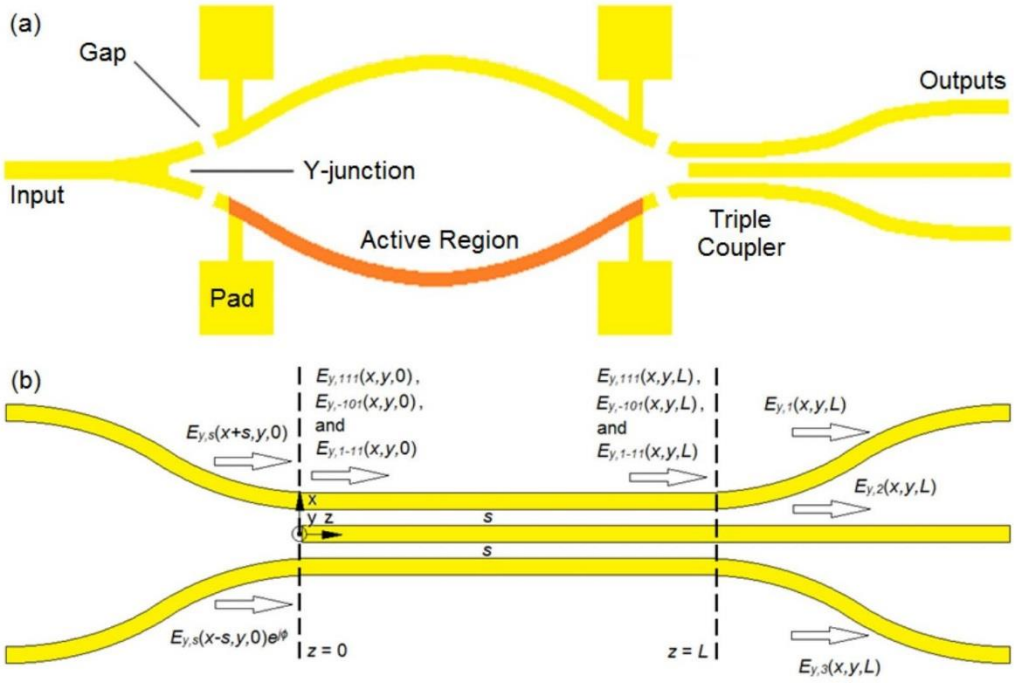

Fig. 1. Sketch of the structure of interest: (a) triple-output MZI, and (b) triple coupler structure with notation identifying the modes travelling thereon.

2.2 Coupling model

We model the performance of the triple coupler using modal analysis and overlap integrals, following [4,8], as illustrated in Fig. 1(b), despite the existing strongly coupled theory discussed in [17,25], because the modal approach is direct, straight forward, and only requires an accurate mode solver. The inputs to the triple coupler are connected to the MZI, as shown in Fig. 1(b), and excited by the fundamental LRSPP mode emerging from the arms of the MZI. Thus, at the inputs of the triple coupler ($z = 0$), the input field distribution is taken as the fundamental LRSPP mode supported by a single waveguide (ss_b^0) centered on one of the outside waveguides of the coupler, superimposing the same mode field distribution centered on the other outside waveguide of the coupler multiplied by a factor $e^{j\phi}$ representing the thermally induced phase shift, as expressed as follows:

$$E_{y,in}(x,y,0) = E_{y,s}(x+s,y,0) + E_{y,s}(x-s,y,0)e^{j\phi} \qquad (2.1)$$

here s is the coupler separation and $E_{y,s}$ is the mode field of the ss_b^0 mode supported by a single waveguide, as shown in Fig. 2(a). As the input field enters the triple coupler, it redistributes among the three supermodes supported by the coupler, namely mode (1 1 1), mode (−1 0 1), and mode (1 −1 1), for which the field distributions are shown in Figs. 2(b)–2(d), respectively, and forward propagating radiative modes. The latter are neglected (but could be included by discretizing the continuum of radiative modes into a finite set of box

#201434 - $15.00 USD Received 15 Nov 2013; revised 3 Feb 2014; accepted 3 Feb 2014; published 13 Feb 2014
(C) 2014 OSA

modes, following [8]). The input overlap factors C_i into each supermode at the input of the coupler are given as follows [8,28]:

$$C_i = \frac{\iint_{A_\infty} E_{y,in}(x,y,0)\cdot E^*_{y,i}(x,y,0)\,dA}{\sqrt{\left(\iint_{A_\infty} E_{y,in}(x,y,0)\cdot E^*_{y,in}(x,y,0)\,dA\right)\left(\iint_{A_\infty} E_{y,i}(x,y,0)\cdot E^*_{y,i}(x,y,0)\,dA\right)}} \quad (2.2)$$

here A_∞ is the area of the entire computational domain at the transverse plane where the modes meet, and $E_{y,i}$ is the field of one of the three super modes supported by the coupler (with i = (1 1 1), (−1 0 1), or (1 −1 1)). It was checked that $\sum_i |C_i|^2 \approx 1$, showing that most of the forward propagating power is coupled into the supermodes of the coupler and justifying the neglect of the forward propagating radiative modes. After travelling along the coupler and reaching its end ($z = L$), the super modes superimpose to yield the output field distribution as:

$$E_{y,out}(x,y,L) = \sum_i C_i E_{y,i}(x,y,0)\, e^{-(\alpha_i + j\beta_i)L} \quad (2.3)$$

here the factor $e^{-(\alpha_i + j\beta_i)L}$ represents the attenuation and propagation along the coupler and L is the coupler length. The α_i and β_i of each supermode must be used as they are different. The output field redistributes again among the single modes centered on the individual waveguides connected to the output of the coupler, and the output overlap factors C_m are calculated similarly as in Eq.(2.2):

$$C_1 = \frac{\iint_{A_\infty} E_{y,out}(x,y,L)\cdot E^*_{y,s}(x+s,y,L)\,dA}{\sqrt{\left(\iint_{A_\infty} E_{y,out}(x,y,L)\cdot E^*_{y,out}(x,y,L)\,dA\right)\left(\iint_{A_\infty} E_{y,s}(x+s,y,L)\cdot E^*_{y,s}(x+s,y,L)\,dA\right)}} \quad (2.4.a)$$

$$C_2 = \frac{\iint_{A_\infty} E_{y,out}(x,y,L)\cdot E^*_{y,s}(x,y,L)\,dA}{\sqrt{\left(\iint_{A_\infty} E_{y,out}(x,y,L)\cdot E^*_{y,out}(x,y,L)\,dA\right)\left(\iint_{A_\infty} E_{y,s}(x,y,L)\cdot E^*_{y,s}(x,y,L)\,dA\right)}} \quad (2.4.b)$$

$$C_3 = \frac{\iint_{A_\infty} E_{y,out}(x,y,L)\cdot E^*_{y,s}(x-s,y,L)\,dA}{\sqrt{\left(\iint_{A_\infty} E_{y,out}(x,y,L)\cdot E^*_{y,out}(x,y,L)\,dA\right)\left(\iint_{A_\infty} E_{y,s}(x-s,y,L)\cdot E^*_{y,s}(x-s,y,L)\,dA\right)}} \quad (2.4.c)$$

here C_2 relates to the middle waveguide while C_1 and C_3 to the outside two. The normalized optical powers in the individual output waveguides are then calculated as $P_m = |C_m|^2$ with m = 1, 2, or 3. We neglect the effects of the s-bends before and after the coupler on the mode field distribution of a single waveguide $E_{y,s}$ as the radii of curvature are large [27].

#201434 - $15.00 USD Received 15 Nov 2013; revised 3 Feb 2014; accepted 3 Feb 2014; published 13 Feb 2014
(C) 2014 OSA

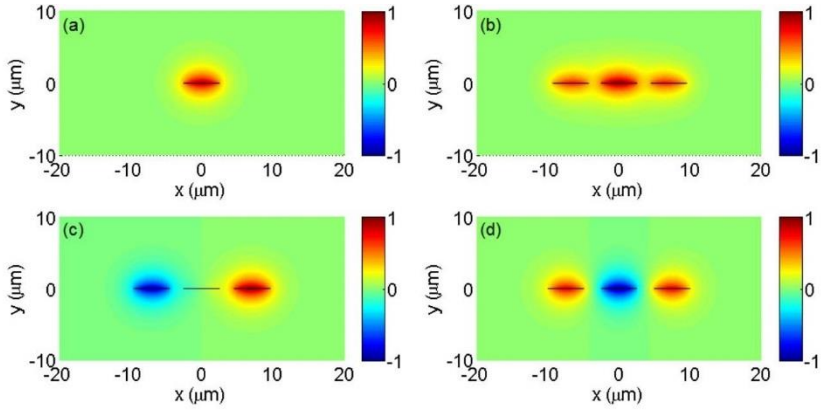

Fig. 2. Calculated normalized E_y field distribution of (a) the long-range ss_b^0 mode supported by a single waveguide, (b) the long-range supermode (1 1 1), (c) the long-range supermode (−1 0 1), and (d) the long-range supermode (1 −1 1), supported by a triple coupler.

2.3 Validation

To validate the theoretical model, Fig. 4(a) of Ref [17] was reproduced and the calculated results were compared to the original ones obtained by applying the strongly coupled theory. The structure considered consisted of a slab dielectric waveguide symmetric triple coupler having a coupler separation s = 1 μm and coupler length $L = 0.75L_c$. L_c is defined as the coupling length where maximum power is transferred from a single input at one outside waveguide to the other outside waveguide. The dielectric coupler has claddings of refractive index of 1.6 and cores of refractive index 1.646, operating at a free-space wavelength of 786 nm, and the core width was 1 μm. The modeling work was conducted using the Finite Element Method (FEM) and COMSOL. As shown in Fig. 3, the results coincide very well, providing verification of our theoretical model.

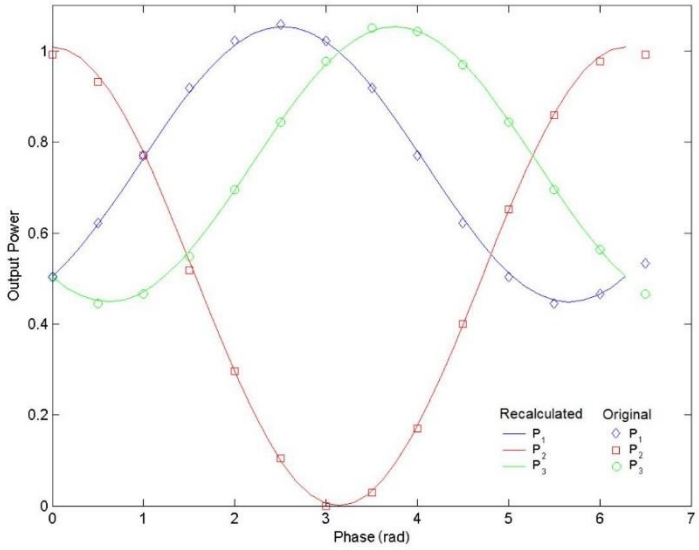

Fig. 3. Calculated output powers compared to results of [17] for a dielectric slab triple coupler of core index 1.646 and cladding index 1.6, operating at 786 nm. The core width was 1 μm, the coupler separation was s = 1 μm and coupler length $L = 0.75L_c$.

#201434 - $15.00 USD Received 15 Nov 2013; revised 3 Feb 2014; accepted 3 Feb 2014; published 13 Feb 2014
(C) 2014 OSA

2.4 Design

The model was implemented to the structure of interest in this paper, at the operation wavelength λ_0 = 1310 nm, for which the refractive index of Cytop is n = 1.3348 [29] and the relative permittivity of Au is ε_r = –86.08 - j8.322 [30] ($e^{+j\omega t}$ time harmonic form implied). The β/β_0 and the mode power attenuation (MPA) of the three supermodes of interest in the triple coupler (Figs. 2(b)–2(d)) were computed for various stripe separations and plotted in Figs. 4(a) and 4(b), respectively. It is observed that as the separation increases, both the β/β_0 and the MPA of the three supermodes merge to those of the ss_b^0 mode, becoming approximately equal at s ~16 μm. Herein β/β_0 is the real part of the effective index and is denoted n_{eff}, and the MPA is related to the attenuation constant α in m^{-1}, as:

$$\mathrm{MPA} = \alpha \frac{20}{1000} \log_{10} e \tag{2.5}$$

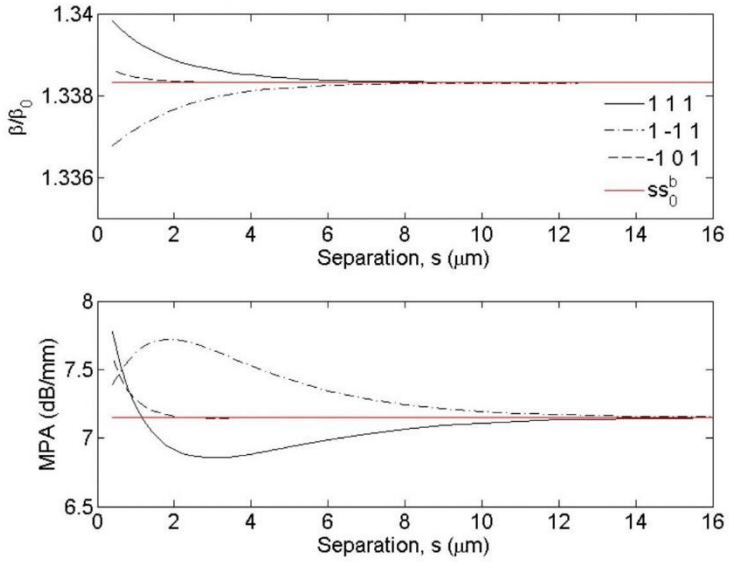

Fig. 4. Calculated β/β_0 and MPA versus stripe separation s for the triple coupler.

From these calculations, the transfer characteristic of the triple-output MZI was computed and its dimensions optimized. Figures 5(a), 5(b), and 5(c) plot the normalized optical power of the three outputs as a function of the phase shift applied between the two arms of the MZI (ϕ) for coupler separations s = 1, 2 and 3μm, respectively. All three normalized powers are sinusoidal with the phase shift. The corresponding coupler lengths L were chosen as 457 μm, 828.57 μm and 1530 μm in order that the individual sinusoidal responses separate to ~2π/3 rad from each other. The wider the separation the longer the required coupler length. The total output power is also plotted and is observed to be approximately constant with ϕ in all cases, justifying our neglect of the forward propagating radiative modes. Comparing Figs. 5(a), 5(b) and 5(c), the total output power becomes increasingly constant as the separation increases, but at the expense of a decrease in the dynamic range, so there is a trade-off between these two quantities. Another consideration is that a shorter device is more compact and profits integration. The devices used in the experiments are designed to have a coupler separation of s = 2 μm and coupler length L = 828.57 μm, providing a flatter total output power response, with good dynamic range, and an adequate device length.

#201434 - $15.00 USD Received 15 Nov 2013; revised 3 Feb 2014; accepted 3 Feb 2014; published 13 Feb 2014
(C) 2014 OSA

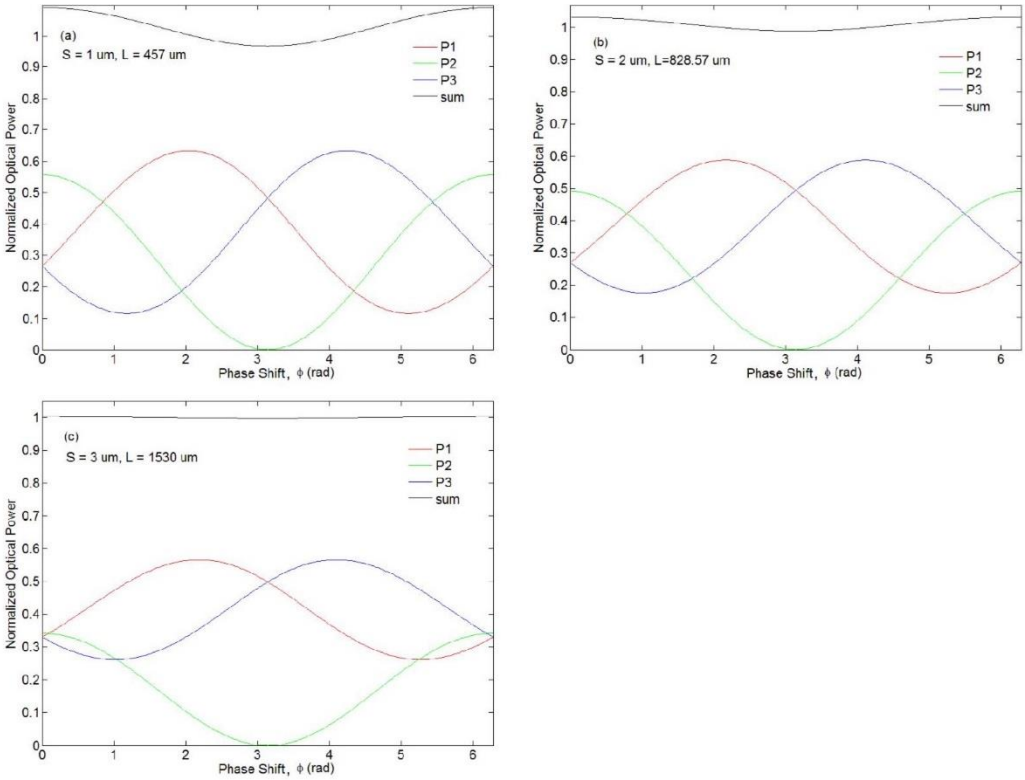

Fig. 5. Calculated normalized optical power output versus phase shift ϕ for triple-output MZIs for triple couplers designed with (a) s = 1 μm, L = 457 μm, (b) s = 2 μm, L = 828.57 μm, and (c) s = 3 μm, L = 1530 μm.

3. Experimental

3.1 Device and setup

Figure 6(a) shows a microscope image of the triple-output MZI device used in the experiments and Fig. 6(b) shows a higher magnification image of the triple coupler portion of the device. The devices were fabricated on a 450 μm thick silicon substrate by sequentially depositing a 10 μm thick Cytop layer as the bottom cladding, a 35 nm thick Au layer patterned using lift-off lithography, and another 10 μm thick Cytop layer as the top cladding that maintains the optical symmetry of the device [31,32]. All devices originate from the same wafer (identified internally as ND II). Due to fabrication most of the waveguides suffer some extent of deformation and the operation wavelength of the devices changes from the designed wavelength of 1310 nm to ~1370 nm (according to the experimental results). Other possible defects may include slightly thicker and wider waveguides, unbalanced Y-junction splitters and MZI arms [27], a wider coupler separation, and a slightly decentralized triple coupler.

#201434 - $15.00 USD Received 15 Nov 2013; revised 3 Feb 2014; accepted 3 Feb 2014; published 13 Feb 2014
(C) 2014 OSA

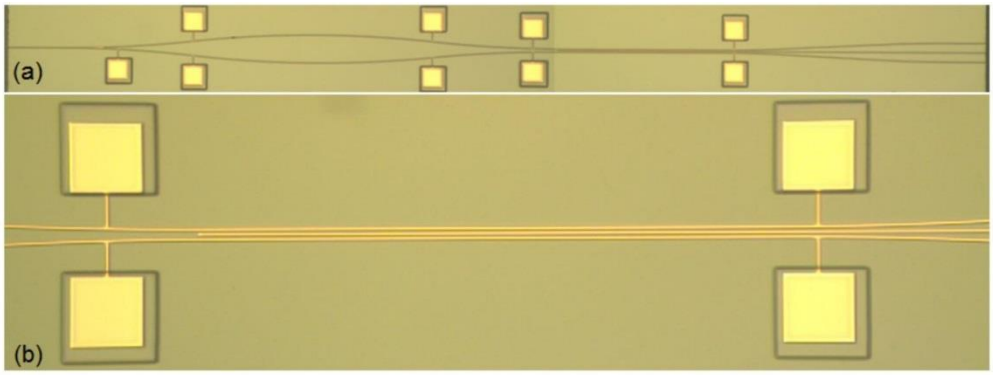

Fig. 6. Microscope images of (a) the whole triple-output MZI device and (b) the triple coupler portion of the device under higher magnification.

Figure 7 illustrates the block diagram of the experimental setup. Light from a tunable laser is butt-coupled into the triple-output MZI device through a polarisation maintaining fiber (PMF) and the three outputs are collimated by a microscope objective and captured by a CCD camera simultaneously, constituting the optical path. Electrical current from a power supply is injected into the active region of one arm of the MZI through metal probes, heating the waveguide to apply the thermo-optic phase modulation, and measured by a multi-meter, forming the electrical circuit. The power supply, the multi-meter, and the camera are controlled by LabVIEW programs to change the applied voltages, to read the currents, and to take pictures of output mode images every time step (0.5 s), respectively. The mode images are captured in real time using frame grabber software (LBA-710PC, Ophir Spiricon), and post-processed using Matlab to determine the power (in arbitrary units) within three pre-set software apertures that cover the three outputs of the coupler. The power is computed by numerical integration of the pixel values within each aperture (as a diamond sum) and is related to the absolute power via a constant that can be determined via calibration. In this method the powers of all three outputs are captured simultaneously so that the suppression of time-varying common perturbations can be carried out.

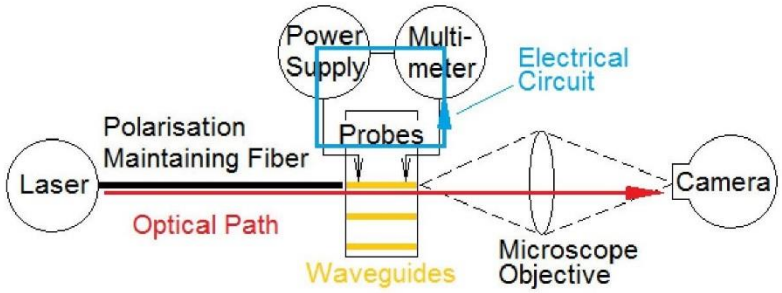

Fig. 7. Block diagram of the thermo-optic experimental setup.

3.2 Results

With the above-mentioned device and setup, experiments were conducted by increasing the applied voltage in a step of 0.01 V every 0.5 s. The dissipated electrical powers corresponding to the voltages were calculated. The operating wavelength of the laser was tuned to 1364 nm, selected to optimize the performance of the devices. The output optical power versus dissipated electrical power of the individual outputs and the sum of the optical powers are plotted in Fig. 8(a), revealing the transfer characteristic of the device. The measured optical powers are given in arbitrary units (A.U.). A mosaic showing the outputs for three dissipated

#201434 - $15.00 USD Received 15 Nov 2013; revised 3 Feb 2014; accepted 3 Feb 2014; published 13 Feb 2014
(C) 2014 OSA

electrical powers that clearly shows the power switching among the three outputs is given as the inset.

As observed from Fig. 8(a), the curves of the individual outputs are sinusoidal and with ~2π/3 rad phase separation, but the two curves of the outside outputs are not as symmetric as in the ideal case of Fig. 5. This could be caused by asymmetry in the coupling structure induced by fabrication imperfections. In order to compare the measurements with theory, computations were conducted where the middle stripe of the triple coupler was decentralized (but maintained parallel) causing asymmetry relative to the two outside stripes. By optimising the fit between theory and the measurements, the left and right coupler separations increased from the designed 2 μm, to 2.2 μm and 2.5 μm, respectively. Also, the waveguide thickness decreases from the designed 35 nm to 31 nm (which is consistent with the results in [27]). Both the measured and the simulated results are normalized by dividing each by the sum of the optical powers, to exclude possible errors caused by the drifting of the powers in the experiments and to make them comparable. The measured results are re-plotted as a function of thermally induced phase shift in the same way that the computed results are plotted. The conversion from dissipated electrical power to thermally induced phase shift is discussed in [9] and [23]. Figure 8(b) shows the comparison of the measured and computed results, from which the generally good fit shows that decentralizing the middle waveguide of the triple coupler is a reasonable explanation for the difference in dynamic range between the two outside output powers.

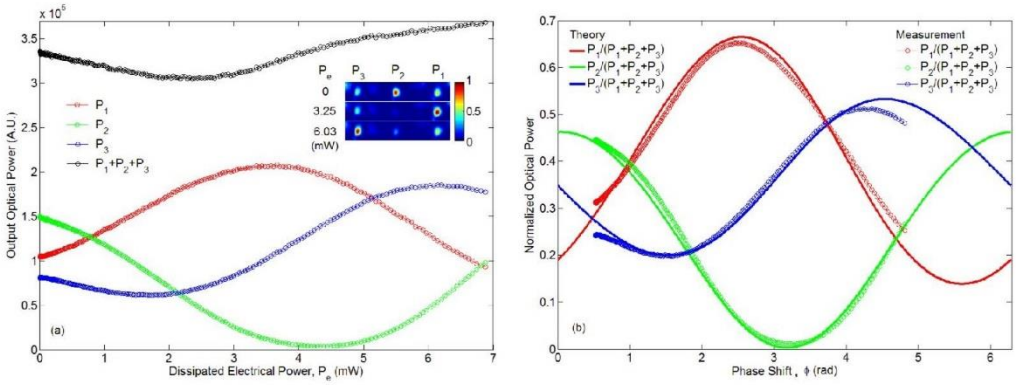

Fig. 8. Transfer characteristic measurements for a triple-output MZI: (a) output optical power versus dissipated electrical power, and (b) normalized optical power versus thermally induced phase shift. The theoretical results are superimposed on the measurements in Part (b). The inset is a mosaic of normalized mode images showing the power switching among the three outputs.

4. Discussion

4.1 Operation with maximum sensitivity

There are three main advantages for the triple-output MZI device compared to a single-output MZI. The first one is that an output near maximum sensitivity is always available. It is observed from Figs. 5 and 8 that as the three output curves are separated by ~2π/3 rad in phase, at any given point there is at least one output in the linear region of a sinusoidal curve, providing the fastest change in optical power in response to a phase shift, and thus maximum MZI sensitivity.

4.2 Dynamic range

Secondly, the triple-output MZI has another advantage: In the ideal case (*e.g.*, Fig. 5(c)), the three outputs can be combined appropriately to obtain a response having a dynamic range three times larger than that of a single output, without significantly increasing the time-varying perturbations. Ideally, the dynamic range of the three individual outputs are nearly

#201434 - $15.00 USD Received 15 Nov 2013; revised 3 Feb 2014; accepted 3 Feb 2014; published 13 Feb 2014
(C) 2014 OSA

equal, the phase separation between them is very close to ~2π/3, and the total power can be taken as constant. Thus the three sinusoidal outputs P_1, P_2 and P_3 can be modeled mathematically using the following equations in terms of the induced phase shift ϕ and the input optical power P_{in}, with time-varying common perturbation terms (p_i, p_o) included:

$$P_1 = \left[a\cos\left(\phi - \frac{2\pi}{3} \right) + b_1 \right] \left(P_{in} + p_i \right) + p_o \tag{4.1.a}$$

$$P_2 = \left(a\cos\phi + b_2 \right) \left(P_{in} + p_i \right) + p_o \tag{4.1.b}$$

$$P_3 = \left[a\cos\left(\phi + \frac{2\pi}{3} \right) + b_3 \right] \left(P_{in} + p_i \right) + p_o \tag{4.1.c}$$

here a is the amplitude and b_1, b_2 and b_3 are the constant offsets of the sinusoidal curves. p_i represents a perturbation on the input side, such as a drift in the input optical power or input coupling conditions, and p_o represents a perturbation received on the output side, for instance, due to background light. We define three power difference terms based on the individual powers: $D_i = 2P_i - P_j - P_k$, where i is one of 1, 2, 3 while j and k are the other two. In the case of D_2 for example, by multiplying Eq. (4.1.b) by 2 and subtracting Eqs. (4.1.a) and (4.1.b), the following expression is obtained:

$$D_2 = \left(3a\cos\phi + 2b_2 - b_1 - b_3 \right) \left(P_{in} + p_i \right) \tag{4.2}$$

Compared to P_2, the input common perturbation p_i of D_2 remains the same whereas the output common perturbation p_o is cancelled and the amplitude of the sinusoidal term triples. It is easy to calculate D_1 and D_3 and observe that they behave the same way as D_2. Thus the difference terms provide a signal with 3 times larger dynamic range compared to the individual ones without increasing the level of any time-varying perturbations. Figure 9 shows D_1, D_2 and D_3 obtained from the measurements of Fig. 8(a). It is observed that they have 3 times larger dynamic ranges, in agreement with Eq. (4.2).

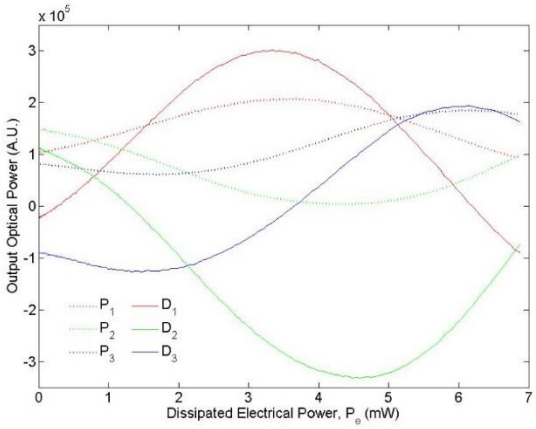

Fig. 9. Output optical power difference versus dissipated electrical power obtained from the measurements of Fig. 8(a).

4.3 Suppression of common perturbations

The third advantage is the ability to suppress common input perturbations. Suppose there is no output perturbation p_o, then the input perturbation p_i can be removed by normalization. Take the normalized P_2 for instance; it has the following expression as obtained from Eqs. (4.1.a)-(4.1.c):

#201434 - $15.00 USD Received 15 Nov 2013; revised 3 Feb 2014; accepted 3 Feb 2014; published 13 Feb 2014
(C) 2014 OSA

$$\frac{P_2}{P_1+P_2+P_3}=\frac{(a\cos\phi+b_2)(P_{in}+p_i)+p_o}{(b_1+b_2+b_3)(P_{in}+p_i)+3p_o} \tag{4.3}$$

with no output perturbation ($p_o = 0$) the above simplifies to:

$$\frac{P_2}{P_1+P_2+P_3}=\frac{a}{b_1+b_2+b_3}\cos\phi+\frac{b_2}{b_1+b_2+b_3} \tag{4.4}$$

As observed from Eq. (4.4) the input perturbation p_i is removed. If the output perturbation p_o exists, the term $P_{in} + p_i$ cannot be completely cancelled but normalization can at least suppress to some extent the time-varying perturbation.

The perturbation suppression obtained by normalization was observed in experiments. Figure 10(a) shows the unnormalized output optical powers and power differences versus dissipated electrical power. It is obvious that strong perturbations prevail in the curves. The amplitudes of the perturbations are proportional to the power of the signal and so the power differences cannot suppress them, therefore they are assumed to be input perturbations p_i. Figure 10(b) shows the same measurements but normalised, revealing significant suppression of the time-varying perturbations.

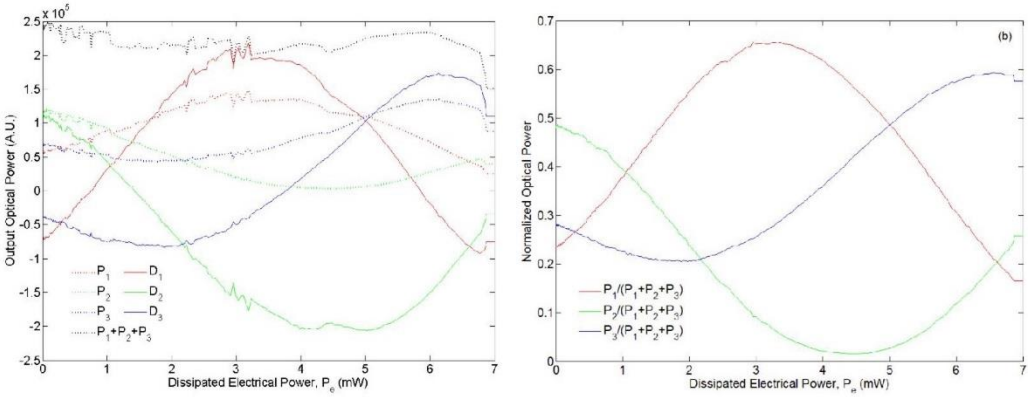

Fig. 10. Experiment illustrating time-varying perturbation suppression by normalization: (a) unnormalized output optical power and power difference and (b) normalized optical power versus dissipated electrical power.

Normalization can also be applied to the power difference terms. From Eqs. (4.1.a)-(4.1.c) the normalized D_2 is calculated as:

$$\frac{D_2}{P_1+P_2+P_3}=\frac{(3a\cos\phi+2b_2-b_1-b_3)(P_{in}+p_i)}{(b_1+b_2+b_3)(P_{in}+p_i)+3p_o} \tag{4.5}$$

This produces a similar effect as normalizing individual powers, as is easily observed setting $p_o = 0$ into the above, yielding:

$$\frac{D_2}{P_1+P_2+P_3}=\frac{3a}{b_1+b_2+b_3}\cos\phi+\frac{2b_2-b_1-b_3}{b_1+b_2+b_3} \tag{4.6}$$

Thus there are four possible detection schemes: an individual power (*i.e.* P_2), a power difference (*i.e.* D_2), a normalized individual power (*i.e.* $P_2/(P_1 + P_2 + P_3)$), and a normalized power difference (*i.e.* $D_2/(P_1 + P_2 + P_3)$). A statistical comparison between the four detection schemes is necessary. One way of doing this is to conduct a time tracing experiment where the applied voltage (dissipated electrical power, phase difference between arms) is kept constant and the output optical power is recorded over time. The standard deviation σ of each scheme is then calculated, however, those of the normalized group cannot be directly compared to those of the unnormalized group (the units are different). Therefore the

#201434 - $15.00 USD Received 15 Nov 2013; revised 3 Feb 2014; accepted 3 Feb 2014; published 13 Feb 2014
(C) 2014 OSA

minimum detectable phase shift $\Delta\phi_{min}$ is introduced and used to compare all schemes directly; it is defined as [23]:

$$\Delta\phi_{\min} = \frac{\Delta P_{\min}}{\left|\frac{\partial P}{\partial \phi}\right|} = \frac{k\sigma}{\left|\frac{\partial P}{\partial \phi}\right|} \tag{4.7}$$

where the minimum detectable change in power ΔP_{min} is taken as the corresponding σ times a factor k, say $k = 2$. Rewriting Eq. (4.1.b) by removing all the perturbation terms, we obtain:

$$P_2 = \left(a\cos\phi + b_2\right) P_{in} \tag{4.8}$$

from which $\partial P_2/\partial\phi$ is obtained as:

$$\frac{\partial P_2}{\partial \phi} = \left(a\sin\phi\right) P_{in} \tag{4.9}$$

substituting Eq. (4.9) into Eq. (4.7) yields the minimum detectable phase shift based on P_2:

$$\Delta\phi_{\min}\big|_{P_2} = \frac{k}{\left(a\sin\phi\right) P_{in}} \sigma\big|_{P_2} \tag{4.10}$$

Similarly, the $\Delta\phi_{min}$ for the other individual powers P_1 and P_3 are obtained, and so are those for the power differences, the normalized individual powers and the normalized power differences:

$$\Delta\phi_{\min}\big|_{D_2} = \frac{k}{\left(3a\sin\phi\right) P_{in}} \sigma\big|_{D_2} \tag{4.11}$$

$$\Delta\phi_{\min}\Big|_{\frac{P_2}{P_1+P_2+P_3}} = \frac{k}{\frac{a}{b_1+b_2+b_3}\sin\phi} \sigma\Big|_{\frac{P_2}{P_1+P_2+P_3}} \tag{4.12}$$

$$\Delta\phi_{\min}\Big|_{\frac{D_2}{P_1+P_2+P_3}} = \frac{k}{\frac{3a}{b_1+b_2+b_3}\sin\phi} \sigma\Big|_{\frac{D_2}{P_1+P_2+P_3}} \tag{4.13}$$

For maximum sensitivity, the device operates in the linear region where the $\cos\phi$ term in Eq. (4.8) is very close to 0, so $\sin\phi \sim 1$. Substituting this and $k = 2$ into Eqs. (4.10)-(4.13), with our experimental value for P_{in} and the standard deviations obtained from a time-tracing experiment, the minimum detectable phase shifts of the four schemes can be calculated and compared directly to determine which scheme provides the best performance. Table 1 gives the σ and the $\Delta\phi_{min}$ for three time-tracing experiments (nominally M 1, M 2 and M 3 in Table 1), each taken on the same triple-output MZI device with $P_{in} = 0.7$ mW (the absolute power was determined by calibration), and each with a different voltage applied so that a different output operates in the linear region (*i.e.*, M 1 has P_1 in the linear region, M 2 has P_2 in the linear region and M3 has P_3 in the linear region). The parameters $a = 0.22$ and $b_1 + b_2 + b_3 = 1.01$ are chosen by best fitting with the transfer characteristic.

#201434 - $15.00 USD Received 15 Nov 2013; revised 3 Feb 2014; accepted 3 Feb 2014; published 13 Feb 2014
(C) 2014 OSA

Table 1. Standard deviations σ and minimum detectable phase shifts $\Delta\phi_{min}$ for P_i, D_i, $P_i/(P_1 + P_2 + P_3)$, and $D_i/(P_1 + P_2 + P_3)$ of three time tracing measurements taken on the same device.

Scheme		P_i	D_i	$P_i/(P_1 + P_2 + P_3)$	$D_i/(P_1 + P_2 + P_3)$
M 1	σ	1.1 μW	2.6 μW	0.0013	0.0039
	$\Delta\phi_{min}$ **(mrad)**	14	12	12	12
M 2	σ	1.1 μW	2.3 μW	0.0011	0.0033
	$\Delta\phi_{min}$ **(mrad)**	14	9.8	10	10
M 3	σ	1 μW	1.7 μW	0.0008	0.0024
	$\Delta\phi_{min}$ **(mrad)**	13	7.4	7.3	7.3

Comparing the standard deviations of P_i and D_i for all three measurements in Table 1, suggests that there was very little time-varying output perturbation (p_o, see Eqs. (4.1.a)-(4.1.c)) in the experiments to be cancelled using the power difference scheme, because all power differences have ~2 times larger standard deviation than the individual powers. However, comparing their corresponding $\Delta\phi_{min}$ it is observed that the power difference scheme provides an reduction of ~3/2 which originates from the 3 times larger dynamic range and the 2 times worse standard deviation (compare Eq. (4.10) with Eq. (4.11)). If the standard deviation of the power difference scheme remains comparable to that of a single power then $\Delta\phi_{min}$ would be reduced by a factor of 3.

Although the cases seem to be similar considering Eqs. (4.12) and (4.13), the normalized power difference scheme does not benefit from the larger dynamic range, because there is a fixed relation between the standard deviations of both. According to the definition of D_i, $D_i/(P_1 + P_2 + P_3)$ can be expressed as $3[P_i/(P_1 + P_2 + P_3)]$-1 and thus always has a 3 times larger standard deviation than $P_i/(P_1 + P_2 + P_3)$. Substituting this relation into Eqs. (4.12) and (4.13) it is observed that the 3 times larger dynamic range of $D_i/(P_1 + P_2 + P_3)$ is cancelled and the $\Delta\phi_{min}$ remains the same. Therefore the normalized individual power and the normalized power difference can actually be regarded as the same scheme. This is verified experimentally by comparing $\Delta\phi_{min}$ of $P_i/(P_1 + P_2 + P_3)$ and $D_i/(P_1 + P_2 + P_3)$ in Table 1.

A comparison of $\Delta\phi_{min}$ of the power difference scheme and the normalized schemes reveals very similar values though not exactly equal, However, both are smaller compared to the individual power scheme, thus both are good schemes. The smallest value of $\Delta\phi_{min}$ obtained in these experiments was 7.3 mrad compared to 3.1 mrad in the dual-output case [23]. The length of the active region of both MZIs is similar so this is not the cause of the larger $\Delta\phi_{min}$ in the triple-output case. Considering that the two cases were tested under different experimental conditions, and the perturbation levels were neither controllable nor comparable, the larger detection limit in the triple-output case is attributed to larger perturbations that were not as easily suppressed. Relative to the dual-output, the triple-output eliminates the sensitivity fading and directional ambiguity in the former (there is always one output in a linear region).

5. Conclusions

In the interest of both thermal-optic and bio-chemical sensing applications, LRSPP triple-output MZIs were thermo-optically characterized at a free-space operating wavelength of ~1370 nm. The device consists of a MZI and a triple coupler in cascade, implemented with Au stripe waveguides 5 μm wide and 35 nm thick cladded with Cytop. The thermo-optic phase modulation was applied to one arm of the MZI, heated by injecting electrical currents thereon through metal probes. A theoretical model for three-waveguide coupling was proposed, implemented and validated by comparisons to literature results and to the measurements. The approach is based on modal analysis and overlap integrals, and is easy to

#201434 - $15.00 USD Received 15 Nov 2013; revised 3 Feb 2014; accepted 3 Feb 2014; published 13 Feb 2014
(C) 2014 OSA

implement. Dimensions for the triple coupler were chosen by optimizing the performance. As expected, the three output optical powers were sinusoidally related to the thermally induced phase shift and separated ~$2\pi/3$ rad. Four detection schemes were proposed and analyzed, and applied to improve the detection limit. Improvements are obtained from a 3 times larger dynamic range as well as the suppression of time-varying common perturbations, relative to a single output. The power difference scheme and the normalization schemes were found to be equally effective. A minimum detectable phase shift ($\Delta\phi_{min}$) ~2/3 that of a single output was obtained. The smallest value of $\Delta\phi_{min}$ obtained was 7.3 mrad. The device is of interest for sensing applications.

Acknowledgments

The authors are grateful to Robin Buckley for helpful discussions and assistance with the modeling work, and to Ewa Lisicka-Skrzek and Hamoudi Asiri for sample preparation and fabrication, respectively.

#201434 - $15.00 USD Received 15 Nov 2013; revised 3 Feb 2014; accepted 3 Feb 2014; published 13 Feb 2014
(C) 2014 OSA

Chapter 5

Optical bulk sensing using LRSPP dual-output MZIs

5.1 Summary

In this chapter, optical bulk (refractometric) sensing of sample solutions is demonstrated using dual-output Mach-Zehnder interferometers built from long-range surface plasmon-polariton waveguides operating at a free-space wavelength of 1375 nm. The device of interest was constructed by embedding Au stripes in Cytop claddings and etching a fluidic channel through the top cladding of one arm of the interferometer to expose the Au stripe. Bulk sensing was carried out by flowing sequentially a series of solutions of different refractive index through the microfluidic channel. The optical powers of the two outputs responded sinusoidally and were complimentary as expected in theory. Three detection schemes aiming at improving the detection limit are analyzed, showing that the device benefits from a 2× larger dynamic range, and has the ability to suppress common perturbations, relative to a single output. A detection limit of ~4×10^{-6} RIU is demonstrated which can be further improved by lengthening the sensing channel.

5.2 Contribution

The results provided in this chapter were published as an article in the *Journal of Lightwave Technology*. I designed and built the experimental setup, I developed the theoretical model, I generated and interpreted the theoretical and experimental results, and wrote the manuscript. Prof. Berini contributed to the design of the experiments and experimental setup, the

interpretation of the results, and revised the manuscript. Wei Ru Wong contributed to the design and construction of the experimental setup. Hamoudi Asiri fabricated the devices used in the experiments.

5.3 Article

The published article follows verbatim.

Bulk Sensing Using a Long-Range Surface-Plasmon Dual-Output Mach–Zehnder Interferometer

Hui Fan and Pierre Berini, *Fellow, IEEE, Fellow, OSA*

***Abstract*—Optical bulk (refractometric) sensing of sample solutions is demonstrated using dual-output Mach–Zehnder interferometers built from long-range surface-plasmon polariton waveguides operating at a free-space wavelength of 1375 nm. The device of interest was constructed by embedding Au stripes inCytop-claddings and etching a fluidic channel through the top cladding of one arm of the interferometer to expose the Au stripe. Bulk sensing was carried out by flowing sequentially a series of solutions of different refractive index through the microfluidic channel. The optical powers of the two outputs responded sinusoidally and were complimentary, as expected in theory. Three detection schemes aiming at improving the detection limit are analyzed showing that the device benefits from a 2× larger dynamic range, and has the ability to suppress common perturbations, relative to a single output. A detection limit of $\sim 4 \times 10^{-6}$ RIU is demonstrated, which can be further improved by lengthening the sensing channel. The device is promising for application as a biosensor.**

***Index Terms*—Dual-Output, mach-zehnder interferometer, long-Range, optical sensing, surface plasmon-polariton.**

I. Introduction

BIOCHEMICAL sensing plays an important part in medical diagnosis and in the detection of drugs and pathogens. A common method to conduct biosensing is to label the target biomolecules with fluorescent dyes [1], but this method induces problems such as photo-bleaching and signal bias, and it is also time consuming to perform detection. Label-free optical biosensing allows for detection without labelling biomolecules as well as real-time monitoring [2]. Initially, optical biosensing was dominated by surface plasmon resonance (SPR) based on the Kretschmann–Raether configuration consisting of a prism with a thin layer of Au integrated with fluidics and a charge-coupled device (CCD) detector, interrogated with a transverse magnetic (TM) polarized beam [3]–[5]. Phase-sensitive SPR sensing schemes based on Mach–Zehnder interferometers (MZIs) [6], Fabry–Perot interferometers [7], and optical fibers [8] were also developed.

Long-range surface plasmon-polaritons (LRSPPs) are TM polarised optical surface waves that propagate typically along a thin metal slab or stripe bounded by dielectrics of similar refractive index (RI), formed by the coupling of single-interface surface plasmon-polaritons (SPPs) at each metal–dielectric interface, and having significantly lower attenuation and thus longer propagation length than the latter [9]. Among the LRSPP modes supported by the stripe, the fundamental mode exhibits a Gaussian-like field distribution enabling end-fire excitation, while higher-order modes can be cut-off by properly designing the dimensions of the stripe. LRSPPs are useful for applications such as integrated optics [9], amplifiers and lasers [10], [11], thermo-optic modulation [12]–[15], and biochemical sensing [16]–[24].

In recent years, LRSPPs have demonstrated advantages in biosensing. Their longer propagation length allows for a longer sensing surface to be used, leading to better sensitivity and lower detection limits [16]. LRSPPs exploited in prism-coupled sensors have been reported to perform better than conventional SPR [17]–[20]. LRSPPs excited in end-fire coupled sensors based on a straight waveguide with a microfluidic channel etched into the top cladding have been successfully tested by monitoring changes in the loss of LRSPPs during sensing [21]–[23]. LRSPP single-output MZIs with a microfluidic channel etched into the top cladding of one arm have been used as a refractometric sensor for bulk sensing [24], [25]. Biosensors using single-interface SPPs [26] and metal–insulator–metal SPPs [27], also based on MZIs, have been demonstrated.

MZIs based on dielectric waveguides can also be used for sensing applications (e.g., [28]). Compared to sensors based on dielectric waveguides, there are many advantages using Au LRSPP waveguides: Surface chemistries for Au are well-known and easy to apply. Also, the fabrication of Au stripe structures, using standard photolithography with metal evaporation and lift-off, is straightforward. The Au waveguides can also be used for other purposes in addition to biosensing, such as enabling thermo-optic phase modulation, to improve the signal-to-noise ratio.

Previously, dual-output MZIs based on LRSPPs have been shown to provide a 2× larger dynamic range relative to single-output MZIs, along with the ability to suppress common perturbations, within the context of thermo-optic actuation [14]. However, such structures have yet to be applied to sensing, thus motivating the present investigation. To enable sensing, a microfluidic channel is required on chip, along with a fluidic fixture and new experimental protocols. Additionally, existing theoretical models (such as proposed in [14]) must be altered to take into account extra losses introduced by the microfluidic channel (i.e., the MZI is unbalanced). In Section II, we develop a theoretical model for unbalanced dual-output MZIs sensors. In Section III, we determine experimentally the optimal sensing

Manuscript received December 19, 2015; revised February 22, 2016; accepted March 14, 2016. Date of publication March 15, 2016; date of current version April 13, 2016.

H. Fan is with the School of Electrical Engineering and Computer Science, and the Centre for Research in Photonics, University of Ottawa, Ottawa, ON K1N 6N5, Canada [redacted]

P. Berini is with the School of Electrical Engineering and Computer Science, the Department of Physics, and the Centre for Research in Photonics,University of Ottawa, Ottawa, ON K1N 6N5, Canada [redacted]

This paper has supplementary downloadable material available at http://ieeexplore.ieee.org.

Color versions of one or more of the figures in this paper are available online at http://ieeexplore.ieee.org.

Digital Object Identifier 10.1109/JLT.2016.2543138

0733-8724 © 2016 IEEE. Personal use is permitted, but republication/redistribution requires IEEE permission.

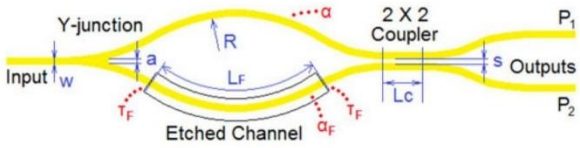

Fig. 1. Sketch of the structure. The dimensions labeled on the parts are: $w = 5\ \mu$m, $R = 5.5$ mm, $a = 2\ \mu$m, $L_c = 100.25\ \mu$m, $s = 3\ \mu$m, and $L_F = 1.1985$ mm.

wavelength, we analyze the noise level, and discuss the detection limit. We provide a brief conclusion in Section IV.

II. Theoretical Study

A. Dimensions of the Structure

Fig. 1 shows a sketch of the structure of interest in this paper. A dual-output MZI is composed of a MZI in cascade with a 3-dB (50:50) coupler. The important dimensions are labeled in the figure. All Au stripes forming the waveguides are designed to be of the same width $w = 5\ \mu$m and thickness $t = 35$ nm. All curved sections follow the same radius of curvature $R = 5.5$ mm. The Y-junction at the split has an inner waveguide separation of $a = 2\ \mu$m. The coupler section has a coupling length $L_c = 100.25\ \mu$m and a coupling separation $s = 3\ \mu$m. A microfluidic channel of path length $L_F = 1.1985$ mm is etched into the top cladding of the sensing arm to expose the Au stripe for sensing. When the RI of the solution filling the channel changes, the effective index of the LRSPP mode passing though this waveguide section will change accordingly, producing a phase shift between the two arms of the MZI and thus modulating the optical powers emerging from the two outputs.

B. Modal Analysis

In addition to producing a phase shift, changing the RI of the sensing solution causes a mismatch between the bottom cladding and the solution in the channel which produces a change in the attenuation along the sensing arm (α_F in Fig. 1) compared to the reference arm (α in Fig. 1). As the attenuation in the channel changes and transition losses are induced at the input and output of the channel, the optical powers emerging from the two arms of the MZI become unequal and the MZI unbalanced. Following Ref. [14] but introducing terms relevant in the unbalanced case, we obtain expressions for the two output optical powers P_1 and P_2 emerging from the MZI:

$$P_1 = \frac{1}{2} P_{\rm inc} A \left[\frac{B+1}{2} + \sqrt{B} \sin(\phi + \phi_0) \right] \quad (1.1)$$

$$P_2 = \frac{1}{2} P_{\rm inc} A \left[\frac{B+1}{2} - \sqrt{B} \sin(\phi + \phi_0) \right]. \quad (1.2)$$

From the above, the difference and sum of the two output powers are expressed as:

$$P_1 - P_2 = P_{\rm inc} A \sqrt{B} \sin(\phi + \phi_0) \quad (1.3)$$

$$P_1 + P_2 = P_{\rm inc} A \frac{B+1}{2}. \quad (1.4)$$

Thus, the normalized power difference between the two outputs is expressed as:

$$\frac{P_1 - P_2}{P_1 + P_2} = \frac{2\sqrt{B}}{B+1} \sin(\phi + \phi_0). \quad (1.5)$$

In these equations, we have:

$$A = e^{-2(\alpha L + \tau)} \quad (1.6)$$

$$B = e^{-2(\alpha_F - \alpha) L_F} |T_F|^2 = e^{-2[(\alpha_F - \alpha) L_F + 2\tau_F]} \quad (1.7)$$

$$\phi = \frac{2\pi L_F}{\lambda} (n_{{\rm eff},F} - n_{{\rm eff},C}) = \frac{2\pi L_F}{\lambda} \frac{\partial n_{{\rm eff},F}}{\partial n_F} (n_F - n_C) \cong \frac{\pi L_F}{\lambda} (n_F - n_C). \quad (1.8)$$

Here $P_{\rm inc}$ is the power incident on the input facet, A is the loss factor of the whole structure (including input transmittance), B is the unbalance factor which depends on the fluid RI, ϕ and ϕ_0 are the phase shift induced by the solution in the fluidic channel and the initial phase difference between the two arms, α and α_F are the mode field attenuation coefficients of the cladded and fluidic waveguides, L is the total path length of the device, L_F is the path length of the waveguide in the channel, τ and τ_F model the total transition loss of a fully-cladded device and the extra transition loss per interface between the cladded and fluidic sections, T_F is the transmittance at a junction of the cladded to fluidic waveguide (relates to τ_F as $T_F = \exp(-2\tau_F)$), λ is the operating wavelength, $n_{{\rm eff},C}$ and $n_{{\rm eff},F}$ are the effective indices of the cladded and fluidic waveguides, and n_C and n_F are the RIs of the claddings and the solution in the fluidic channel, respectively. In deriving these equations we made the assumptions that the coupler operates at its 3-dB wavelength, the radiation losses along the curved sections are negligible, and the RIs satisfy the relation $n_F - n_C \cong 2(n_{{\rm eff},F} - n_{{\rm eff},C})$, as the bulk sensitivity of the LRSPP is $\partial n_{{\rm eff},F} / \partial n_F \sim 0.5$ [16].

The unbalance factor B varies with the RI of the solution filling the channel. When the RI of the solution matches that of the claddings we have $B = 1$. B approaches 0 when the index mismatch increases and the loss of the sensing arm increases accordingly. From Eqs. (1.1) and (1.2) we find that unbalanced arms reduce the sensitivity of the sinusoidal P-ϕ signal by $B^{1/2}$ as the peak power decreases and the valley power increases. The performance is ideal when the MZI is balanced, but the two outputs always remain complementary irrespective of changes in B. Similar observations apply to the power difference and the normalized power difference given by Eqs. (1.3) and (1.5).

Fig. 2 shows computational results for this structure (obtained using COMSOL) of α_F and the total transition loss factor due to the channel given by $|T_F|^2 = \exp[-2(2\tau_F)]$ as a function of n_F at an operating free-space wavelength of 1310 nm. The B factor calculated over this range of n_F (1.333 to 1.3366) varies between 0.84 and 0.91 using Eq. (1.7), showing that the change of the optical power passing through the sensing arm is small and the B factor can be regarded as constant within this range of n_F.

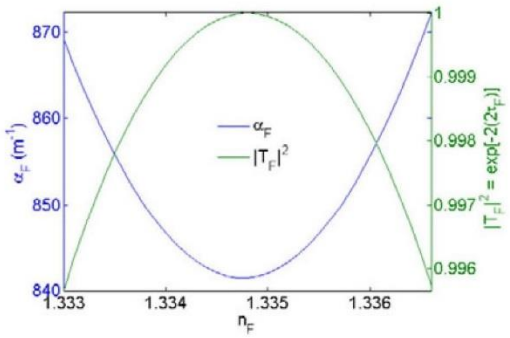

Fig. 2. Mode field attenuation coefficient and total transition loss factor due to the channel as a function of the solution RI in the microfluidic channel.

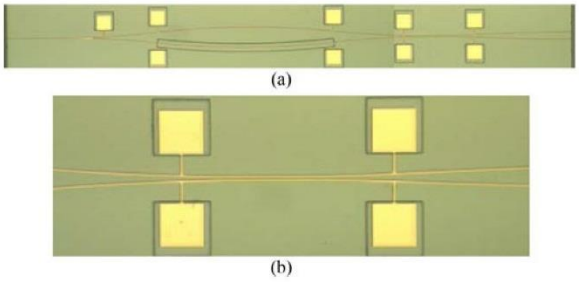

Fig. 3. Microscope images of (a) the dual-output MZI used for bulk sensing and (b) the coupler portion of the device under a higher magnification.

III. Experimental Study

A. Device, Setup and Test Solutions

Fig. 3(a) gives a microscope image of the device tested in the experiments. Fig. 3(b) shows a high-magnification microscope image of the 2×2 coupler of the device. All devices originate from the same wafer (internally identified as ND II). The wafer was fabricated by first spin-coating a 10 μm thick Cytop layer on a 450 μm thick silicon substrate as the bottom cladding, followed by a 35 nm thick Au layer patterned into the designed structures via a lift-off lithography process. Then another 10 μm thick Cytop layer was spin-coated as the top cladding and subsequently etched to expose part of the Au stripe forming one arm of the MZI in order to apply the sensing solutions. Fabrication details can be found in Refs. [29] and [30].

Fig. 4(a) illustrates the block diagram of the setup. Light tuned to the designed or optimized operating wavelength was guided in from a tunable laser via a polarisation maintaining fiber, and the output light from the device was received by a microscope objective and a CCD camera. An attenuation system producing ~30 dB of insertion loss was placed in front of the camera to prevent it from saturating. Liquid flow was driven by a syringe pump through a microfluidic fixture holding the MZI under test at an adjustable flow rate. Fig. 4(b) shows a sketch of the microfluidic fixture with a device under test. After mounting the device on a metal holder (not shown), a transparent plastic cover was fixed to the top using plastic screws. The gap between the cover and the device was sealed using a rubber O-ring to form

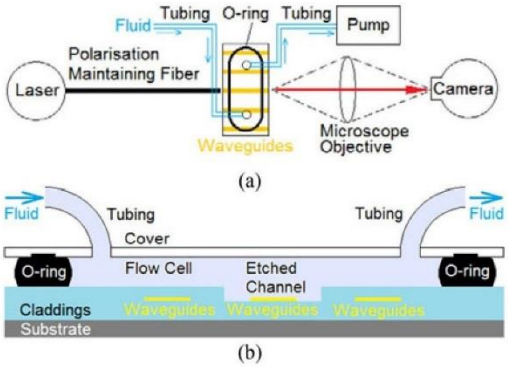

Fig. 4. Sketch of (a) the setup for bulk sensing and (b) the microfluidic fixture.

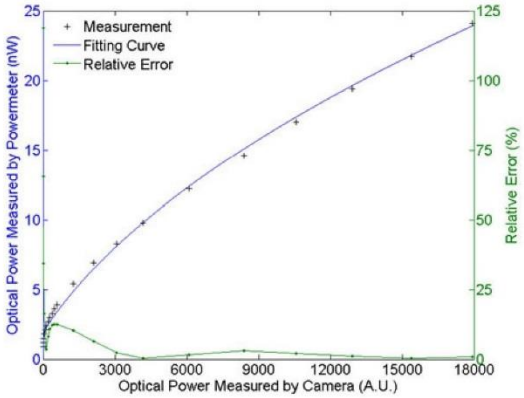

Fig. 5. Calibration of camera power in a.u. to power in nanowatt and the relative error.

an airtight flow cell above the etched channel of the device. Sample solutions were pulled into the flow cell from sample vials via fluidic tubes connected to a syringe pump (pulling), thus changing the bulk RI in the channel, leading to a phase shift between the arms and modulation of the outputs.

The setup was covered by an opaque tent and in most cases the experiments were conducted with the tent fully closed and all illumination in the lab turned off, aiming at excluding as much background light as possible. The laser and camera were controlled by LabView programs to change the input power and operating wavelength, and to take output mode images at every time step (0.5 s). The mode images were recorded in spreadsheets by frame-grabber software (LBA-710PC, Ophir Spiricon) and were post-processed to measure the powers inside two preset software apertures overlapping the two output mode spots using MATLAB. In this way the two output optical powers were obtained in arbitrary units (a.u.) then converted to nW via calibration to a known power.

Fig. 5 shows the measurements on which the calibration is based. The same set of output powers were measured using the camera with image post-processing, and in nW using a power meter. As observed in the figure, the relationship is not linear so it is necessary to fit an analytical model to the measurements.

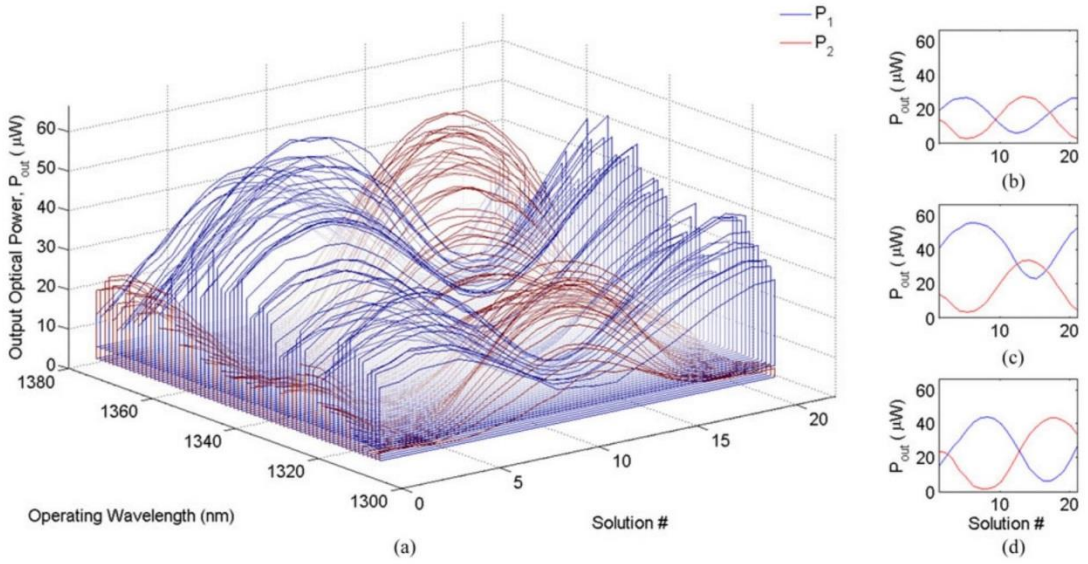

Fig. 6. (a) Waterfall plot of transfer characteristics from 1310 to 1378 nm, and typical transfer characteristics at (b) 1326, (c) 1350, and (d) 1375 nm.

The fitting equation was then used to convert the camera measurements to powers in nanowatt. Except for powers that are too small to be used in the experiments, the relative error is less than 5%, indicating that the fit is good. The fitting equation is:

$$P_{PowerMeter}\,(\mathrm{nW}) = [0.05 \times (P_{\mathrm{Camera}}\,(\mathrm{a.u.}) + 1792)]^{\frac{1}{2}} - 7.5. \quad (1.9)$$

In optical sensing, it is important to properly clean and protect the bare Au surface in the channel from possible contamination. A cleaning protocol must be followed when new devices are picked from a wafer. First the device is cleaned in heptane in an ultrasonic bath (37 kHz, 50% power) for 5 min to remove particles from the facets. Then dicing resist is removed from the top surface by placing the device in acetone for 5 min, then flushing with clean acetone and placing in clean acetone for an additional 30 min, then flushing with isopropyl alcohol (IPA), and drying with N_2 gas. Next, in order to remove residual organics, we placed the device in a UV/Ozone chamber for 15 min with the ultraviolet lamp on, and another 15 min with the Ozone only. Finally we incubate the device in 1% 16-mercaptohexadecanoic acid (16-MHA) in IPA overnight to stabilize and make the Au surface hydrophilic. It is important to flush the device with plenty of distilled/deionized (DDI) H_2O before experiments, because any residual IPA in the channel may react with glycerol used in the sample solutions, perturbing sensing.

After the experiments, surface cleaning was conducted before re-use to remove any possible residue on the sensing arm. Prior to removal of the device from the setup, we flowed a 5% (weight to weight) solution of sodium dodecyl sulfate in H_2O at a flow rate of 20 μL/min for 15 min and DDI H_2O at 20 μL/min for 20 min to clean the microfluidic system and remove any possible (loosely bound) contaminants. After dismounting the device, we flushed it with DDI H_2O and IPA in succession, dried with N_2, and placed in the UV/Ozone chamber in the same way as in the cleaning protocol.

The sample solutions used in the experiments are H_2O-glycerol mixtures prepared in a series of 21 solutions with a constant RI step between them and the RI of the middle ones close to that of the Cytop claddings (~1.3348 near 1310 nm). H_2O and glycerol were mixed by measuring a volume of DDI H_2O and a mass of glycerol, but the cup and the scale are neither precise enough nor convenient to prepare every solution in the series because the RI step is small. Instead, only the two with the lowest and highest RIs (targeted as 1.333 and 1.336) in the series were prepared using this method, yielding two "stock solutions" that were then mixed using precision pipetting to generate the rest of the series. A Metricon prism coupler was used to verify the RI of the two stock solutions to an accuracy of $\pm 1 \times 10^{-4}$ refractive index unit (RIU), which is the absolute accuracy on all of our solutions. A more accurate value for the index step is determined by fitting theory to the measurements (below). Metricon measurements on pure glycerol and DDI H_2O were also obtained to provide RIs, the former being 1.4699 and the latter 1.3196 respectively.

B. Wavelength Sweeps

The devices were originally designed to operate at 1310 nm. However, due to fabrication imperfections the operating wavelength is shifted because the coupling section in the device does not work as a 3-dB (50:50) coupler at 1310 nm. To find the new operating wavelength, sweeping experiments from 1310 to 1378 nm were conducted for each solution and the corresponding output optical powers from the two outputs of the device were recorded. The input optical power was kept constant and the initial alignment was unchanged so as to make the curves at different wavelengths comparable to each

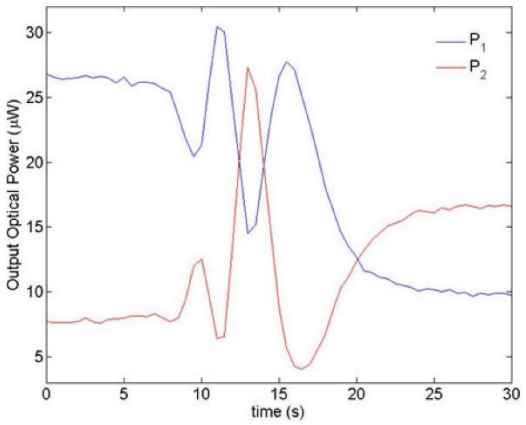

Fig. 7. Time tracing experiment showing one solution replacing another in the flow cell.

other. The results obtained from the whole set of solutions are shown in Fig. 6(a) as a waterfall plot of transfer characteristics at each wavelength and in Media 1 as a short movie for clearer observation. It is obvious that the longer the wavelength, the higher the peak powers, which is reasonable since the attenuation at longer wavelength is comparatively lower. Fig. 6(b)–(d) gives three typical transfer characteristics selected from the waterfall plot, at wavelengths of 1326, 1350 and 1375 nm, respectively. At 1350 nm, the outputs have different offsets such that the valley of one output nearly reaches the peak of the other, because the coupler is not 3-dB (50:50) at this wavelength. At 1375 nm, no obvious offset is observed and the two outputs are close to ideal. At 1326 nm there is no obvious offset either but the powers are lower due to higher attenuation. By comparing the transfer characteristics at all wavelengths, 1375 nm was chosen as the operating wavelength.

C. Transfer Characteristics and Time Traces

Fig. 7 give a time trace obtained as one solution replaces another in the fluidic fixture. The powers oscillate as the fluids exchange due to mixing within the fluidic fixture. About 20 s are required for the fluids to completely exchange at a flow rate of 20 μL/min. We henceforth wait for $\sim$3 min after injecting a new solution into the system before recording the outputs to allow for replacement of the solution and for the output powers to stabilize. Media 2 shows a movie of the changes in the two output mode spots recorded during this process.

We then obtained a time-dependent transfer characteristic by recording the two output powers over $\sim$60 s for each solution injected in sequence, while keeping the input power, wavelength and initial alignment unchanged. The output powers were averaged over 60 s for each solution and used to produce the transfer characteristic. Thus, each data point in the transfer characteristic is associated with a time trace from which noise statistics can be extracted.

Fig. 8(a) shows the transfer characteristic measured in this manner. As expected, the two outputs are sinusoidal with solution number which is linearly related to the solution RI.

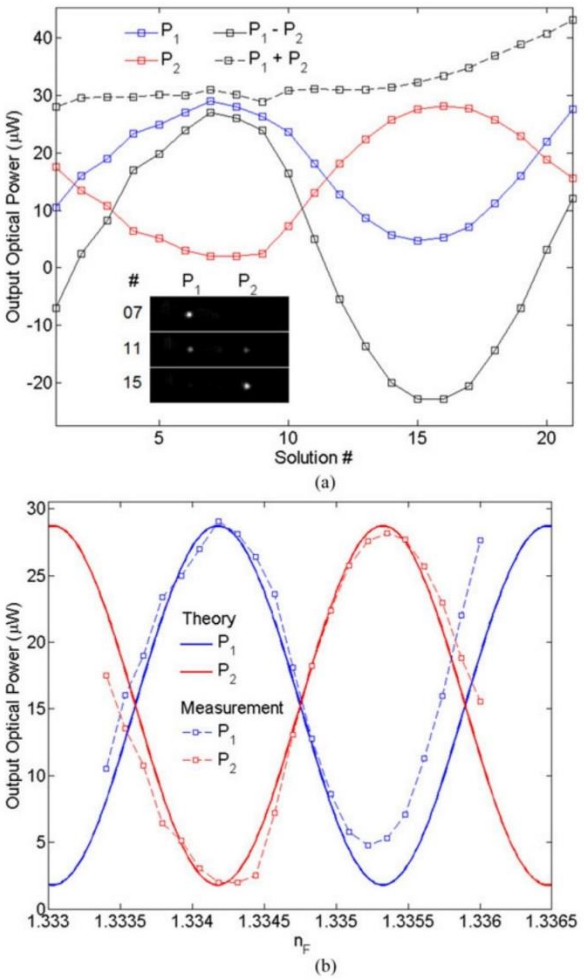

Fig. 8. (a) Transfer characteristics measured at 1375 nm, and (b) comparison with theoretical expectations.

TABLE I
RIs Corresponding to Solution Number

Solution #	RI	Solution #	RI	Solution #	RI
01	1.33340	08	1.33431	15	1.33522
02	1.33353	09	1.33444	16	1.33535
03	1.33366	10	1.33457	17	1.33548
04	1.33379	11	1.33470	18	1.33561
05	1.33392	12	1.33483	19	1.33574
06	1.33405	13	1.33496	20	1.33587
07	1.33418	14	1.33509	21	1.33600

The power difference between the outputs is also plotted and shows a larger dynamic range of $\sim$2$\times$ relative to the individual outputs as the two are complementary. A mosaic clearly identifying power switching between the outputs is given as the inset. The total output power remains generally constant but increases with RI over the last several solutions.

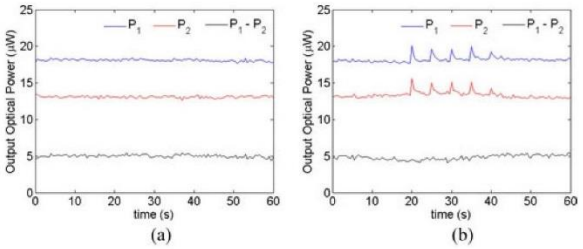

Fig. 9. Time traces associated with Solution 11 at 1375 nm with (a) natural noise and (b) artificial noise.

The measurements were compared to theory by adjusting the terms in Eqs. (1.1) and (1.2) over reasonable ranges to optimize the fit; Fig. 8(b) shows that the fit achieved is generally good. We chose $\alpha = 0.5756$ mm^{-1} (5 dB/mm, consistent with Ref. [31]), $\alpha_F = 0.9210$ mm^{-1} (8 dB/mm, consistent with Ref. [24]), $e^{-2\tau} = 0.7144$ (1.4606 dB, determined by fitting), $|T_F|^2 = 0.8264$ (0.8281 dB, by fitting) and $\phi_0 = 3.2812$ rad (by fitting), using $L = 3.8053$ mm and $L_F = 1.1985$ mm from the device layout, and $P_{\rm inc} = 7$ dBm and $\lambda = 1375$ nm from the experimental conditions. From Eq. (1.8), ϕ depends on L_F and λ which are known, so the period of the theoretical transfer characteristic can be used to extract the step in the RI of the solutions by fitting, which works out to $\Delta n_F = 1.3 \times 10^{-4}$. The RIs assigned to the solutions used in the measurements are given in Table I. It is observed that no solution lies exactly at a crossing point where maximum sensitivity occurs. The two curves cross between Solutions 11 and 12 with corresponding RIs of 1.33470 and 1.33483 (see Table I), which are close to the RI of Cytop ($\sim$1.3348). This is reasonable because the device is designed to produce equal power output when the RI of the solution matches that of the cladding and when the coupler is operating at its 3-dB (50:50) wavelength.

D. Noise Analysis and Detection Limit

Fig. 9(a) shows a time trace associated with Solution 11 revealing the baseline noise in the system. Although solution 11 is not exactly at the 3-dB point, the two output powers are quite close to each other. A second experiment was carried out where the illumination on the alignment microscope in our test set-up was turned ON and OFF a few times. In this way a man-made noise source was added in a controllable manner aiming at demonstrating the ability of the device to suppress common perturbations. Fig. 9(b) shows a time trace with such artificial noise, also associated with Solution 11. It is observed that both outputs are affected similarly by the artificial noise, and that taking the power difference effectively suppresses these common perturbations as the spikes observed on the individual outputs are removed.

It is necessary to perform quantitative analysis in order to compare three detection schemes: an individual power (i.e., P_1 or P_2), a power difference (i.e., $P_d = P_1 - P_2$), and a normalized power difference (i.e., $P_n = (P_1 - P_2)/(P_1 + P_2)$). It has been clarified in Ref. [14] that a normalized individual power (i.e., $P_i/(P_1 + P_2)$, $i = 1$ or 2) and the normalized power difference produce (mathematically) the same detection limit, so the former is not discussed in this paper. The first step of the analysis is to use the transfer characteristic at 1375 nm (see Fig. 8(b)) to calculate the change in power ΔP_i (i = 1, 2, d, or n) between Solutions 11 and 12 for all schemes. Then, since we know from Table I that the RI difference between Solutions 11 and 12 is $\Delta n_F = 1.3 \times 10^{-4}$ RIU, the sensitivity near the crossing point (between Solutions 11 and 12) can be estimated as $\partial P_i/\partial n_F \cong \Delta P_i/\Delta n_F$. We use the noises $\sigma(P_i)$ obtained for Solution 11 as the standard deviation over time of the powers P_i and calculate the limit of detection (LOD) for all detection schemes as $\mathrm{LOD}(P_i) = \sigma(P_i) \cdot \mathrm{SNR}/(\partial P_i/\partial n_F)$ assuming the minimum signal-to-noise ratio required for reliable detection as SNR = 2 (following Ref. [24]). The noises, sensitivities and detection limits for all schemes are listed in Table II.

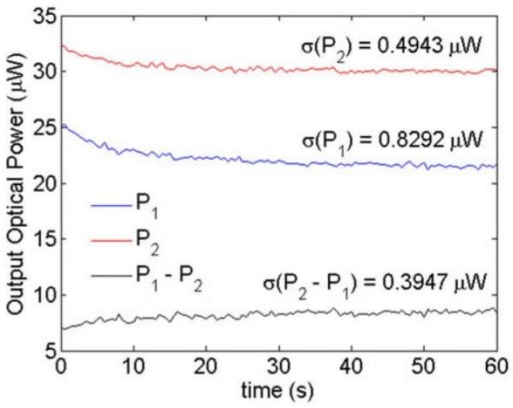

Fig. 10. Time tracing experiment showing drift.

In Table II we observe for the case of artificial noise that $\sigma(P_d)$ is smaller than the σ's of the individual powers, $\sigma(P_1)$ and $\sigma(P_2)$, meaning that some common perturbations are canceled (as observed in Fig. 9(b)). Consequently, the LODs of the P_d and P_n schemes are 2–3 times smaller than those of the individual powers, which is a significant improvement. For the case of natural noise $\sigma(P_d)$ is slightly larger than the σ's of the individual powers, showing that little common perturbation exists here. However, the LOD in this case is still improved, specifically, by a factor of $\sim$1.6 due to the 2$\times$ larger dynamic range. Comparing all of the LODs, it is observed that although those of the individual power schemes are much worse in the case of artificial noise, the P_d and P_n schemes bring the detection limits to generally the same level as in the case of natural noise, showing the effectiveness of common perturbation suppression.

Drift is also a common problem observed in optical sensing. It is thus worth investigating the ability of the device to suppress perturbations due to drift. Natural drift happened to be recorded during one of the time tracing experiments, as shown in Fig. 10. As shown in Fig. 10, $\sigma(P_d)$ is smaller than σ of the individual powers, indicating an improvement in the noise level. It is found that the two outputs do not drift at the same rate, nor is the drifting proportional to power level as the output with smaller

TABLE II
STANDARD DEVIATIONS σ'S, SENSITIVITIES $\partial P_i/\partial n_F$'S, AND DETECTION LIMITS LODS OF ALL DETECTION SCHEMES

Detection scheme		Individual power	Individual power	Power difference	Normalized power difference
Expression		P_1	P_2	$P_d = P_1 - P_2$	$P_n = P_d/(P_1 + P_2)$
P at Solution 11		18.09883 μW	13.0841 μW	5.01473 μW	0.1608
P at Solution 12		12.79298 μW	18.1963 μW	−5.40332 μW	−0.1744
ΔP Solution 11–12		5.30585 μW	5.1122 μW	10.41805 μW	0.3352
Δn_F by fitting		1.3×10^4 RIU			
$\partial P/\partial n_F$		4.081×10^4 μW / RIU	3.932×10^4 μW / RIU	8.014×10^4 μW / RIU	0.2578×10^4 RIU^{-1}
Case of natural noise	σ	0.1536 μW	0.1454 μW	0.1953 μW	0.0063
	LOD	7.53×10^{-6} RIU	7.40×10^{-6} RIU	4.87×10^{-6} RIU	4.89×10^{-6} RIU
Case of artificial noise	σ	0.4079 μW	0.4672 μW	0.3256 μW	0.0116
	LOD	10.03×10^{-6} RIU	12.15×10^{-6} RIU	4.12×10^{-6} RIU	4.61×10^{-6} RIU

power has a larger drift. As a result, the drift is not fully removed by power subtraction—there is still a slight drift on the power difference. Calibration error may contribute to the difference in the drifts, but the two output powers are too close for calibration error alone to cause such a difference. Instead, it could be caused by misalignment at the input side, where vertical misalignment causes common perturbations whereas horizontal misalignment causes a difference in the drifts. Nevertheless, the device is still capable of removing the common portion due to drift.

IV. CONCLUSION

In summary, we have demonstrated bulk refractometric sensing on LRSPP dual-output MZIs formed of Au stripes cladded with Cytop and composed of a MZI followed by a 2×2 coupler in cascade, with a microfluidic channel etched on top of the sensing arm. A theoretical model for unbalanced dual-output MZIs was proposed. Wavelength sweeping experiments were conducted in order to select the operating wavelength for the device by choosing the most ideal transfer characteristic. Time tracing experiments were conducted to obtain the crossing point of the transfer characteristic, and to analyze the natural and artificial noise associated with a crossing point. A detection limit of about 4×10^{-6} RIU was achieved by applying and comparing three detection schemes. The device shows an ability to suppress common perturbation and drift, and benefits from a $2\times$ larger dynamic range relative to its single-output counterpart. The possibility of achieving a better detection limit, for instance by increasing the sensing length, makes the structure a promising candidate for biosensing.

ACKNOWLEDGMENT

The authors would like to thank W. R. Wong and O. Krupin for help on the construction of the setup, and C. Chiu and H. Asiri for fabricating the devices.

REFERENCES

[1] P. N. Prasad, *Introduction to Biophotonics*. Toronto, ON, Canada: Wiley, 2003.
[2] M. A. Cooper, "Optical biosensors in drug discovery," *Nature Rev. Drug Discovery*, vol. 1, no. 7, pp. 515–528, 2002.
[3] S. Löfås, "Optimizing the hit-to-lead process using SPR analysis," *Assay Drug Dev. Technol.*, vol. 2, no. 4, pp. 407–416, 2004.
[4] B. N. Feltis, B. A. Sexton, F. L. Glenn, M. J. Best, M. Wilkins, and T. J. Davis, "A hand-held surface plasmon resonance biosensor for the detection of ricin and other biological agents," *Biosens. Bioelectron.*, vol. 23, no. 7, pp. 1131–1136, 2007.
[5] J. Homola, "Surface plasmon resonance sensors for detection of chemical and biological species," *Chem. Rev.*, vol. 108, no. 2, pp. 462–493, 2008.
[6] S. Y. Wu, H. P. Ho, W. C. Law, and C. Lin, "Highly sensitive differential phase-sensitive surface plasmon resonance biosensor based on the Mach-Zehnder configuration," *Opt. Lett.*, vol. 29, no. 20, pp. 2378–2380, 2004.
[7] Y. Hadjar, M. Renault, S. Blaize, A. Bruyant, R. Vincent, and A. Hmima, "Compact interferometer transducer based on surface plasmon phase resonance," *J. Opt. Soc. Am. A*, vol. 32, no. 5, pp. 771–777, 2015.
[8] H. Nguyen, F. Sidiroglou, S. F. Collins, T. J. Davis, A. Roberts, and G. W. Baxter, "A localized surface plasmon resonance-based optical fiber sensor with sub-wavelength apertures," *Appl. Phys. Lett.*, vol. 103, no. 19, p. 193116, 2013.
[9] P. Berini, "Long-range surface plasmon polaritons," *Adv. Opt. Photon.*, vol. 1, no. 3, pp. 484–588, 2009.
[10] I. De Leon and P. Berini, "Amplification of long-range surface plasmons by a dipolar gain medium," *Nature Photon.*, vol. 4, no. 6, pp. 382–387, 2010.
[11] M. C. Gather, K. Meerholz, N. Danz, and K. Leosson, "Net optical gain in a plasmonic waveguide embedded in a fluorescent polymer," *Nature Photon.*, vol. 4, no. 7, pp. 457–461, 2010.
[12] K. Leosson, T. Rosenzveig, P. G. Hermannsson, and A. Boltasseva, "Compact plasmonic variable optical attenuator," *Opt. Exp.*, vol. 16, no. 20, pp. 15546–15552, 2008.
[13] T. Rosenzveig, P. G. Hermannsson, A. Boltasseva, and K. Leosson, "Optimizing performance of plasmonic devices for photonic circuits," *Appl. Phys. A*, vol. 100, no. 2, pp. 341–346, 2010.
[14] H. Fan and P. Berini, "Noise cancellation in long-range surface plasmon dual-output Mach-Zehnder interferometers," *J. Lightw. Technol.*, vol. 31, no. 15, pp. 2606–2612, Aug. 2013.
[15] H. Fan, R. Charbonneau, and P. Berini, "Long-range surface plasmon triple-output Mach-Zehnder interferometers," *Opt. Exp.*, vol. 22, no. 4, pp. 4006–4020, 2014.
[16] P. Berini, "Bulk and surface sensitivities of surface plasmon waveguides," *New J. Phys.*, vol. 10, no. 10, p. 105010, 2008.
[17] J. Dostálek, A. Kasry, and W. Knoll, "Long range surface plasmons for observation of biomolecular binding events at metallic surfaces," *Plasmonics*, vol. 2, no. 3, pp. 97–106, 2007.
[18] R. Slavík and J. Homola, "Ultrahigh resolution long range surface plasmon-based sensor," *Sens. Actuators B Chem.*, vol. 123, no. 1, pp. 10–12, 2007.
[19] M. Vala, S. Etheridge, J. A. Roach, and J. Homola, "Long-range surface plasmons for sensitive detection of bacterial analytes," *Sens. Actuators B Chem.*, vol. 139, no. 1, pp. 59–63, 2009.
[20] V. Chabot, Y. Miron, M. Grandbois, and P. G. Charette, "Long range surface plasmon resonance for increased sensitivity in living cell biosensing through greater probing depth," *Sens. Actuators B Chem.*, vol. 174, pp. 94–101, 2012.
[21] O. Krupin, H. Asiri, C. Wang, R. N. Tait, and P. Berini, "Biosensing using straight long-range surface plasmon waveguides," *Opt. Exp.*, vol. 21, no. 1, pp. 698–709, 2013.
[22] O. Krupin, C. Wang, and P. Berini, "Selective capture of human red blood cells based on blood group using long-range surface plasmon waveguides," *Biosens. Bioelectron.*, vol. 53, pp. 117–122, 2014.

[23] W. R. Wong, O. Krupin, S. D. Sekaran, F. R. M. Adikan, and P. Berini, "Serological diagnosis of dengue infection in blood plasma using long-range surface plasmon waveguides," *Anal. Chem.*, vol. 86, no. 3, pp. 1735–1743, 2014.
[24] A. Khan, O. Krupin, E. Lisicka-Skrzek, and P. Berini, "Mach-Zehnder refractometric sensor using long-range surface plasmon waveguides," *Appl. Phys. Lett.*, vol. 103, no. 11, p. 111108, 2013.
[25] K. C. Vernon, D. E. Gómez, and T. J. Davis, "A compact interferometric sensor design using three waveguide coupling," *J. Appl. Phys.*, vol. 106, no. 10, p. 104306, 2009.
[26] Y. Gao, Q. Gan, Z. Xin, X. Cheng, and F. J. Bartoli, "Plasmonic Mach-Zehnder interferometer for ultrasensitive on-chip biosensing," *ACS Nano*, vol. 5, no. 12, pp. 9836–9844, 2011.
[27] X. Zeng, Y. Gao, H. Hu, D. Ji, Q. Gan, and F. J. Bartoli, "A metal-insulator-metal plasmonic Mach-Zehnder interferometer array for multiplexed sensing," *J. Appl. Phys.*, vol. 113, no. 13, p. 133102, 2013.
[28] S. M. Lindecrantz, J. C. Tinguely, B. S. Ahluwalia, and O. G. Hellesø, "Characterization of a waveguide Mach-Zehnder interferometer using PDMS as a cover layer," *J. Eur. Opt. Soc. Rapid Publ.*, vol. 10, p. 15020, 2015.
[29] C. Chiu, E. Lisicka-Skrzek, R. N. Tait, and P. Berini, "Fabrication of surface plasmon waveguides and devices in Cytop with integrated microfluidic channels," *J. Vac. Sci. Technol. B*, vol. 28, no. 4, pp. 729–735, 2010.
[30] H. Asiri, "Fabrication of surface plasmon biosensors in cytop," Master's thesis, Dept. Chem. Biol. Eng., Univ. Ottawa, Ottawa, ON, Canada, 2012.
[31] H. Fan, R. Buckley, and P. Berini, "Passive long-range surface plasmon-polariton devices in Cytop," *Appl. Opt.*, vol. 51, no. 10, pp. 1459–1467, 2012.

Hui Fan received the B.Sc. degree in optoelectronics from Nankai University, Tianjin, China, in 2008, and the M.A.Sc. degree in electrical engineering from the University of Ottawa, Ottawa, ON, Canada, in 2011, where he is currently working toward the Ph.D. degree in electrical engineering.

He was a Research Assistant with the Centre for Research in Photonics, University of Ottawa, from 2009 to 2015. His research topic involved the application of long-range surface-plasmon polaritons in optical sensing. He characterized passive components of plasmon-based optical devices. He performed experimental noise analysis in thermooptic actuation and in bulk (refractometric) sensing and also performed Comsol and MATLAB modal analysis on dual-output and triple-output Mach–Zehnder interferometers.

Pierre Berini (F'11) received the B.E.Sc. and B.Sc. degrees in electrical engineering and computer science, respectively, from the University of Western Ontario, London, ON, Canada, and the M.Sc.A. and Ph.D. degrees in electrical engineering from École Polytechnique de Montréal, Montréal, QC, Canada.

He is a Professor of electrical engineering, a Professor of physics, the University Research Chair in Surface Plasmon Photonics, and the Director of the Centre for Research in Photonics at the University of Ottawa, Ottawa, ON. He was the Founder and Chief Technology Officer of a venture capital financed company and he collaborates on an ongoing basis with industry. He has published seven book chapters, approximately 300 scientific and technical papers in peer-reviewed periodicals and conference proceedings, and is an inventor or coinventor on 20 patents. He was an Associate Editor of *Optics Express* and is currently an Associate Editor of *Nanophotonics*. He contributes on an ongoing basis to the organization of several international conferences in photonics. His research interests include many areas of optics and photonics, with surface plasmons and their applications being of particular interest. He received an NSERC Steacie Fellowship, an NSERC Discovery Accelerator, a Premier of Ontario Research Excellence Award, the University of Ottawa Young Researcher of the Year Award, an URSI Young Scientist Award, a George S. Glinski Award for Excellence in Research, and is a Canada Foundation for Innovation Researcher. He is a Fellow of the Canadian Academy of Engineering, and a Member of the OSA and SPIE.

5.4 Supplementary

It is also observed that the curves of the two output powers are somewhat different from those obtained via the wavelength sweeping experiments at the same operating wavelength. A possible cause is the accumulation of dust on the facets of the device, which may explain the decrease of the power ranges. Another possible cause is that evaporation changed the RIs of the solutions when taking them from the vials they were stored and when flowing them through the microfluidic system from the syringes, which may explain the slight change in the period. A third cause may be that between the time tracing and the wavelength sweeping experiments, the device had been dismounted from the microfluidic system for cleaning, and reassembled to proceed. In the design of these devices, the O-ring of the microfluidic system presses on the top cladding of the coupler section and thus may affect its performance. Since the pressure may vary every time the system was reassembled, depending on how tight the cover was fixed on the jig, it is possible that the performance of the coupler could change. However, it is found in Eqs.(3.1) and (3.2) in Chapter 3 that the deviation of the coupling performance from the ideal case would not only decrease the power ranges but also add offsets to the outputs, the latter of which is not observed in our case, and so this cause probably does not contribute to the changes.

Compared to a LOD of ~1×10^{-6} RIU in Ref.[46], the LODs reported in this paper are larger, which may be caused by the measurement method. In Ref.[46] the powers were read by a power meter, while here they were measured by post-processing calibrated camera images. An experiment using the same measurement method as in this paper was conducted on a single-output MZI for verification. The LOD is 6×10^{-6} RIU, a little better than those of the individual outputs of a dual-output MZI as shown in Table 2 perhaps due to that the length of

the sensing surface of a single-output MZI (in which case L_F = 1.612 mm) is longer than that of a dual-output one and the sensitivity is higher accordingly, but still not as low as the improved LODs via either the P_d scheme or the P_n scheme. Supposing that the noise level of the individual output powers of the dual-output MZIs could be improved to match that in the single-output case in Ref.[46], the P_d and P_n schemes would have helped renew the best record of detection limit.

Chapter 6

Optical bulk sensing using LRSPP triple-output MZIs

6.1 Summary

In this chapter, a triple-output Mach-Zehnder interferometric sensor operating with long-range surface plasmon-polaritons at free-space wavelengths near 1310 nm was constructed by etching a microfluidic channel through the Cytop upper cladding of one arm of the interferometer to expose the Au stripe embedded therein. Optical bulk (refractometric) sensing was conducted by sequentially flowing sample solutions with different refractive indices through the microfluidic channel and measuring the optical powers of the three outputs, which responded sinusoidally and were separated by ~$2\pi/3$ rad as expected in theory. Three detection schemes are analyzed and compared, demonstrating that the device benefits from a 3× larger dynamic range and the ability to suppress common perturbations relative to its single-output counterpart, thus improving the detection limit.

6.2 Contribution

The results provided in this chapter were published as an article in the *Journal of the Optical Society of America B*. I designed and built the experimental setup, I developed the theoretical model and implemented the numerical methods used for the theoretical analysis, I generated and interpreted the theoretical and experimental results, and wrote the manuscript. Prof. Berini contributed to the design of the experiments and experimental setup, the development of the theoretical model, the interpretation of the results, and revised the manuscript. Wei Ru

Wong contributed to the design and construction of the experimental setup. Hamoudi Asiri fabricated the devices used in the experiments.

6.3 Article

The published article follows verbatim.

Journal of the Optical Society of America B
OPTICAL PHYSICS

Bulk sensing using a long-range surface-plasmon triple-output Mach–Zehnder interferometer

HUI FAN[1,2] AND PIERRE BERINI[1,2,3,*]

[1]Centre for Research in Photonics at the University of Ottawa, 25 Templeton, Ottawa, Ontario K1 N 6N5, Canada
[2]School of Electrical Engineering and Computer Science, University of Ottawa, 800 King Edward Ave., Ottawa, Ontario K1 N 6N5, Canada
[3]Department of Physics, University of Ottawa, 150 Louis Pasteur St., Ottawa, Ontario K1 N 6N5, Canada
*Corresponding author: [redacted]

Received 1 February 2016; revised 3 April 2016; accepted 8 April 2016; posted 8 April 2016 (Doc. ID 258602); published 10 May 2016

A triple-output Mach–Zehnder interferometric sensor operating with long-range surface plasmon–polaritons at free-space wavelengths near 1310 nm was constructed by etching a microfluidic channel through the top cladding (Cytop) of one arm of the interferometer to expose the Au stripe embedded therein. Optical bulk (refractometric) sensing was conducted by sequentially flowing sample solutions with different refractive indices through the microfluidic channel and measuring the optical powers of the three outputs, which responded sinusoidally and were separated by $\sim 2\pi/3$ rad as expected in theory. Three detection schemes are analyzed and compared, demonstrating that the device benefits from a 3× larger dynamic range and the ability to suppress common perturbations relative to its single-output counterpart, thus improving the detection limit. The device is promising for biosensing applications. © 2016 Optical Society of America

OCIS codes: (240.6680) Surface plasmons; (230.3120) Integrated optics devices.

http://dx.doi.org/10.1364/JOSAB.33.001068

1. INTRODUCTION

Nonlabeled biosensors have the advantages of reduced labor and real-time detection [1]. Surface plasmon resonance (SPR) biosensors based on the Kretschmann–Raether configuration consisting of a prism with a thin layer of Au integrated with fluidics and a CCD detector, interrogated with a transverse-magnetic (TM)-polarized beam [2,3] are the most common optical biosensors. Bloch surface wave (BSW) biosensors applying the same experimental configuration were also developed, showing increased resolution with respect to surface refractive index changes and high fluorescence collection efficiency [4]. In recent years, long-range surface plasmon–polariton (LRSPP) biosensors have been demonstrated to be advantageous due to their longer propagation length which leads to a longer sensing surface and thus compelling sensitivity and detection limits [5]. LRSPPs are TM-polarized optical surface waves, propagating typically along a nanometer thin metal stripe cladded with dielectrics and having significantly lower attenuation relative to single-interface SPPs [5]. Prism-coupled biosensors using LRSPPs have been demonstrated with better performance than conventional SPR [6–9]. End-fire-coupled LRSPP biosensors based on straight waveguides (Au stripes) with a microfluidic channel etched through the top cladding have been demonstrated by monitoring changes in the loss as biomaterial binds to the waveguide [10–13]. LRSPP single-output [14,15] and dual-output [16] Mach–Zehnder interferometers (MZIs) with a microfluidic channel etched through the top cladding of one arm have been used as refractometric sensors for bulk sensing.

MZIs are useful for biochemical sensing applications [17,18]. In the past, MZI sensors based on fibers [19], dielectric waveguides [20,21], and surface plasmon waveguides [22,23] have been demonstrated. Compared to a single-output MZI, multiple-output (e.g., dual- and triple-output) MZIs have been demonstrated to improve the detection limit due to their larger dynamic ranges and their ability to suppress common perturbations [24,25]. Specifically for the case of triple-output MZIs, a further advantage consists of always having one output operating with near-maximum sensitivity [25]. In this paper we discuss and demonstrate the ability of triple-output MZIs operating with LRSPPs to carry out optical bulk sensing. In Section 2, we introduce the device, the setup, the sample solutions, and the sensing mechanism. In Section 3, we present and discuss the sensing results, we analyze the noise levels, and discuss the detection limit. In Section 4, we summarize and present some concluding remarks.

2. EXPERIMENTAL PREPARATIONS

A. Device

A triple-output MZI consists of a MZI in cascade with a triple coupler. Figure 1(a) shows a sketch of the structure with

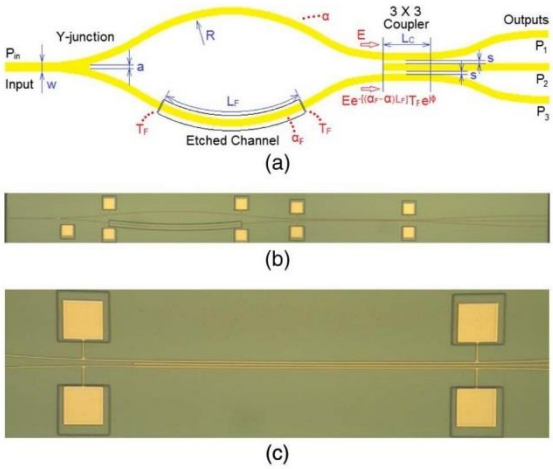

Fig. 1. (a) Sketch of the device with important dimensions labeled: $w = 5$ μm, $R = 5.5$ mm, $a = 1$ μm, $L_c = 828.57$ μm, $s = 2$ μm, and $L_F = 1.1902$ mm. (b) Microscope images of the device, and (c) high-magnification microscope image of the coupler portion.

important dimensions labeled thereon. All Au stripes are designed to be of the same width $w = 5$ μm and thickness $t = 35$ nm, and all curved sections have the same radius of curvature $R = 5.5$ mm. The Y-junction at the split has an inner waveguide separation of $a = 1$ μm. The coupler section has a coupling length $L_c = 828.57$ μm and a coupling separation $s = 2$ μm. A microfluidic channel is etched through the top cladding of the sensing arm to expose the Au stripe for sensing. The path length of the waveguide in the sensing channel is designed to be $L_F = 1.1902$ mm. The device is designed to operate at 1310 nm, with a mode power attenuation MPA = 7.1776 dB/mm and a total insertion loss ~34 dB.

When the refractive index (RI) of the sample solution that fills the channel changes, the effective index of the LRSPP passing though this waveguide section will change accordingly, producing a phase shift ϕ between the two arms, thus modulating the optical powers emerging from the three outputs due to interference in the coupler [25]. The sensing channel also causes the MZI to become unbalanced because the losses thereon are different from those along the reference arm. This is due to the change in attenuation from α to α_F and the transition losses at the input and output facets of the fluidic section, each modeled by the transmittance T_F. Figure 1(b) shows a microscope image of the device tested in the experiments. (The Au rectangular pads shown here are unrelated to the experiments of this paper; they were used for thermal tuning [25].) Figure 1(c) shows a high-magnification microscope image of the 3 × 3 coupler portion of the device. All devices originate from the same wafer (identified internally as ND II) fabricated by spin-coating a 10 μm thick Cytop layer on a 450 μm thick silicon substrate as the bottom cladding, followed by a 35 nm thick Au layer patterned into the designed structures via a metal evaporation and lift-off lithography process, and then another 10 μm thick Cytop layer as the top cladding [26,27].

B. Setup

Figure 2(a) illustrates the block diagram of the setup. Light from a tunable laser, tuned to an operating wavelength optimized for the device, was guided to the device via a polarization maintaining fiber, and the output light from the device was received by a microscope objective and a CCD camera. In front of the camera there was an attenuation system which induced a loss of ~30 dB to prevent the camera from saturating. The camera was connected to a monitor and to a computer via coaxial cable. The laser was also connected to the computer using GPIB cable for automated control. LabView programs were used to change the input power and operating wavelength and to record output mode images at every time step (set to 0.5 s) in files by frame-grabber software (LBA-710PC, Ophir Spiricon). The files were postprocessed using MATLAB to determine the powers inside three preset software apertures overlapping the three output mode spots. The powers were then calibrated in the same way as in Ref. [16] for linear response.

Sample solutions were driven through a microfluidic fixture by a syringe pump at an adjustable flow rate. Figure 2(b) shows a sketch of the microfluidic fixture holding a device under test. After mounting the device on a metal holder (not shown), a transparent plastic cover was fixed by plastic screws upon a metal holder on which the device was mounted (not shown) to cover the top of the device, forming an airtight flow cell above the etched channels with the gap between the cover and the device sealed by a rubber O-ring. A series of solutions was sequentially pulled into the flow cell from sample vials via fluidic tubes connected to the syringe pump, thus changing the bulk RI inside the channel. The whole setup was covered by an opaque tent in order to exclude as much background light as possible.

C. Sample Solutions

The sample solutions are H_2O-glycerol mixtures prepared in a series of 21 solutions with a constant RI step, with the RI of the middle one close to that of the Cytop claddings (~1.3348 near 1310 nm). In order to prepare the mixtures, a certain volume of DDI H_2O and a certain mass of glycerol were measured using a measuring cup and a scale, respectively, but neither is precise

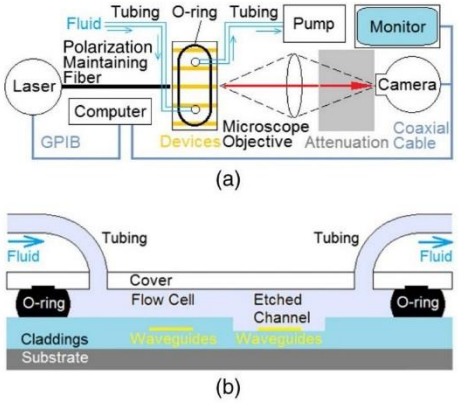

Fig. 2. Sketch of (a) the experimental setup and (b) the microfluidic fixture.

enough because the RI step is small. Therefore, only the first and the last solutions (with the lowest and highest RIs, targeted as 1.333 and 1.336, respectively) in the series were prepared in this way, yielding two "stock solutions" that were then mixed using precision pipetting to generate the rest of the series. A Metricon prism coupler was used to verify the RIs of the two stock solutions as well as pure glycerol (1.4699) and DDI H_2O (1.3196) to an accuracy of 1×10^{-4} RIU (refractive index unit), which is the absolute accuracy on all solutions. A more accurate value for the index step is determined by fitting theory to the measurements.

D. Cleaning Protocol

A cleaning protocol was followed when new devices were selected from a wafer in order to protect the bare Au surface in the channel section from contamination. The device was first placed in heptane and cleaned in an ultrasonic bath (37 kHz, 50% power) for 5 min to remove particles from the facets. Next, the dicing resist was removed from the top surface by placing the device in acetone for 5 min, then flushing with clean acetone, and placing in clean acetone for an additional 30 min, then flushing with isopropyl alcohol (IPA), and drying with N_2 gas. Next, in order to remove residual organics, the device was placed in a UV/ozone chamber for 15 min with the ultraviolet lamp on and another 15 min with the ozone only. Finally, the device was incubated in 1% 16-mercaptohexadecanoic acid (16-MHA) in IPA overnight to stabilize and make the Au surface hydrophilic. It is important to flush the device with plenty of distilled/deionized (DDI) H_2O before experiments, for the residual IPA in the channel may react with glycerol in the sample solutions forming a residual adlayer on the Au surface.

After the experiments, surface cleaning was conducted to remove any possible residue on the sensing arm. Prior to removal of the device from the setup, a 5% (weight-to-weight) solution of sodium dodecyl sulfate in H_2O was flowed at a 20 μl/min flow rate for 15 min and then DDI H_2O at 20 μl/min for 20 min to clean the microfluidic system and to remove any possible (loosely bound) contaminants. After dismounting the device, it was flushed with DDI H_2O and IPA in succession, dried with N_2, and placed in the UV/ozone chamber in the same way as in the cleaning protocol.

3. EXPERIMENTS AND ANALYSIS

A. Wavelength Sweeps

Due to fabrication imperfections, the operating wavelength of the coupler portion shifted from the originally designed wavelength of 1310 nm. To find a good operating wavelength, sweeping experiments from 1310 to 1378 nm were conducted for each solution with the input optical power kept constant and the initial alignment unchanged. The optical powers of the three outputs were measured and are shown in Fig. 3(a) as a waterfall plot of transfer characteristics at each wavelength and in Visualization 1 as a movie. It is observed that all three outputs have very small dynamic ranges around 1310 nm and that the dynamic ranges increase at longer wavelengths, which is reasonable because the LRSPP mode has lower attenuation at longer wavelength. Figures 3(b) and 3(c) show two typical transfer characteristics selected at 1346 and 1360 nm, illustrating the basic criteria for judging whether a transfer characteristic is considered "good" or "bad." At 1346 nm, the dynamic ranges of the output powers are relatively smaller, especially for P_1 and P_2, showing that the coupling at this wavelength is weak. The small dynamic ranges also make it difficult to appreciate the phase separation among the three transfer characteristics. In the ideal case, we expect that the three sinusoidal output curves should have similar dynamic ranges and should be separated by $2\pi/3$ rad [25]. Therefore, transfer characteristics like this one are considered "bad." At 1360 nm, the three

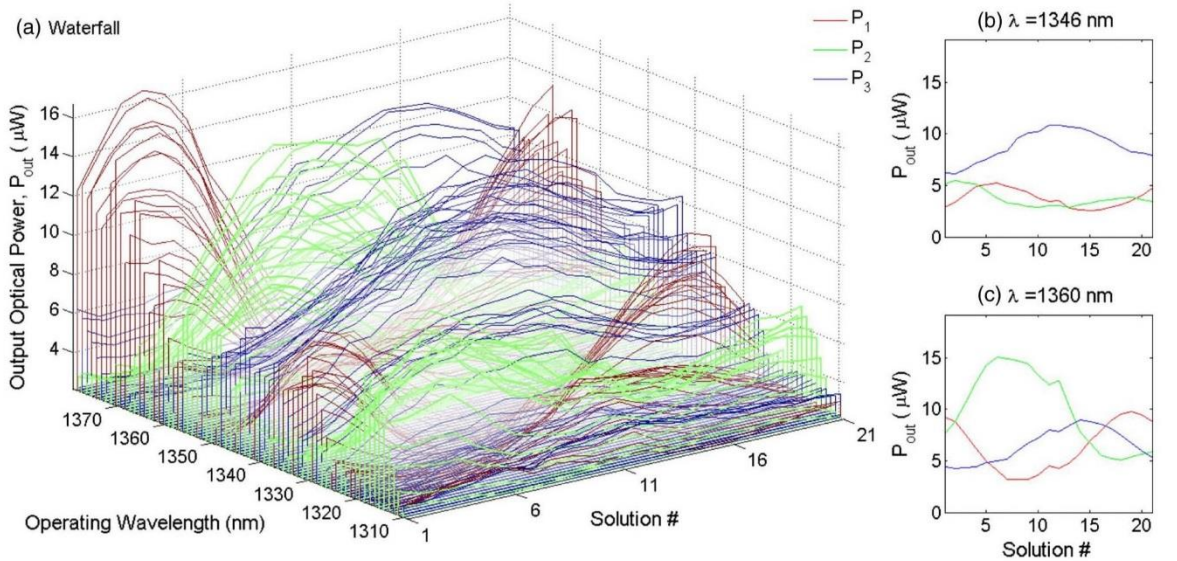

Fig. 3. (a) Waterfall plot of transfer characteristics from 1310 to 1378 nm, and typical transfer characteristics selected at (b) 1346 nm and (c) 1360 nm (Visualization 1).

outputs have a good dynamic range and their power levels are generally comparable. Also, it is observed that the three curves are separated by $\sim 2\pi/3$ rad. Therefore, transfer characteristics such as these are closer to ideal and the corresponding wavelength can be used to carry out sensing experiments.

B. Time Traces

Once the optimized wavelength is determined, a time-dependent transfer characteristic is obtained by recording the three output powers over ~60 s for each of the 21 solutions injected in sequence, while keeping the input power, wavelength, and initial alignment unchanged. For each solution, the output powers were averaged over 60 s and used to produce the transfer characteristic. Thus, each data point in the transfer characteristic is associated with a time trace from which noise statistics can be extracted.

Figure 4 represents a time trace obtained as Solution 21 replaces DDI H_2O in the fluidic fixture. The output powers fluctuate due to mixing of the fluids as they exchange. Visualization 2 shows a movie of the changes in the three output mode spots recorded during this process. It took ~30 s to complete the exchange of fluid at a flow rate of 20 μl/min. Normally, we wait for ~3 min after injecting a new solution into the system before recording the output powers in order to allow for replacement of the solution and for the output powers to stabilize.

Figure 5(a) shows the transfer characteristics measured on another triple-output MZI at 1318 nm (this operating wavelength deviates slightly from the design wavelength of 1310 nm). As expected, the three outputs are sinusoidal and separated by $\sim 2\pi/3$ rad. However, it is observed that P_3 has a lower dynamic range compared to the other two outputs. Therefore, the performance deviates from ideal and rather resembles a case where P_1 and P_2 form complimentary output pairs (as in a dual-output MZI). Nevertheless, the total power (sum of P_1, P_2, and P_3) is generally constant over all solutions. Following Ref. [25], the power differences $P_{di} = 2P_i - P_j - P_k$ ($i, j, k = 1, 2, 3$) are also plotted, and they show ~3× larger dynamic ranges relative to the individual outputs, which is one of the advantages of using a triple-output MZI. A mode mosaic identifying power switching between the three outputs is given as the inset.

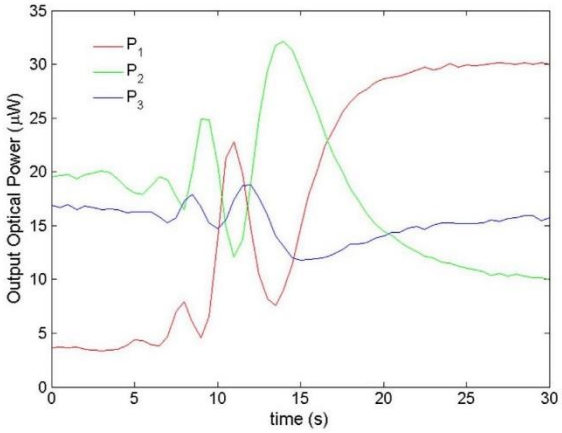

Fig. 4. Time tracing experiment showing one solution replacing another in the flow cell (Visualization 2).

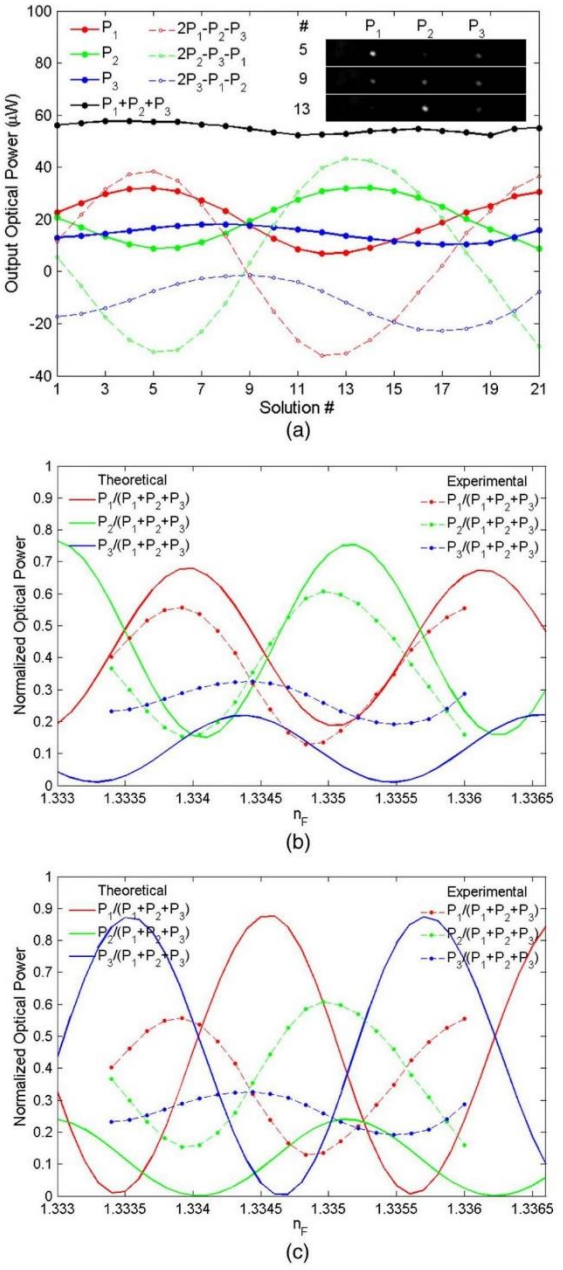

Fig. 5. (a) Transfer characteristics measured at 1375 nm. (b) Normalized measured transfer characteristics compared with theoretical curves obtained when $s = 2.1$ μm and the offset of the central waveguide is 1.0 μm and (c) when $s = 3.5$ μm without offset.

The normalized measurements were compared to theory, as shown in Fig. 5(b). We applied the theoretical model described extensively in [25]. The only change made was to adjust the

field's input into the triple-coupler section to take into account the unbalanced nature of the MZI by introducing the loss term $T_F \exp[-(\alpha_F - \alpha)L_F]$ to the field emanating from the sensing channel [see Fig. 1(a)]. The same fitting of RIs for the sample solutions as given in Ref. [16] was used because the two sets of experiments were conducted over the same timeframe. These RIs are plotted as the abscissa in Fig. 5(b), and the step between neighboring solutions in the series is 1.3×10^{-4} RIU. Comparing measurements and theory, it is observed that the fitting of power levels is good for P_1 and P_2 and fair for P_3, while the locations of peaks, valleys, and crossing points are generally aligned. The theoretical curves were obtained by increasing the coupling separation s from 2 to 2.1 μm and offsetting the central waveguide of the coupler portion to one side by 1.0 μm. The increase in coupling separation could be caused by the pressure that the O-ring exerts on the coupler portion when assembling the device in the fluidic fixture. The offset of the central waveguide is not supported by microscope observations of the device but effectively models the measured performance. Another set of theoretical curves obtained when $s = 3.5$ μm without offset is given in Fig. 5(c), showing an example that if the central waveguide is not offset, it is not the dynamic range of the side output (blue) but that of the middle one (green) that changes, and the abscissa of the theoretical peaks and valleys do not match the measurements either.

One problem noted during the experiments is that the measured performance depends on the input alignment conditions even though the waveguides support a single mode. It has been observed that even if the microfluidic fixture is untouched, a different initial misalignment at the input causes the transfer characteristics to change. It is thought that background light originating from imperfect input coupling and fabrication defects in the structure may be responsible for this behavior, which could in part explain the deviation between theory and experiment in Fig. 5(b). A possible method to solve the problem is to use gratings for input coupling [28], where the input light is incident perpendicularly instead of on a facet and along the device. Thus, the uncoupled light at the input does not interfere with the triple-coupler portion and will not affect the output powers.

C. Noise Analysis

Following Ref. [25], there are three independent detection schemes in a triple-output MZI: measuring an individual power P_i, a power difference $P_{di} = 2P_i - P_j - P_k$, and a normalized individual power $P_{ni} = P_i/(P_i + P_j + P_k)$, where $i, j, k = 1, 2, 3$. A normalized power difference [i.e., $(2P_i - P_j - P_k)/(P_i + P_j + P_k)$] has been shown to produce mathematically the same detection limit as the corresponding normalized individual power, so the former is not discussed in this paper. We also know that in the ideal case, the three outputs are separated by $\sim 2\pi/3$ rad, so there is always one output available that operates in the linear-response region which has sensitivity close to maximum. However, in Fig. 5, the device has one output of lower dynamic range compared to the others; the performance of the device is thus between that of a dual- and triple-output MZI. We therefore choose Solution 9 to carry out noise analysis because the two outputs of larger dynamic range (P_1 and P_2) operate in a linear region.

Figure 6(a)–6(i) show time traces associated with Solution 9, revealing the baseline noise in the system. A second experiment was carried out where the illumination on the alignment microscope above the setup was turned on and off a few times. In this way, a perturbation (artificial noise) was added manually in a controllable manner to demonstrate the ability of the structure

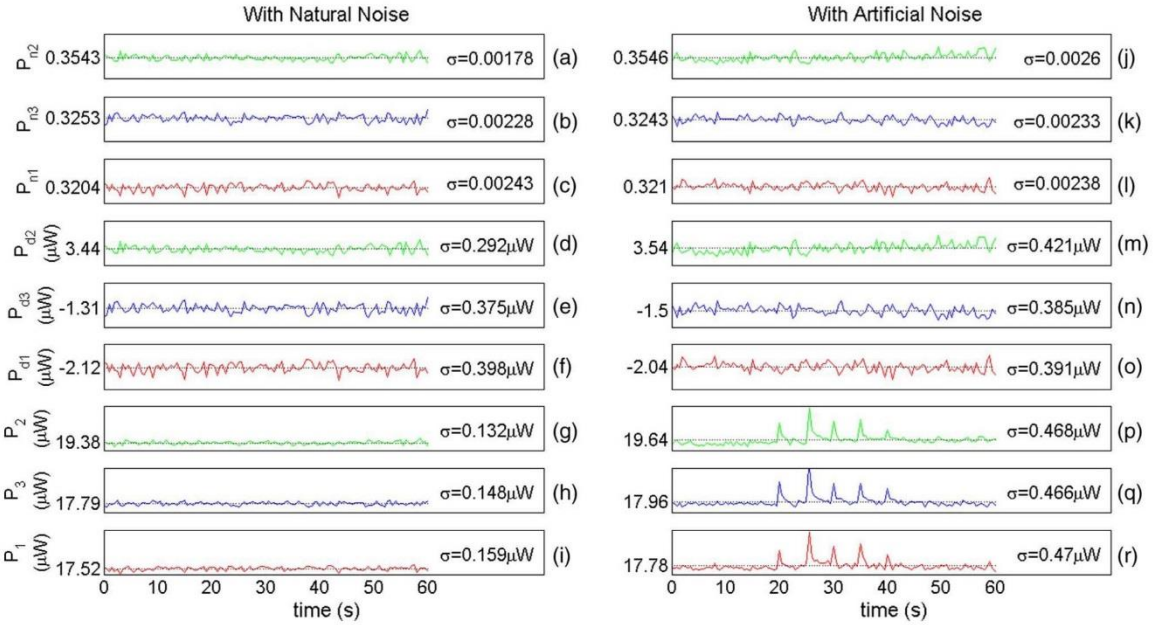

Fig. 6. Time traces associated with Solution 9 at 1318 nm with (a)–(i) natural noise and (j)–(r) artificial noise.

Table 1. Standard Deviations (σ), Sensitivities ($\partial P/\partial nF$), and Detection Limits (LOD) of All Detection Schemes

					Natural Noise		Artificial Noise	
	P at Sol. 8	P at Sol.10	ΔP Sol. 8–10	$\partial P/\partial n_F$ at Sol. 9	σ	LOD	σ	LOD
P_1	23.21319 μW	12.69963 μW	10.51356 μW	4.04×10^4 μW/RIU	0.1585 μW	7.84×10^{-6} RIU	0.4696 μW	2.32×10^{-5} RIU
P_2	14.56966 μW	23.71858 μW	9.148922 μW	3.52×10^4 μW/RIU	0.1323 μW	7.52×10^{-6} RIU	0.4676 μW	2.66×10^{-5} RIU
P_3	18.04506 μW	17.08658 μW	0.958477 μW	3.69×10^3 μW/RIU	0.1476 μW	8.01×10^{-5} RIU	0.4664 μW	2.53×10^{-4} RIU
P_{d1}	13.81166 μW	−15.4059 μW	29.21757 μW	1.12×10^5 μW/RIU	0.398 μW	7.08×10^{-6} RIU	0.3913 μW	6.96×10^{-6} RIU
P_{d2}	−12.1189 μW	17.65096 μW	29.76988 μW	1.14×10^5 μW/RIU	0.2921 μW	5.10×10^{-6} RIU	0.4213 μW	7.36×10^{-6} RIU
P_{d3}	−1.69274 μW	−2.24505 μW	0.552314 μW	2.12×10^3 μW/RIU	0.3751 μW	3.53×10^{-4} RIU	0.3849 μW	3.62×10^{-4} RIU
P_{n1}	0.415799	0.237355	0.178444	6.86×10^2 RIU^{-1}	0.0024	6.99×10^{-6} RIU	0.0024	6.99×10^{-6} RIU
P_{n2}	0.260975	0.443298	0.182324	7.01×10^2 RIU^{-1}	0.0018	5.13×10^{-6} RIU	0.0026	7.42×10^{-6} RIU
P_{n3}	0.323226	0.319347	0.00388	1.49×10^1 RIU^{-1}	0.0023	3.08×10^{-4} RIU	0.0023	3.08×10^{-4} RIU

to suppress common perturbations. Time traces with such artificial noise are shown in Figs. 6(j)–6(r). The noise level of the time traces is characterized by the standard deviation (σ) of each signal over the timeframe considered and is given in the inset to each plot. The average signal is also given, as labeled on each y axis. Figures 6(a)–6(c) and 6(j)–6(l) are time traces of normalized individual powers P_{ni}. These six curves are all plotted over a 0.03 vertical scale (dimensionless) and thus can be compared directly to each other. Figures 6(d)–6(f) and 6(m)–6(o) are time traces of power differences P_{di}, whereas Figs. 6(g)–6(i) and 6(p)–6(r) are those of the individual powers P_i. These 12 curves are all plotted over a 4 μW vertical power scale and thus can be compared directly to each other. By comparing Figs. 6(g)–6(i) with 6(p)–6(r), we clearly observe five spike-shaped pulses imposed similarly on all three outputs in the case of artificial noise (due to the manual perturbations). By comparing Figs. 6(g)–6(i) with 6(d)–6(f), we note that the noise levels increase in the power-difference scheme. However, by comparing Figs. 6(p)–6(r) with 6(m)–6(o), we note that the spike-shaped artificial noise is effectively suppressed by the power-difference scheme and that the noise levels decrease slightly. By inspecting Figs. 6(j)–6(l), we likewise observe that the spike-shaped artificial noise is effectively suppressed.

To compare the three detection schemes, it is necessary to determine their bulk sensitivity and noise level quantitatively, then to compute the limit of detection (LOD) as $\mathrm{LOD}(P) = \sigma(P) \cdot \mathrm{SNR}/(\partial P/\partial n_F)$, where σ is the standard deviation over time of the measurand P, SNR is the minimum signal-to-noise ratio required for reliable detection assumed to be $\mathrm{SNR} = 2$ (following [14] and [16]), and $\partial P/\partial n_F$ is the bulk sensitivity of the measurand estimated as $\partial P/\partial n_F \cong \Delta P/\Delta n_F$, where ΔP is determined from the average time traces for two solutions, and Δn_F is the difference in the RI of the solutions. The measurand P can be taken as P_i, P_{ni}, or P_{di}. The noises, sensitivities, and detection limits for all schemes are listed in Table 1.

In Table 1, it is observed in the case of natural noise that although the σ values of the power differences are larger than those of the individual powers, the LOD of P_{d2} is smaller than that of P_2 (from $\sim 7 \times 10^{-6}$ to $\sim 5 \times 10^{-6}$ RIU, comparable to the results in Ref. [16]), and the LOD of P_{d1} is also slightly improved relative to P_1, due to the 3× larger dynamic range of the difference schemes P_{di}. The normalized individual powers P_{ni} improve the LODs to generally the same levels as the power difference schemes. The LOD of P_3 is not improved by P_{d3} or P_{n3} since its sensitivity at Solution 9 is almost 0, far away from the linear-response region.

In the case of artificial noise, the σ values of the power differences are smaller than those of the individual powers, showing the removal of the artificial common perturbations. The LODs show that both the power differences P_{d1} and P_{d2} and the normalized individual powers P_{n1} and P_{n2} produce significant improvements compared to the individual powers P_1 and P_2 (from $\sim 25 \times 10^{-6}$ to $\sim 7 \times 10^{-6}$ RIU). This demonstrates the ability of the device to remove common perturbations from the signals.

4. CONCLUSIONS

In summary, optical bulk sensing using LRSPP triple-output MZIs was demonstrated. The device was composed of a MZI followed by a triple coupler in cascade, with a microfluidic channel etched through the top cladding of the sensing arm. Wavelength sweeps were conducted to determine the optimized operating wavelength of the device by choosing wavelengths that produce transfer characteristics closest to ideal. Time traces were conducted to analyze the natural and artificial noise present during a sensing experiment. A minimum detection limit of $\sim 5 \times 10^{-6}$ RIU was achieved by applying normalized or differential detection schemes. The device shows the ability of common perturbation suppression and benefits from a 3× larger dynamic range compared to a single-output MZI. The detection limit can be further improved by optimizing the design of the sensor and the interrogation setup.

Acknowledgment. We acknowledge Wei Ru Wong and Oleksiy Krupin for help on the construction of the setup and Charles Chiu and Hamoudi Asiri for fabricating the devices.

REFERENCES

1. M. A. Cooper, "Optical biosensors in drug discovery," Nat. Rev. Drug Discovery **1**, 515–528 (2002).
2. S. Löfås, "Optimizing the hit-to-lead process using SPR analysis," Assay Drug Dev. Technol. **2**, 407–416 (2004).
3. J. Homola, "Surface plasmon resonance sensors for detection of chemical and biological species," Chem. Rev. **108**, 462–493 (2008).
4. A. Sinibaldi, A. Fieramosca, R. Rizzo, A. Anopchenko, N. Danz, P. Munzert, C. Magistris, C. Barolo, and F. Michelotti, "Combining label-free and fluorescence operation of Bloch surface wave optical sensors," Opt. Lett. **39**, 2947–2950 (2014).

5. P. Berini, "Long-range surface plasmon polaritons," Adv. Opt. Photon. **1**, 484–588 (2009).
6. J. Dostálek, A. Kasry, and W. Knoll, "Long range surface plasmons for observation of biomolecular binding events at metallic surfaces," Plasmonics **2**, 97–106 (2007).
7. R. Slavík and J. Homola, "Ultrahigh resolution long range surface plasmon-based sensor," Sens. Actuators B **123**, 10–12 (2007).
8. M. Vala, S. Etheridge, J. A. Roach, and J. Homola, "Long-range surface plasmons for sensitive detection of bacterial analytes," Sens. Actuators B Chem. **139**, 59–63 (2009).
9. V. Chabot, Y. Miron, M. Grandbois, and P. G. Charette, "Long range surface plasmon resonance for increased sensitivity in living cell biosensing through greater probing depth," Sens. Actuators B **174**, 94–101 (2012).
10. O. Krupin, H. Asiri, C. Wang, R. N. Tait, and P. Berini, "Biosensing using straight long-range surface plasmon waveguides," Opt. Express **21**, 698–709 (2013).
11. O. Krupin, C. Wang, and P. Berini, "Selective capture of human red blood cells based on blood group using long-range surface plasmon waveguides," Biosens. Bioelectron. **53**, 117–122 (2014).
12. O. Krupin, C. Wang, and P. Berini, "Detection of leukemia markers using long-range surface plasmon waveguides functionalized with protein G," Lab on a Chip **15**, 4156–4165 (2015).
13. W. R. Wong, O. Krupin, S. D. Sekaran, F. R. M. Adikan, and P. Berini, "Serological diagnosis of dengue infection in blood plasma using long-range surface plasmon waveguides," Anal. Chem. **86**, 1735–1743 (2014).
14. A. Khan, O. Krupin, E. Lisicka-Skrzek, and P. Berini, "Mach–Zehnder refractometric sensor using long-range surface plasmon waveguides," Appl. Phys. Lett. **103**, 111108 (2013).
15. K. C. Vernon, D. E. Gómez, and T. J. Davis, "A compact interferometric sensor design using three waveguide coupling," J. Appl. Phys. **106**, 104306 (2009).
16. H. Fan and P. Berini, "Bulk sensing using a long-range surface plasmon dual-output Mach–Zehnder interferometer," J. Lightwave Technol. **34**, 2631–2638 (2016).
17. R. G. Heideman and P. V. Lambeck, "Remote opto-chemical sensing with extreme sensitivity: design, fabrication and performance of a pigtailed integrated optical phase-modulated Mach–Zehnder interferometer system," Sens. Actuators B **61**, 100–127 (1999).
18. B. J. Luff, J. S. Wilkinson, J. Piehler, U. Hollenbach, J. Ingenhoff, and N. Fabricius, "Integrated optical Mach–Zehnder biosensor," J. Lightw. Technol. **16**, 583–592 (1998).
19. H. Nguyen, F. Sidiroglou, S. F. Collins, T. J. Davis, A. Roberts, and G. W. Baxter, "A localized surface plasmon resonance-based optical fiber sensor with sub-wavelength apertures," Appl. Phys. Lett. **103**, 193116 (2013).
20. P. Hua, B. Jonathan Luff, G. R. Quigley, J. S. Wilkinson, and K. Kawaguchi, "Integrated optical dual Mach–Zehnder interferometer sensor," Sens. Actuators B **87**, 250–257 (2002).
21. M. Kitsara, K. Misiakos, I. Raptis, and E. Makarona, "Integrated optical frequency-resolved Mach–Zehnder interferometers for label-free affinity sensing," Opt. Express **18**, 8193–8206 (2010).
22. Y. Gao, Q. Gan, Z. Xin, X. Cheng, and F. J. Bartoli, "Plasmonic Mach–Zehnder interferometer for ultrasensitive on-chip biosensing," ACS Nano **5**, 9836–9844 (2011).
23. X. Zeng, Y. Gao, H. Hu, D. Ji, Q. Gan, and F. J. Bartoli, "A metal-insulator-metal plasmonic Mach–Zehnder interferometer array for multiplexed sensing," J. Appl. Phys. **113**, 133102 (2013).
24. H. Fan and P. Berini, "Noise cancellation in long-range surface plasmon dual-output Mach–Zehnder interferometers," J. Lightwave Technol. **31**, 2606–2612 (2013).
25. H. Fan, R. Charbonneau, and P. Berini, "Long-range surface plasmon triple-output Mach–Zehnder interferometers," Opt. Express **22**, 4006–4020 (2014).
26. C. Chiu, E. Lisicka-Skrzek, R. N. Tait, and P. Berini, "Fabrication of surface plasmon waveguides and devices in Cytop with integrated microfluidic channels," J. Vac. Sci. Technol. B **28**, 729–735 (2010).
27. H. Asiri, "Fabrication of surface plasmon biosensors in Cytop," Master's thesis (University of Ottawa, 2012).
28. N. Fong, P. Berini, and R. Niall Tait, "Characterization of grating-coupled long range surface plasmon polariton membrane waveguides," Opt. Express **23**, 17421–17430 (2015).

Chapter 7

Conclusions

7.1 Summary and contributions

In recent years, researchers have studied LRSPPs for various applications such as thermo-optic, optical bulk and biochemical sensing, using straight waveguide and single-output MZI. In sensing applications, it is necessary to reduce the noise level in order to obtain better detection limits. An important method to realize this is to use multiple-output MZIs so that the common portion of the perturbations among the outputs can be canceled. Despite some theoretical analysis on the performances of 2×2 and 3×3 couplers, little investigation on the transfer characteristics of dual- and triple-output MZIs had been reported. Chapter 2 presented the experimental results of the transfer characteristics of single-output MZIs compared to theoretical expectation based on the plane-wave model, serving as a basis to analyze the performance of multiple-output MZIs theoretically and experimentally, as multiple-output MZIs are constituted of a single-output MZI in cascade with a multiple-output directional coupler. It also provides a safe current density 70 GA/m^2 for thermo-optic modulation, in order to prevent the waveguide from temporary interruptions such as antiguide effect and permanent damage such as electromigration in the Au stripe and glass transition in the Cytop claddings.

The theory applied and examined in Chapter 2 was combined with the analysis of a 3-dB (50:50) coupler also based on the plane-wave model to obtain a theoretical model for dual-

output MZIs in Chapter 3. Thermo-optic experiments were conducted and compared to theory. The results verify the sinusoidal response of an individual output and the complementary relation between the two outputs. The experiments also show that the operating wavelength of the coupler has been shifted from the designed wavelength 1310 nm to ~1370 nm due to fabrication imperfections, and the exact new operating wavelength is waveguide dependent. In order to realize the suppression of common perturbation, 4 detection schemes - an individual power scheme, a power difference scheme, a normalized individual power scheme, and a normalized power difference scheme were analyzed and compared. It was demonstrated mathematically that the latter two schemes produce identical performance. It is found that subtracting the two output powers and normalizing them provides generally the same level of minimum detectable phase shift of ~ 3 mrad, 4 × lower than obtained from the individual power scheme.

As for a triple-output MZI, the plane-wave model is no longer applicable. Instead, local normal mode theory is used in which modal analysis of the 3×3 coupler is conducted and overlap integrals on the input and output of the coupler are calculated to determine the theoretical output powers of the whole device, as presented in Chapter 4. Thermo-optic experimental results obtained at an operating wavelength of ~1370 nm verify the ~2π/3 rad phase separation between the outputs. Similar noise analyses are applied as in Chapter 3, except that the power difference scheme is redefined so as to have a 3× larger dynamic range, and it is shown specifically that the power difference scheme is better at dealing with perturbations on the output side such as the background light, while the normalization scheme is better at dealing with perturbations on the input side such as drifting and end-fire coupling misalignment. A minimum detectable phase shift ~2/3 that of an individual output

is obtained. The smallest minimum detectable phase shift obtained is 7.3 mrad. The advantage of a triple-output MZI over a dual-output one is that an output operating in the linear region of the corresponding curve is always available; therefore there is no restriction that a data point with the maximum sensitivity in the curves must be selected.

By etching the top cladding to produce a fluidic channel, the dual- and triple- output MZIs can be applied to optical bulk sensing. Chapter 5 uses a dual-output MZI in bulk (refractometric) sensing experiments in a similar way as in Chapter 3. However, the change in effective index of the LRSPP mode due to the injection of a sample solution may unbalance the two arms of the MZI, and therefore a plane-wave model for unbalanced dual-output MZIs was constructed in the theoretical part. In the experimental part, a wavelength sweep experiment was designed and carried out, enabling the determination of the shifted operating wavelength due to fabrication imperfections. The accurate refractive indices of the sample solutions used in the experiments were determined by fitting theoretical transfer characteristics to the measurements. A detection limit of $\sim 4\times10^{-6}$ RIU was achieved by applying three detection schemes to the time traces in a similar way as in Chapter 3. Time traces with artificial noise were obtained to show the effectiveness of the device to suppress common perturbations.

Chapter 6 applies the bulk sensing experimental technique developed in Chapter 5 to triple-output MZIs, producing a comparable detection limit of $\sim 5\times10^{-6}$ RIU, not as good as that of the dual-output MZIs but this does not necessarily mean that the triple-output MZIs are less competitive. They are more susceptible to imperfections in input alignment, setup, and fabrication, which lead to deviations from the ideal performance of a triple-output MZI, but all can be improved. There can be a few improvements on the design of the waveguides, the

details of the structures, and the device layout. With enough potential improvements, it is possible to obtain the ideal performances of a triple-output MZI, in which the detection ability is expected to be even better than that of a dual-output MZI. Besides, the triple-output MZIs show the same advantages compared to their single- and dual-output counterparts, in a similar way as demonstrated in Chapter 4. Therefore, the triple-output MZIs could be more promising than the dual-output ones. Key points summarizing the performance of the MZIs are listed in Table 7.1, where L_F is the length of the microfluidic channel for bulk sensing experiments. The multiple-output MZIs show their superiority in detection limit even with shorter microfluidic channels (sensing surfaces). The improvement would be more significant if they had the same channel length.

	Single-output MZI	Dual-output MZI	Triple-output MZI
Dynamic Range	1×	2×	3×
Ability of Common Perturbation Suppression	No	Yes	Yes
Availability of Maximum Sensitivity	Tunable	Tunable	Always
Detection Limit in Bulk Sensing (RIU)	6×10^{-6} (L_F = 1.6 mm)	4×10^{-6} (L_F = 1.2 mm)	5×10^{-6} (L_F = 1.2 mm)
Potential for Improvements	Limited	Fair	High

Table 7.1 Summary of the performance of the single-, dual-, and triple-output MZIs.

7.2 Future Work

One suggestion for future work is to redesign the layout of the devices. As reported in Supplementary in Chapter 5, the pressure the O-ring of the microfluidic fixture exerts on the top cladding of the coupler portion may affect its performance. As the pressure changes

every time we assemble the microfluidic fixture, so does the coupler performance change depending on the tightness the cover was fixed on the device holder. This problem can be resolved by changing the layout so that the O-ring is removed from the top of the coupler portion. There can be other improvements on the device layout; for instance, the Y-junction at the input side of the MZIs can be improved by accessing better resolution lithography, or by replacing with a coupler or a multi-mode interferometer, which could possibly decrease the transition loss at the Y-junction.

Another suggestion is to further investigate the dependence of the measured performance of the multiple-output MZIs on the input alignment conditions, as noted in the Supplementary section of Chapter 5 as well as in Chapter 6, where a different initial misalignment at the input changes the transfer characteristics. A possible cause is the background light originating from imperfect input coupling and fabrication defects in the structure, which can be excluded by changing the input coupling from end-fire excitation to grating excitation in a perpendicular direction.

A third suggestion is to change the measurement method of the output optical power. As discussed in the Supplementary section of Chapter 5, despite the ability to suppress common perturbations and the larger dynamic range, the LODs reported in this thesis is significantly larger than that in Ref. [46] (~4×10^{-6} RIU compared to ~1×10^{-6} RIU), which cannot be fully attributed to the difference in the sensing length on the MZIs (~1.2 mm compared to ~1.6 mm). Changing to a better camera or replacing it with a fiber array and a power meter may be worth trying, but as for the latter option, an efficient alignment method must be developed.

Besides, the waveguide itself can be further improved with new fabrication processes that are potentially applicable. In the past, researchers have demonstrated the reverse-symmetry waveguide technique to enhance the surface sensitivity of dielectric waveguides [53]. It may be possible to develop a similar method for the fabrication of LRSPP waveguides.

Finally, the devices of interest and the whole experimental technique developed in optical bulk sensing can be applied to biosensing and to the detection of diseases in complex fluids in a similar way as in Ref. [43-45]. The advantages of the multiple-output MZIs, especially the triple-output MZIs, render the devices promising for biosensing applications.

Bibliography

[1] H. Raether, Surface Plasmons on Smooth and Rough Surfaces and on Gratings, Springer, 1988.

[2] V. M. Agranovich and D. L. Miles, Surface Polaritons: Electromagnetic Waves at Surfaces and Interfaces, Eds., North Holland, 1982.

[3] A. D. Boardman, Ed., Electromagnetic Surface Modes, Wiley, 1982.

[4] P. Berini, "Long-range surface plasmon polaritons," Advances in Optics and Photonics 1, 484-588 (2009).

[5] G. Gagnon, N. Lahoud, G. A. Mattiussi, and P. Berini, "Thermally activated variable attenuation of long-range surface plasmon-polariton waves," Journal of Lightwave Technology 24 (11), 4391-4402 (2006).

[6] E. D. Palik and G. Ghosh, Electronic Handbook of Optical Constants of Solids. New York: Academic, 1999.

[7] Asahi Glass Co., Ltd., Japan, "Amorphous fluoropolymer CYTOP," Jan. 2009 [Online]. Available: www.agc-cytop.com

[8] P. N. Prasad, Introduction to Biophotonics, Wiley, Toronto, 2003.

[9] S. G. Ignatov, J. A. Ferguson, and D. R. Walt, "A fiber-optic lactate sensor based on bacterial cytoplasmic membranes", Biosensors and Bioelectronics 16 (1), 109-113 (2001).

[10] M. A. Cooper, "Optical biosensors in drug discovery," Nature Rev. Drug Discov. 1 (7), 515-528 (2002).

[11] P. Berini, "Bulk and surface sensitivities of surface plasmon waveguides," New J. Phys. 10 (10), 105010 (2008).

[12] T. Nikolajsen, K. Leosson, and S. I. Bozhevolnyi, "In-line Extinction modulator based on long-range surface plasmon-polaritons," Optical Communication 244 (1), 455-459 (2005).

[13] H. Fan and P. Berini, "Thermo-optic characterisation of long-range surface plasmon devices in Cytop," Applied Optics 52 (2), 162-170 (2013).

[14] S. Park and S. H. Song, "Polymeric variable optical attenuator based on long range surface plasmon polaritons," Electronics Letters 42 (7), 402-404 (2006).

[15] K. Leosson, T. Nikolajsen, A. Boltasseva, and S. I. Bozhevolnyi, "Long-range surface plasmon polariton nanowire waveguides for device applications," Optical Express 14 (1), 314-319 (2006).

[16] K. Leosson, T. Rosenzveig, P. G. Hermannsson, and A. Boltasseva, "Compact plasmonic variable optical attenuator," Optics Express 16 (20), 15546-15552 (2008).

[17] T. Rosenzveig, P. G. Hermannsson, A. Boltasseva, and K. Leosson, "Optimizing performance of plasmonic devices for photonic circuits," Applied Physics A, 100 (2), 341-346 (2010).

[18] I. Breukelaar, R. Charbonneau, and P. Berini, "Long-range surface plasmon-polariton mode cutoff and radiation in embedded strip waveguides," Journal of Applied Physics 100 (4), 043104 (2006).

[19] I. Breukelaar and P. Berini, "Long-range surface plasmon polariton mode cutoff and radiation in slab waveguides," Journal of Optical Society of America A 23 (8), 1971-1977 (2006).

[20] T. Nikolajsen, K. Leosson, and S. I. Bozhevolnyi, "Surface plasmon polariton based modulators and switches operating at telecom wavelengths," Applied Physics Letters 85 (24), 5833-5835 (2004).

[21] J. Gosciniak, S. I. Bozhevolnyi, T. B. Andersen, V. S. Volkov, J. Kjelstrup-Hansen, L. Markey, and A. Dereux, "Thermo-optic control of dielectric-loaded plasmonic waveguide components," Optics Express 18 (2), 1207-1216 (2010).

[22] J. Gosciniak, L. Markey, A. Dereux, and S. I. Bozhevolnyi, "Efficient thermo-optically controlled Mach-Zehnder interferometers using dielectric-loaded plasmonic waveguides," Optics Express 20 (15), 16300-16309 (2012).

[23] J. C. Weeber, T. Bernardin, M. G. Nielsen, K. Hassan, S. Kaya, J. Fatome, C. Finot, A. Dereux, and N. Pleros, "Nanosecond thermo-optical dynamics of polymer loaded plasmonic waveguides," Optics express 21 (22), 27291-27305 (2013).

[24] S. Kaya, J. C. Weeber, F. Zacharatos, K. Hassan, T. Bernardin, B. Cluzel, J. Fatome, and C. Finot, "Photo-thermal modulation of surface plasmon-polariton propagation at telecommunication wavelengths," Optics Express 21 (19), 22269-22284 (2013).

[25] R. S. Marks, A. Novoa, D. Thomassey, and S. Cosnier, “An innovative strategy for immobilization of receptor proteins on to an optical fiber by use of poly (pyrrole-biotin)”, Analytical Bioanalytical Chemistry 374 (6), 1056-1063 (2002).

[26] L. Zhu, Y. Li, and G. Zhu “A novel flow through optical fiber biosensor for glucose based on luminol electrochemiluminescence”, Sensors and Actuators B 86 (2), 209-214 (2002).

[27] M. C. Ramos, M. C. Torrijas, and A. N. Diaz, “Enhanced chemiluminiscence biosensor for the determination of phenolic compounds and hydrogen peroxide”, Sensors and Actuators B Chem 73 (1), 71–75 (2001).

[28] R. Garg, S. M. Tripathi, K.Thyagarajan, and W. J. Bock, “Long period fiber grating based temperature-compensated high performance sensor for bio-chemical sensing applications,” Sensors and Actuators B Chemistry 176, 1121–1127 (2013).

[29] B. N. Feltis, B. A. Sexton, F. L. Glenn, M. J. Best, M. Wilkins, and T. J. Davis, “A hand-held surface plasmon resonance biosensor for the detection of ricin and other biological agents,” Biosensors and Bioelectronics 23 (7), 1131-1136 (2007).

[30] S. Y. Wu, H. P. Ho, W. C. Law, C. Lin, and S. K. Kong, “Highly sensitive differential phase-sensitive surface plasmon resonance biosensor based on the Mach-Zehnder configuration,” Optics Letters 29 (20), 2378-2380 (2004).

[31] Y. Hadjar, M. Renault, S. Blaize, A. Bruyant, R. Vincent, and A. Hmima, “Compact interferometer transducer based on surface plasmon phase resonance,” Journal of Optcial Society of Amercia A 32 (5), 771-777 (2015).

[32] H. Nguyen, F. Sidiroglou, S. F. Collins, T. J. Davis, A. Roberts, and G. W. Baxter, “A localized surface plasmon resonance-based optical fiber sensor with sub-wavelength apertures,” Applied Physics Letters 103 (19), 193116 (2013).

[33] T. Špringer, M. L. Ermini, B. Špačková, J. Jabloňků, and J. Homola, “Enhancing Sensitivity of Surface Plasmon Resonance Biosensors by Functionalized Gold Nanoparticles: Size Matters,” Analytical Chemistry 86 (20), 10350–10356 (2014).

[34] H. Vaisocherová, H. Šípová, I. Víšová, M. Bocková, T. Špringer, M. L. Ermini, X. Song, Z. Krejčík, L. Chrastinová, O. Pastva, K. Pimková, M. D. Merkerová, J. E. Dyr, J. Homola, “Rapid and sensitive detection of multiple microRNAs in cell lysate by low-

fouling surface plasmon resonance biosensor," Biosensors and Bioelectronics 70, 226–231 (2015).

[35] Y. Gao, Q. Gan, Z. Xin, X. Cheng, and F. J. Bartoli, "Plasmonic Mach-Zehnder interferometer for ultrasensitive on-chip biosensing," ACS Nano 5 (12), 9836-9844 (2011).

[36] X. Zeng, Y. Gao, H. Hu, D. Ji, Q. Gan, and F. J. Bartoli, "A metal-insulator-metal plasmonic Mach-Zehnder interferometer array for multiplexed sensing," Journal of Applied Physics 113 (13), 133102 (2013).

[37] J. Dostálek, A. Kasry, and W. Knoll, "Long range surface plasmons for observation of biomolecular binding events at metallic surfaces," Plasmonics 2 (3), 97-106 (2007).

[38] R. Slavík, and J. Homola, "Ultrahigh resolution long range surface plasmon-based sensor," Sensors and Actuators B Chemistry 123 (1), 10-12 (2007).

[39] M. Vala, S. Etheridge, J. A. Roach, and J. Homola, "Long-range surface plasmons for sensitive detection of bacterial analytes," Sensors and Actuators B Chemistry 139 (1), 59-63 (2009).

[40] V. Chabot, Y. Miron, M. Grandbois, and P. G. Charette, "Long range surface plasmon resonance for increased sensitivity in living cell biosensing through greater probing depth," Sensors and Actuators B Chemistry 174, 94-101 (2012).

[41] O. Krupin, H. Asiri, C. Wang, R. N. Tait, and P. Berini, "Biosensing using straight long-range surface plasmon waveguides," Optics Express 21 (1), 698-709 (2013).

[42] O. Krupin, C. Wang, and P. Berini, "Selective capture of human red blood cells based on blood group using long-range surface plasmon waveguides," Biosensors and Bioelectronics 53, 117-122 (2014).

[43] O. Krupin, C. Wang, and P. Berini, "Detection of leukemia markers using long-range surface plasmon waveguides functionalized with protein G," Lab on a Chip 15 (21), 4156-4165 (2015).

[44] W. R. Wong, O. Krupin, S. D. Sekaran, F. R. M. Adikan, and P. Berini, "Serological diagnosis of dengue infection in blood plasma using long-range surface plasmon waveguides," Analytical Chemistry 86 (3), 1735-1743 (2014).

[45] P. Béland, O. Krupin, and P. Berini, "Selective detection of bacteria in urine with a long-range surface plasmon waveguide biosensor," Biomedical Optics Express 6 (8), 2908-2922 (2015).

[46] A. Khan, O. Krupin, E. Lisicka-Skrzek, and P. Berini, "Mach-Zehnder refractometric sensor using long-range surface plasmon waveguides," Applied Physics Letters 103 (11), 111108 (2013).

[47] K. C. Vernon, D. E. Gómez, and T. J. Davis, "A compact interferometric sensor design using three waveguide coupling," Journal of Applied Physics 106 (10), 104306 (2009).

[48] M. Paniccia, P. Flynn, and R. Reifenberger, "Scanning probe microscopy studies of electromigration in electroplated Au wires," Journal of Applied Physics 73 (12), 8189–8197 (1993).

[49] A. S. Oates, "Electromigration transport mechanisms in Al thin-film conductors," Journal of Applied Physics 79 (1), 163-169 (1996).

[50] S. Takenobu, Y. Kuwana, K. Takayama, Y. Sakane, M. Ono, H. Sato, N. Keil, W. Brinker, H. Yao, C. Zawadzki, Y. Morizawa, and N. Grote, "All-polymer 8x8 AWG wavelength router using ultra low loss polymer optical waveguide material (CYTOP)," Proceedings of OFC/NFOEC, paper JWA 32, (2008).

[51] C. Chiu, E. Lisicka-Skrzek, R. N. Tait, and P. Berini, "Fabrication of surface plasmon waveguides and devices in Cytop with integrated microfluidic channels," Journal of Vacuum Science and Technology B 28 (4), 729–735 (2010).

[52] H. Fan, R. Buckley, and P. Berini, "Passive long-range surface plasmon-polariton devices in Cytop," Applied Optics 51 (10), 1459-1467 (2012).

[53] R. Horvath, L. R. Lindvold, and N. B. Larsen, "Reverse-symmetry waveguides: theory and fabrication," Applied Physics B 74 (4-5), 383–393 (2002).